Growth, Characterisation and Modelling of Novel Magnetic Thin Films for Engineering Applications

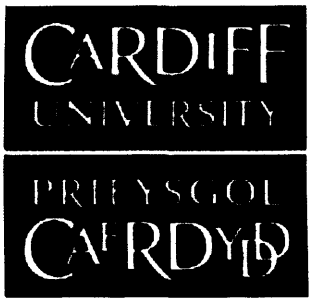

Arun Raghunathan

Wolfson Centre for Magnetics
School of Engineering

Cardiff University

A thesis submitted for the degree of

Doctor of Philosophy

October 2010

ProQuest LLC
789 East Eisenhower Parkway
P.O. Box 1346
Ann Arbor, MI 48106-1346

DECLARATION

This work has not previously been accepted in substance for any degree and is not concurrently submitted in candidature for any degree.

Signed: (candidate) Date: 11 October 2010

STATEMENT 1

This thesis is being submitted in partial fulfilment of the requirements for the degree of PhD.

Signed: (candidate) Date: 11 October 2010

STATEMENT 2

This thesis is the result of my own independent work/investigation, except where otherwise stated. Other sources are acknowledged by explicit references.

Signed: (candidate) Date: 11 October 2010

STATEMENT 3

I hereby give consent for my thesis, if accepted, to be available for photocopying and for inter-library loan, and for the title and summary to be made available to outside organisations.

Signed: (candidate) Date: 11 October 2010

Acknowledgements

I would like to thank Prof. David Jiles for providing me with an opportunity to pursue research at Cardiff University and for his continuous support at every stage of this research.

I am grateful to Dr John Snyder and Dr Yevgen Melikhov for their invaluable guidance throughout this study without which this research would not have been complete.

I would like to personally thank Prof. Anil Prabhakar of IIT Madras who always believed in my abilities and introduced me to Prof. Jiles.

My sincere gratitude to Mr Paul Farrugia and his technical team in the electrical workshop who always helped me with debugging and fixing the faulty equipments (usual routine!). I appreciate the efforts of Mr Steve Mead and his team in the mechanical workshop for helping me with the design and development of the bender in a very short time.

I am grateful to Mr Pete Fisher and Mr Tony Oldroyd of School of Earth Sciences for letting me use their SEM and XRD facilities, without which the analysis part of this research would have been difficult.

I am thankful to all Wolfson Centre (if I may say so!) colleagues for many insightful discussions and to all my friends who directly or indirectly played a role in the smooth completion of this research.

I also admire and appreciate the kindness and benevolence of engineering research office staff (Nicola, Chris, Julie, Rachel, Jeanette...).

I am deeply indebted to and greatly proud of my family who stood by me and encouraged me to pursue my dreams.

Abstract

Magnetic materials, especially thin films, are being exploited today in many engineering applications such as magnetic recording heads and media, magnetic sensors and actuators and even magnetic refrigeration due to their smaller form factor or to thin film effects that do not occur in bulk material. Hence there is a need for optimised growth of thin films to suit the requirements of applications. The aim of this research work is two-fold:

1. Growth and characterisation of optimised magnetic thin films using pulsed-laser deposition and
2. Extension of Jiles-Atherton (JA) theory of hysteresis.

A series of magnetoelastic thin films based on cobalt ferrite were deposited on SiO_2/Si(100) substrates using pulsed-laser deposition at different substrate temperatures and different reactive oxygen pressures. The crystal structure, composition, magnetic properties, microstructure and magnetic domains of cobalt ferrite thin films were investigated. The optimised growth conditions of polycrystalline spinel cobalt ferrite thin films were determined from characterisation results. The Curie point of the optimised cobalt ferrite thin film was determined from moment vs. temperature measurement. The optimised thin film was magnetically annealed in order

to induce an in-plane uniaxial anisotropy. The magnetostriction of the optimised sample was determined in the vibrating sample magnetometer using the inverse measurement technique. A special 3-point bender was designed and built for this purpose.

The first successful thin film of $Gd_5Si_2Ge_2$, a magnetocaloric rare earth intermetallic alloy, was deposited on a polycrystalline AlN substrate. The crystal structure, composition and magnetic phase transformation of $Gd_5Si_2Ge_2$ thin film were investigated. The preliminary results are furnished in this thesis.

The JA model of hysteresis was extended to incorporate thermal dependence of magnetic hysteresis. The extended model was validated against measurements made on substituted cobalt ferrite material. A functional form of anhysteretic magnetisation was derived. The JA theory was also extended to model magnetic two-phase materials. This proposed model was qualitatively compared with measured data published in the literature. The JA theory was applied to magnetoelastic thin films. The cobalt ferrite thin films deposited on SiO_2/Si(100) substrates at different substrate temperatures and oxygen pressures have been modelled based on JA theory and were validated against measurements. This model would help in understanding the influence of deposition parameters on properties of thin films. The calculated and measured data were in excellent agreement.

Contents

List of Figures

List of Tables

Nomenclature

Greek Symbols

α	Domain coupling
β	Critical exponent
χ_{an}	Anhysteretic susceptibility
χ_{in}	Initial susceptibility
ϵ	Mechanical strain
γ	Angle between magnetic field and unique axis
λ	Magnetostriction
Ω	Angle between magnetic moment and unique axis
θ	Angle between magnetic moment and applied field

Other Symbols

ΔT_{ad}	Adiabatic temperature change
a	Domain density

c	Reversibility parameter
H_e	Effective magnetic field
H_k	Anisotropy field
H_{ex}	Exchange field
k	Pinning parameter
k_B	Boltzmann's constant
K_u	Anisotropy constant
m	Magnetic moment
M_S	Spontaneous magnetisation
M_{an}	Anhysteretic magnetisation
M_{irr}	Irreversible magnetisation
M_{rev}	Reversible magnetisation
N	Number of independent magnetic moments
T	Temperature
T_C	Curie temperature
v	Poisson's ratio
Y	Young's modulus
Z	Total partition function

Acronyms

AF Antiferromagnetic

AFM Atomic force microscopy

APB Antiphase boundary

CVD Chemical vapour deposition

EDX Energy dispersive X-ray spectroscopy

FM Ferromagnetic

ICCD Intensified change-coupled device

JA Jiles-Atherton

MFM Magnetic force microscopy

PLD Pulsed-laser deposition

PM Paramagnetic

PVD Physical vapour deposition

RMSE Root mean square error

SEM Scanning electron microscopy

SQUID Superconducting Quantum Interference Device

VSM Vibrating sample magnetometer

XRD X-ray diffraction

Chapter 1

Introduction

1.1 Scope, motivation and contribution

Magnetic materials have been applied to solve many engineering challenges. The number of applications that exploit the properties of magnetic materials is constantly increasing. Magnetic materials in the form of bulk, thin films, nanowires, and ferrofluids have revolutionised the field of magnetism with important applications such as magnetic recording, data storage, sensors, actuators and magnetic authentication. Magnetoelastic and magnetocaloric materials among others are being thoroughly investigated as they are promising candidates for tackling today's sensing (magnetostriction) and energy (magnetic refrigeration) needs respectively.

Ferrites are a class of materials discovered in the early 1900s, that are applied in high frequency applications [Snoek, 1936]. Cobalt ferrite, a member of the ferrites family has been investigated in recent years due to its magnetoelasticity, a property that can be applied in sensors [Smit & Wijn, 1959]. Further-

more, cobalt ferrite was shown to be adaptable enough that its properties can be tailored to meet the requirements of different applications [Lo et al., 2005; Song, 2007].

$Gd_5Si_2Ge_2$, a rare earth intermetallic alloy which exhibits magnetocaloric effect can be a replacement for conventional refrigeration [Pecharsky & Gschneidner Jr., 1997a]. A magnetic refrigerator built using this material was found to be twice as efficient as conventional refrigerators. The Carnot efficiency was found to be ~60% in magnetic refrigerators, whereas it is only ~30% in conventional liquid-vapour refrigerators.

In order to build complete working models to demonstrate the capabilities of magnetoelastic and magnetocaloric materials, there is a need to produce them in thin film forms which are ideal for device applications. Hence this thesis aims at

- growing magnetoelastic and magnetocaloric thin films on suitable substrates,
- investigating the properties of these thin films,
- studying the influence of deposition conditions on properties of thin films,
- optimising the growth conditions based on the measured properties,
- developing non-destructive techniques for characterising thin films and
- modelling of magnetic properties of magnetoelastic thin films using Jiles-Atherton theory of hysteresis.

This thesis covers three important areas in the material science and engineering of thin films: preparation, characterisation and modelling that give insights and instigate new ideas that will further widen the scope.

1.2 Organisation of the thesis

Chapter 2 gives the overall background of this research work. Magnetoelastic and magnetocaloric effects and materials are discussed in detail. The pulsed-laser deposition technique and the influence of deposition conditions on thin film growth are detailed. An introduction to analytical models of hysteresis is also given.

Chapter 3 elaborates the growth process and characterisation of cobalt ferrite thin films on SiO_2/Si substrates using pulsed-laser deposition. Two series of films: one at different substrate temperatures and the other at different oxygen pressures, have been studied. The origin of perpendicular anisotropy in these thin film structures is investigated. Magnetic annealing of cobalt ferrite thin films to induce in-plane uniaxial anisotropy was studied. The results of magnetostriction measurements on uniaxial anisotropic thin films based on inverse technique are reported.

Chapter 4 presents the first successful production of $Gd_5Si_2Ge_2$ thin films, a magnetocaloric rare earth intermetallic alloy suitable for magnetic refrigeration applications. The magnetic phase transformation in this material can be seen from the magnetic measurements and the results are furnished.

Chapter 5 details the analytical modelling of magnetic properties of materials based on the Jiles-Atherton model of hysteresis. The extensions to the Jiles-Atherton theory which were developed as part of this research work are presented. A comparison between the calculated and measured thermal dependence of hysteresis in substituted cobalt ferrite material is given. The functional form of anhysteretic magnetisation is derived. The procedure to model magnetic two-phase materials using Jiles-Atherton theory is described and the results are explained qualitatively.

Chapter 6 discusses the application of Jiles-Atherton theory to cobalt ferrite thin films. The effects of deposition parameters (substrate temperature and oxygen pressure) on magnetic properties of cobalt ferrite thin films are modelled. The variations of Jiles-Atherton parameters with deposition conditions are studied and the results are furnished.

Chapter 7 lists the conclusions that arise from this research work. It also suggests directions for future work in several areas of magnetic materials and modelling on which this thesis was conducted.

Chapter 2

Background

2.1 Introduction

This chapter gives an overall background of the work that was carried out as a part of this research. Section 2.2 introduces the magnetoelastic effect and the class of materials that exhibit this phenomenon. The origin of magnetoelasticity and previous work on magnetoelastic materials are discussed in the subsequent subsections. Section 2.3 explains the magnetocaloric effect and a rare earth intermetallic alloy that exhibits this effect. Section 2.4 aims at detailed discussions on thin film growth procedures and the techniques to characterise them. The pulsed-laser deposition of thin films and the influence of growth parameters on thin film properties are explained in detail in Section 2.5. Finally, Section 2.6 describes the origin of hysteresis and various models to predict hysteretic behaviour in magnetic materials.

2.2 Magnetoelastic effect

In 1842 Joule observed a change in length of a Nickel sample when subjected to a magnetic field [Joule, 1842]. The reason is, in Nickel, the intensity and orientation of magnetic field causes variations in interatomic distances. This is known as the direct magnetoelastic effect. Although this effect can be found in almost all magnetic materials, only a few show large enough coupling between their magnetic and mechanical properties to make them suitable to be applied as sensors or actuators.

Ferrites are a class of materials developed mainly for high frequency applications as eddy current losses are lower than conventional metallic ferromagnetic materials. Hence they have been investigated for high frequency applications [Snoek, 1936, 1948]. They are basically ferrimagnetic oxides where the magnetic ions whose ionic radii are smaller than oxygen are confined to particular interstitial crystallographic sites within the lattice. The super-exchange coupling, an interaction between the magnetic ions through the oxygen atom situated between them, is the cause of ferrimagnetic ordering in these materials. Hence oxygen deficient ferrites are likely to show lower saturation magnetisation due to weaker super-exchange coupling than those that have sufficient oxygen to help achieve a ferrimagnetic ordered state. Ferrites can be broadly classified based on their crystallographic structures: spinel, perovskite, garnet and hexa ferrites.

Cobalt ferrite is a magnetoelastic material that belongs to the class of spinel ferrites. This material was not extensively studied until recently. However, lately, there has been a tremendous increase in the research on cobalt ferrite

due to their magnetoelastic properties which can be utilised in sensor applications. As an important part of this study is based on thin film growth and characterisation of cobalt ferrite, a major part of this chapter is focused on spinel ferrites.

2.2.1 Spinel ferrites

Spinel ferrites are a class of ferrimagnetic oxide materials with chemical formula $MO.Fe_2O_3$ or more generally MN_2O_4, where M represents one of the metal ions with divalent state or a combination of metal ions with an average valence state of two and N represents trivalent metal ions or a combination (often all or partially Fe^{3+}). They possess the crystal structure of the mineral spinel $MgAl_2O_4$ and hence the name 'spinel ferrites'. The smallest cubic cell of spinel lattice has eight molecules of MN_2O_4 in which 32 oxygen atoms form a face centred cubic (fcc) lattice. Two types of interstitial sites occur in this cubic lattice: 8-tetrahedral (A) and 16-octahedral (B). The 8 M^{2+} and 16 Fe^{3+} ions are distributed among A and B sites. The moments of A and B sites are anitparallel to each other. The cubic cell is shown in Fig. 2.1. The octants with their occupied metal ions and oxygen ions are represented in the schematic. The structure of metal ions is the same in all diagonally opposite octants.

Spinel ferrites can be classified as normal and inverse, depending on the site occupancy of the M^{2+} and Fe^{3+} ions. In normal spinels, all the M^{2+} ions are located at the A sites and all the Fe^{3+} ions are located at the B sites whereas, in the inverse spinel structure, all M^{2+} ions are located at the B sites and Fe^{3+} ions are equally distributed between A and B sites. Although normal and inverse

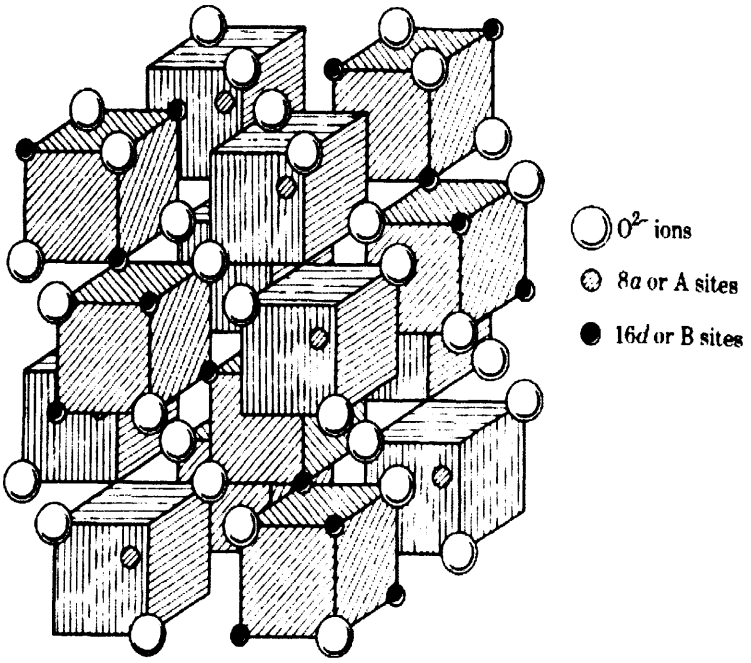

Figure 2.1: An illustration of a cubic spinel structure [Chikazumi, 1997].

are the two extreme cases of spinel ferrites, there is a variety of behaviour in-between them.

The distribution of ions in both A and B sites can be mathematically represented as [Chikazumi, 1984]

$$[Fe^{3+}_{2\delta} M^{2+}_{1-2\delta}]O.(Fe^{3+}_{2(1-\delta)} M^{2+}_{2\delta})O_3 \tag{2.1}$$

where δ is a measure of the inversion. For a normal spinel, $\delta = 0$ and for an inverse spinel, $\delta = 0.5$.

It is well known that spinel ferrites demonstrate magnetoelasticity under the application of magnetic field. Magnetoelastic materials deform under the influence of applied magnetic field. Typically, the magnetoelasticity in ferrites

is very small, but there are a few exceptions (most notably cobalt-containing ferrites). The magnetoelastic coupling is influenced by various factors: electron states, crystallographic ordering, oxidation states and stoichiometry. Hence the interpretation of magnetoelasticity in spinel ferrites is a complex task. Tsuya has thoroughly studied the microscopic origin of magnetoelasticity in spinel ferrites [Tsuya, 1958]. Spinel ferrites have been well-studied and a review of their properties can be found in [du Tremolet de Lacheisserie, 1993].

Cobalt ferrite, among other spinel ferrites has partially inverse spinel structure and possesses high magnetoelastic coupling (of the order of 10^{-4}) [Weil, 1952]. This coupling was later found to vary with the heat treatment [Gumen, 1966], anisotropy and composition [Belov et al., 1989]. The anisotropy energy of cobalt ferrite is very large compared with other spinel ferrites and its easy axes of magnetisation lie in the [100] directions.

The source of anisotropy energy in ferrites was calculated by Yosida and Tachiki [Yosida & Tachiki, 1957]. It was concluded that the major part of anisotropy energy of cobalt ferrite arises from Co^{2+} ions in the B site, whereas the anisotropy energy of nickel ferrite comes from Fe^{3+} ions and the anisotropy energy of magnetite comes from Fe^{2+} ions in the B sites. It was also reported that substituting cobalt for the divalent metallic ions in ferrites changes the easy axis direction from [111] to [100] [Slonczewski, 1958]. Theoretical investigations of the magnetic anisotropy of ferrites have also been carried out by Wolf [Wolf, 1957] and Slonczewski [Slonczewski, 1958].

Studies were carried out to improve magnetic and magnetoelastic properties of cobalt ferrite by cation substitutions. The net magnetic moment in ferrites is the difference in magnetic moments between the B and A sublattices.

Hence by substituting a non-magnetic cation which has A site preference, the net magnetic moment of the material can be increased. However, this also changes the exchange coupling. On the other hand, by substituting a cation onto the B site, the net magnetic moment can be varied (mainly decreased) with less change in the exchange coupling. In substituted ferrites, in order to achieve higher sensitivity, i.e. change in magnetostriction with applied field $\left(\frac{d\lambda}{dH}\right)$, anisotropy should be made to decrease faster than magnetostriction.

The effects of substituting cations such as Mn^{3+}, Cr^{3+}, Ge^{4+}, and Ga^{3+} in cobalt ferrite were investigated by Song [Song, 2007]. Subsequently the temperature dependence and anisotropy of Ge^{4+} and Ga^{3+} substituted cobalt ferrites were measured by Ranvah et al. [Ranvah et al., 2008, 2009a]. Recently, Al^{3+} has been substituted in cobalt ferrite and its temperature dependent magnetic properties have been studied [Ranvah et al., 2009b]. The above investigations showed that of all other cations, the substitution of Ge^{4+} cation was effective. The Ge^{4+} substituted cobalt ferrite has reduced anisotropy and coercivity while it also showed an increased sensitivity, i.e. the strain derivative.

Some magnetic materials, when heat treated in the presence of a magnetic field are known to develop a uniaxial magnetic anisotropy. This process is widely known today as magnetic annealing. In certain classes of materials (including cobalt ferrite), this is thought to take place due to directional order [Cullity & Graham, 2009]. In 1933, Kato and Takei showed that the mixed oxides of cobalt and iron respond to heat treatments in the presence of a magnetic field [Kato & Takei, 1933]. A detailed study of magnetic annealing of ferrites was made by Bozorth et al. [Bozorth et al., 1955]. The magnetomechanical properties of cobalt ferrite were found to improve with magnetic annealing. It

was shown by Lo et al. that the magnetostriction and the strain derivative improved in bulk cobalt ferrite after magnetically annealing at 300 °C for 36 hrs in the presence of a magnetic field of ~318 kA/m (4 kOe) [Lo et al., 2005].

The exceptional magnetic and magnetoelastic properties of cobalt ferrite and its derivatives in bulk form and the ability to tailor the magnetic and magnetoelastic characteristics to suit the requirements have sparked much research interest in cobalt ferrite and shown its potential for a wide range of applications. Researchers have been able to reproduce some of these qualities of bulk cobalt ferrite in thin film form. Chapter 3 of this thesis explains the growth procedure and characterisation of cobalt ferrite thin films using pulsed-laser deposition (PLD) and compares the results, where available, with its bulk form.

2.3 Magnetocaloric effect

The magnetocaloric effect is a phenomenon that couples magnetic and thermodynamic processes in a material where a reversible change in temperature is caused by a changing magnetic field. This is also known as adiabatic demagnetisation. The effect was first observed by the German physicist Warburg [Warburg, 1881] in pure iron and the fundamental principle was explained later [Debye, 1926; Giauque, 1927]. Although most ferromagnetic materials exhibit a change in temperature under the influence of magnetic field, the magnetocaloric effect in most materials is not well-pronounced enough for applications.

The magnetocaloric effect can be used for cooling and the magnetocaloric refrigeration cycle can be described as:

- Increase in the temperature of magnetocaloric materials under the influence of increasing magnetic field in an adiabatic condition.
- Releasing the generated heat by means of natural or forced convection of air or any fluid.
- Removal of the external magnetic field adiabatically when the material is at room temperature reduces the temperature of the material.
- The material then extracts heat from the region to be cooled, thereby cooling it.

The magnetocaloric materials can be broadly divided into three categories based on the temperature range at which they exhibit the magnetocaloric effect:

- low temperature (~10 - 80 K),
- intermediate temperature (80 - 250 K) and
- near room temperature.

Pure rare earth metals such as neodymium (Nd), erbium (Er) and thullium (Tm) exhibit magnetocaloric effect in the low temperature range as they achieve magnetic ordering at low temperatures. The magnetocaloric effect in these materials was found to be, for e.g. in Nd, the adiabatic temperature change is only $\Delta T_{ad} \approx 2.5$ K at T = 10 K for a 8000 kA/m (μ_0H=10 T) increase in magnetic field. This is due to the difficulty in magnetising them in a magnetic field [Zimm et al., 1989, 1990].

The magnetocaloric effect in the intermediate temperatures is not well-studied since there are not many applications in this temperature range of 80 - 250 K. Benford found that pure dysprosium (Dy) with $\Delta T_{ad} \sim 12$ K at T $\sim$ 180 K for a 5600 kA/m (μ_0H=7 T) increase in magnetic field, is one of the best magnetocaloric materials in this range with a field dependence of $\sim$1.7 K/T [Benford, 1979].

2.3.1 $Gd_5(Si_xGe_{1-x})_4$ alloys

The near room temperature magnetocaloric effect has been thoroughly investigated recently due to the possibility of magnetic refrigeration applications. Gadolinium (Gd) is a preferred refrigerant material near room temperature as its magnetic ordering occurs at T_c = 294 K. Hence Gd and its alloys have been extensively studied. At T_c, a change in adiabatic temperature of 20 K can be achieved in Gd for a magnetic field change of 8000 kA/m (μ_0H=10 T) with a field dependence of 2 K/T [Dan'kov et al., 1998]. Intermetallic compounds, such as Y_2Fe_{17} and Nd_2Fe_{17}, whose magnetic ordering is also near room temperature were shown to exhibit lower magnetocaloric effect than Gd until the discovery of giant magnetocaloric effect in $Gd_5(Si_xGe_{1-x})_4$ alloys [Pecharsky & Gschneidner Jr., 1997a]. The adiabatic temperature change in these intermetallic alloys was found to be at least 30% higher than that of Gd and the field dependence was $\sim$5 K/T.

Pecharsky and Gschneidner published the phase diagram of $Gd_5(Si_xGe_{1-x})_4$ alloys at zero field [Pecharsky et al., 2002]. The phase diagram shown in Fig. 2.2 has three different ranges of varying composition:

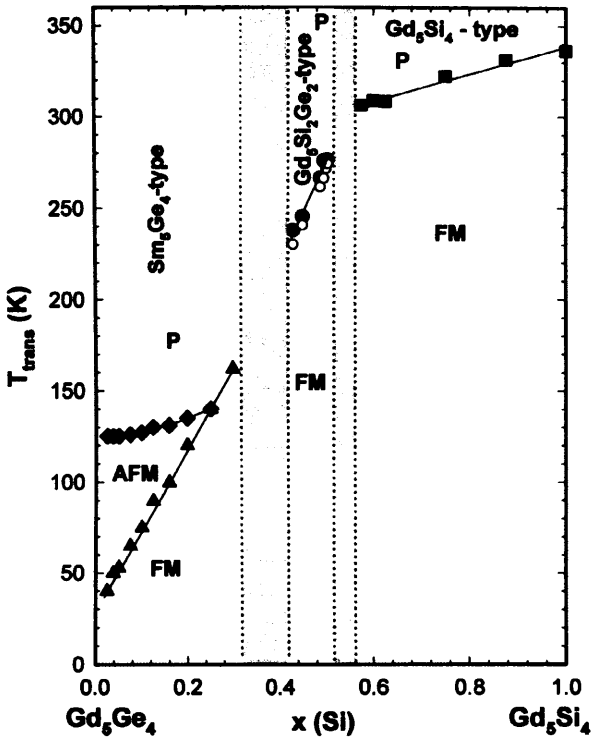

Figure 2.2: Phase diagram of $Gd_5(Si_xGe_{1-x})_4$ alloys [Pecharsky et al., 2002].

- $0.575 < x \leq 1$: A silicon-rich orthorhombic phase, O(I), of type Gd_5Si_4 (space group P_{nma}) with a second order paramagnetic (PM) to ferromagnetic (FM) phase transition.

- $0.4 < x \leq 0.51$: This composition range exhibits a first order magnetostructural phase transformation at temperatures ranging between 225 K (x = 0.4) to 276 K (x = 0.5) from a high temperature PM phase with monoclinic structure (space group $P112_1/a$) to a low temperature FM phase with orthorhombic structure, O(I).

- $x \leq 0.32$: For the germanium-rich compound, second order PM to antiferromagnetic (AF) transition occurs at temperatures between 125 K (x

= 0) and 135 K (x = 0.2).The AF-FM transition occurs simultaneously with a first-order structural transformation from a high-temperature orthorhombic phase, O(II), of type Sm_5Ge_4 (space group P_{nma}) to the low-temperature O(I) phase. It was also shown that in the range $0.24 < x < 0.32$ the second order PM-AF transition disappears leading to the coexistence of O(II) and O(I) phases [Pecharsky & Gschneidner Jr., 1997b].

The stabilisation of crystallographic structures which influence the magnetocaloric effect in $Gd_5(Si_xGe_{1-x})_4$ alloys is quite complex. It depends mainly on the heat treatments of the samples and the purity of the components [Pecharsky et al., 2003]. A detailed review of the high temperature heat treatments on $Gd_5Si_2Ge_2$ can be found in Ref. [Mozharivskyj et al., 2005].

From the metallurgical phase diagrams shown in Figs 2.3(a) and 2.3(b), the 5:4 phases solidify through a peritectic reaction. However, a slow cooling process may yield the secondary phases such as the 5:3 and 1:1. Hence the quenching rate is also an important factor to be considered in order to achieve the right phase and microstructure in bulk materials [Pereira et al., 2008].

It is important to mention that although the magnetocaloric effect in $Gd_5(Si_xGe_{1-x})_4$ alloys has been extensively studied and investigated for more than ten years since its discovery in 1997, there have been no reports of successful growth of thin films of this alloy until now. There was a report of an unsuccessful attempt by Sambandam et al. to grow $Gd_5Si_2Ge_2$ on silicon substrates [Sambandam et al., 2005], which is the only reported thin film work on this alloy found in the literature.

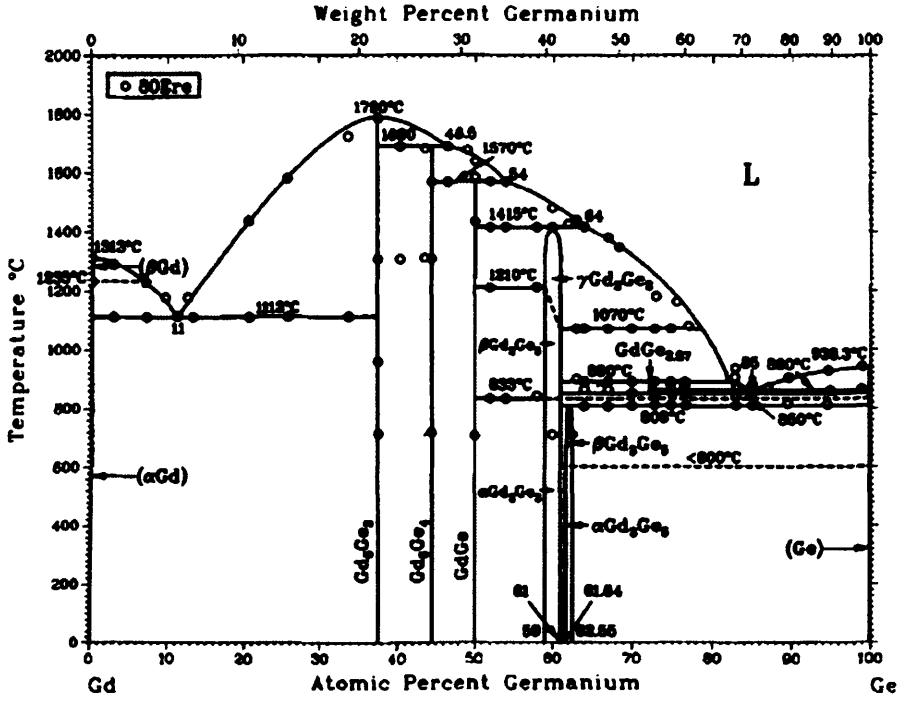

(a)

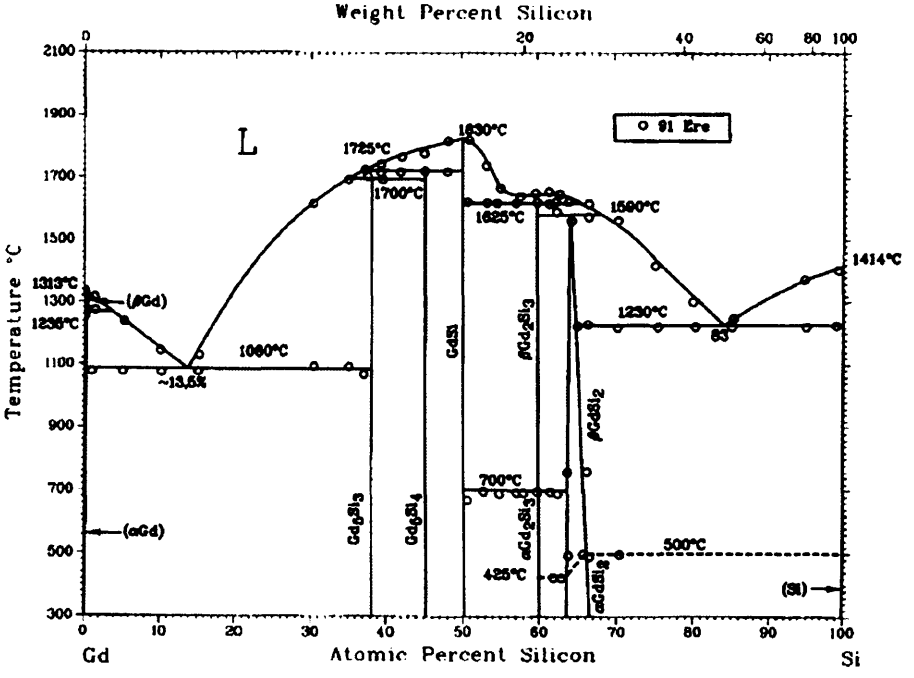

(b)

Figure 2.3: Metallurgical phase diagrams of (a) GdGe [Predel, 1991] (b) GdSi [Okamoto, 1995].

2.4 Thin film growth and characterisation

Today, thin films have been exploited to a large extent and are constantly being engineered to suit many applications. The quality of thin films, which influences their properties, is highly dependent on the growth process. Hence selecting the right technique to grow thin films is advantageous. Thin film growth techniques can be broadly classified into two categories: physical vapour deposition (PVD) and chemical vapour deposition (CVD). PVD involves purely physical processes such as high temperature vacuum evaporation or plasma sputter bombardment of a target material whereas CVD involves chemical reaction at the surface to be coated. Thin film deposition techniques based on PVD are listed in Table 2.1.

Table 2.1: Thin film deposition techniques based on PVD

Deposition technique	Description
Evaporation	Electrically resistive heating in high vacuum
Electron beam	Electron bombardment in high vacuum
Sputtering	Plasma discharge bombardment in high vacuum
Pulsed-laser	Laser ablation in high vacuum

2.5 Pulsed-laser deposition

This section focuses on growing high quality thin films using the pulsed-laser deposition (PLD) technique, and the influence of deposition parameters on thin film properties. In this thesis, all thin films were prepared using the PLD

technique. In both concept and practice, PLD is the most versatile and simple among the thin film deposition techniques discussed in Table 2.1. A simplified schematic of a PLD set-up is shown in Fig. 2.4. The system consists of target and substrate holders inside a vacuum chamber. As this is a high vacuum chamber, the pressure can reach as low as 10^{-8} Torr.

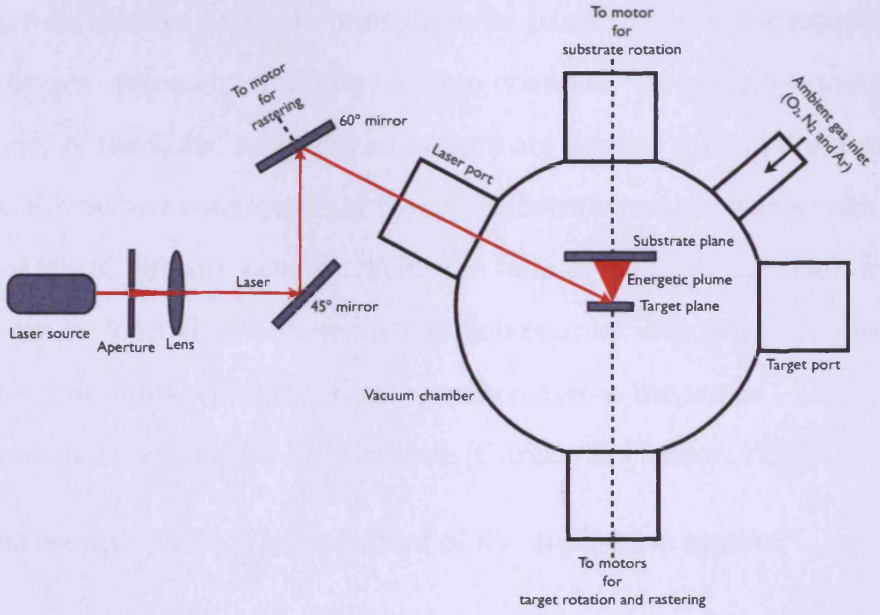

Figure 2.4: A simplified schematic of the PLD setup to deposit thin films.

PLD can be described as a three-step growth process involving:

1. an excimer pulsed-laser beam with high power which is made to focus on the target material;

2. the target material, which on absorbing the laser energy, vapourises and forms a laser plume;

3. the plume, consisting of a mixture of energetic species such as ions, atoms,

molecules etc., which rapidly expands from the target surface to vacuum forming a nozzle jet, which is then deposited on the substrate.

The deposition is very forward-directed and is normal to the surface of the target. An optics train consisting of mirrors, lenses and apertures, is used to focus and raster the laser beam on the surface of the target. Thin films can be grown in reactive or inert atmosphere by passing gases, for example oxygen, nitrogen, argon etc., into the vacuum chamber. In order to maintain homogeneity of the films, substrate and target are rotated during the deposition process. Films can be deposited at various substrate temperatures with a maximum of 950 °C (in our system). With the help of a target carousel, multiple targets can be loaded simultaneously which enables deposition of multilayer structures and films with graded composition across the wafer.

The main advantages of PLD include [Chrisey & Hubler, 1994]:

- the energy source is independent of the deposition system,
- complex multilayer and graded composition films can be produced easily,
- cost-effectiveness.

Unlike other methods, PLD has the major advantage of producing thin films whose average composition equals the target composition.

The generation and presence of particulates in thin films prepared by PLD have been an obstacle in applying the technique to some applications. Although PLD is good at producing films with correct average stoichiometry, there are a number of deposition parameters to be considered and fine-tuned

in order to achieve single phase films and the right structure and nanostructure in thin films.

2.5.1 Influence of deposition parameters

The influence of main deposition parameters such as target topography, laser fluence, ambient gas pressure and substrate temperature on thin film growth and composition is explained in this section. It is necessary to set these parameters so as to gain complete control over the quality, stoichiometry, structure and micro or nanostructure of thin films grown using PLD technique.

2.5.1.1 Target surface

The laser irradiation at high fluence (i.e. laser energy density) and power modifies the target surface. The thermal cycle induced by the laser pulse on the target surface can be explained as a series of phenomena: absorption of laser pulse, target vapourisation, capillary wave formation and solidification. The surface modifications by lasers were reported as early as mid-60's [Birnbaum, 1965].The target surface topography, modified by the frozen capillary waves, contains irregular structures such as ripples, ridges and cones as shown in Fig. 2.5.

It was observed in both sputtering [Auciello et al., 1988] and PLD [Foltyn et al., 1991] of YBCO films that the target surface modification plays a crucial role in film composition and deposition rate. Foote et al. found that initially at low exposures the films were copper- and barium-rich. Once the exposure is $\approx$40 shots/site, the composition reaches steady state [Foote et al.,

1992]. The decrease in deposition rate is due to the reduction in target material being vapourised and this trend stops when cones have been completely formed [Krajnovich & Vázquez, 1993].

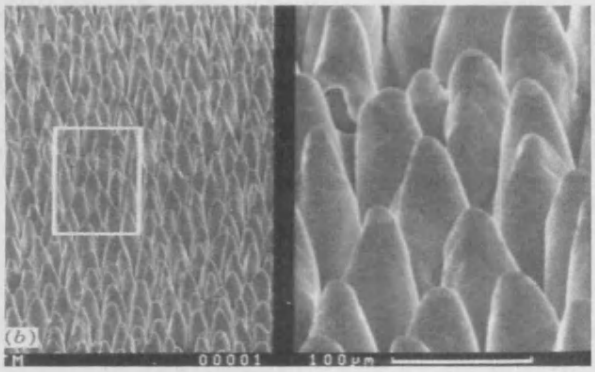

Figure 2.5: Scanning electron micrograph of the modified surface of a YBCO target exposed at 308 nm to 1000 shots/site at a fluence of 5.6 J/cm^2 [Chrisey & Hubler, 1994].

Variation in the angular distribution of the ablated material implies that different components contained in the plume have different angular distributions with respect to the deposition axis. The film stoichiometry is known to be uniform only within a smaller range of angles about the deposition axis. Target cratering also influences the angular distribution of the ablated material [Chrisey & Hubler, 1994].

Laser preconditioning of the target is necessary before every deposition in order to achieve the required composition and uniformity and stable deposition rate.

2.5.1.2 Laser fluence

Particulate generation is a very important factor to be considered in thin film growth. The particulate generation depends on various parameters such as

process conditions, type of material etc., and laser fluence or energy density has a considerable effect on the particulate size and density [Chrisey & Hubler, 1994]. The laser energy density is mainly determined by the laser spot size and laser energy. For any given laser wavelength, there is a threshold laser fluence below which particulates cannot be observed and above which the particulate density increases rapidly. Blank et al. found that for a 308 nm XeCl excimer laser with 20 ns pulse duration the threshold laser fluence is 0.9 J/cm^2 [Blank et al., 1992].

The laser fluence also affects deposited film thickness. In simple relation, film thickness can be represented as

$$d \propto S^2 E \tag{2.2}$$

where S is the laser spot size (usually the diameter of the laser spot) and E is the laser energy density. The other parameters that determine the thickness are laser repetition rate and the duration of deposition. The higher the repetition rate of the laser pulse and the longer the deposition duration the thicker are the films. Film thicknesses of $> 1\ \mu m$ can be grown.

The angular distribution of the plume was found to be independent of laser fluence in a wide range of materials [Foltyn et al., 1991; Neifeld et al., 1988; Scheibe et al., 1990].

2.5.1.3 Laser wavelength

The amount of laser power absorbed by the target when irradiated is determined by the light wavelength. The absorption coefficients of metals decrease

with decreasing wavelength. So, the penetration depth of light in metal targets is larger in the ultraviolet (UV) region than in the infrared (IR) region. The reverse is true for oxide superconductors. It has been shown that the particulate size and density are higher for YBCO films prepared using IR laser as compared to UV laser [Dyer et al., 1992; Koren et al., 1989]. The variation in the particulate size is likely to be due to the difference in absorption coefficient of the target at different wavelengths.

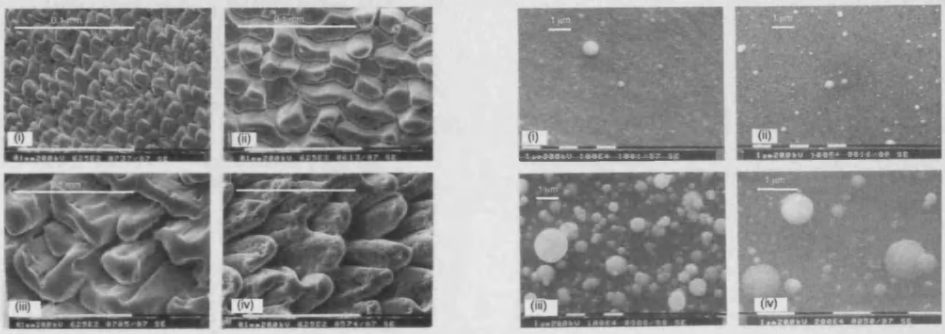

(a) (b)

Figure 2.6: SEM images of YBCO (a) target surfaces and (b) the corresponding thin films deposited using PLD at different wavelengths (i) 266 nm, (ii) 355 nm, (iii) 533 nm and (iv) 1064 nm [Kautek et al., 1990].

Another interesting study by Kautek et al. correlated the particulate sizes on the deposited YBCO thin film to the target surface irradiated with laser pulses at different wavelengths [Kautek et al., 1990]. Figures 2.6(a) and 2.6(b) show respectively the scanning electron microscopy (SEM) images of the target surface irradiated to a laser peak power of 0.79 GW/cm^2 and the corresponding thin film surface deposited at laser wavelengths (i) 266 nm, (ii) 355 nm, (iii) 533 nm and (iv) 1064 nm. As the wavelength increases, the depth of penetration of light on the target increases forming deeper grooves. It is evident

from Fig. 2.6(b) that the penetration depth has a significant effect on particulate size and density. Ideally, a wavelength that is strongly absorbed and has shallow penetration depth is desired to ablate materials with minimum particulate generation.

2.5.1.4 Target-to-substrate distance

The target-to-substrate distance, and pressure in chamber, vary the angular distribution of the plume. In the presence of ambient gas, the plume length decreases due to collisions between the laser plume and ambient gas. The laser plume length (L) can be represented as a function of laser energy density (E) and ambient pressure (P_0) [Dyer et al., 1990]

$$L \propto \left(\frac{E}{P_0}\right)^{\frac{1}{3\gamma}} \tag{2.3}$$

where $\gamma = \frac{C_p}{C_v}$ is the ratio of specific heats of ambient gas at constant pressure and volume (for oxygen, argon and nitrogen, $\gamma \approx 1.4$, 1.7 and 1.4 respectively).

When the target-to-substrate distance is much smaller than L, there is no considerable variation in particulate size and density. It was found that as the distance between the target and substrate increases, the number of smaller particulates decreases and the number of larger particulates increases indicating a merging of particulates during flight [Nishikawa et al., 1991]. When the target-to-substrate distance is much greater than L, the adhesion of the ejected species to the substrate becomes poor [Chrisey & Hubler, 1994].

2.5.1.5 Ambient gas

In order to compensate for the loss of constituent elements such as oxygen or nitrogen in deposited thin films, a reactive ambient atmosphere is necessary during the deposition process. The creation of O_2, N_2 and H_2 atmosphere inside the PLD chamber enables the growth of oxide, nitride and hydride films from metallic targets. Recently oxidants such as N_2O, NO_2 and O_3 have been shown to be very effective as far as the growth of superconducting oxide films are concerned.

The particulate size depends on the pressure of the ambient gas. It was found by Matsunawa et al. that, in the production of various ultra-fine metals and alloys in the presence of argon atmosphere, a decrease in ambient gas pressure reduces the particulate size [Matsunawa et al., 1986]. The effect of ambient gas atmosphere on the nature of particulates can be related to the increased collisions between the ejected species and ambient gas species at higher ambient gas pressures.

The growth mechanism of particles in the presence of ambient gas is by diffusion and so the particulate size is determined by the residence time of the particulate in vapour species [Chrisey & Hubler, 1994]. In the PLD of thin films in vacuum, where there are virtually no collisions, particulates are predominantly formed from solidified liquid droplets expelled from the target.

As explained earlier, in the presence of ambient gas, the ejected vapour species undergo collisions. Hence the plume angular distribution is perturbed and the ejected particles deviate from their initial projected trajectories. This phenomena broadens the angular distribution of the plume thereby reducing

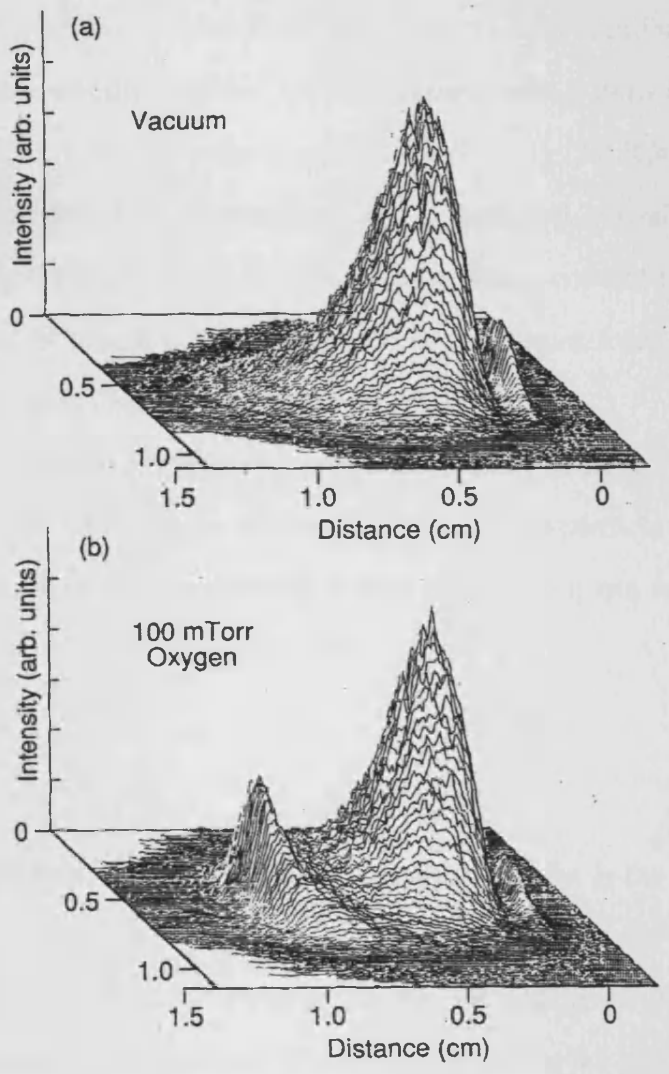

Figure 2.7: Laser plume intensity in vacuum and collision-induced broadening at 100 mTorr of ambient oxygen pressure captured using an ICCD camera at Δt=1 μs following 1 J/cm^2 KrF-laser ablation of YBCO target. The distance corresponds to the plume width and the intensity corresponds to the perpendicular distance away from the target [Geohegan, 1992].

the deposition rate.

The collision-induced broadening effect emission intensity at Δt=1 μs following 1 J/cm^2 KrF-laser ablation of YBCO target was captured using a fast intensified charge-coupled device (ICCD) camera array detector in vacuum and at 100 mTorr of oxygen pressure are shown in Fig. 2.7 [Geohegan, 1992]. At 100 mTorr oxygen, a third component of the plasma emission appears on the leading edge of the expanding plasma as a sharp contact front of greater radius of curvature which is highly suggestive of a shock front formation due to background gas collisions.

The broadening effects induced by collisions between ambient gas and ejected species begin to occur when the mean free path (Λ) of a particle in the ambient gas is less than the target-to-substrate distance (h). The mean free path can be approximated as [Chrisey & Hubler, 1994]

$$\Lambda \approx \frac{1}{\sqrt{2}n\sigma} \tag{2.4}$$

where n is the number density of the ambient gas and σ is the collision cross section.

The reduction in mean free path of the ejected species as the ambient gas pressure increases (approximately 50 mm at 1 mTorr to 0.5 mm at 100 mTorr) indicates that, at high ambient gas pressures, the ejected vapour species undergo enough collisions to form particulates even before they reach the substrate. It was found experimentally that collision-induced broadening occurs at pressures only above ~22 mTorr [Gorbunov & Konov, 1991].

In the growth of multicomponent oxide films, oxygen pressure also plays

an important role in achieving the desired phase in the deposited films. In the growth of $LiNbO_3$ films, as Li atoms are much lighter than Nb, Li atoms are readily scattered in collisions with the background gas [Chrisey & Hubler, 1994]. This results in growth of Nb-rich multiphase films. Hence control of the reactive ambient gas gives a good control over composition of the deposited film.

2.5.1.6 Substrate temperature

The influence of substrate temperature on the crystal structure and stoichiometry of the deposited film has been investigated by Metev et al. [Metev & Meteva, 1989]. The investigation showed that at given deposition conditions there exists a critical substrate temperature below which the films are not crystalline and also below which the composition of the films deviates from the target stoichiometry. The substrate temperature determines the heat loss of the condensate through the substrate, i.e. the speed of crystallisation. At temperatures below the critical point, the velocity of crystallisation is very low as the cooling rate is higher. So, not all adatoms (adsorbed atoms or atoms that lie on the crystal surface) form crystallites. On the arrival of the next vapour species, due to the rise in temperature, the unbonded atoms re-evaporate leaving a particular cation-rich stoichiometry in a multicomponent film. When the temperature is higher than the critical temperature, the cooling rate decreases leading to crystallisation of all adatoms. Hence the substrate temperature is also a critical parameter to preserve stoichiometry in multicomponent thin films.

2.5.2 Stress in thin films

During the growth process, thin films can often develop large stresses. The origin of stress in thin films can be broadly divided into strains developed:

1. within the film,
2. at the film-substrate interface and
3. due to dynamic processess.

Grain boundaries, impurities, dislocations and other types of defects in the film can contribute to the intrinsic strain developed within the film. The strain at the film-substrate interface can be attributed to thermal expansion mismatch and lattice mismatch between the film and substrate. Interdiffusion and recrystallisation in thin films also contribute to the intrinsic strain in thin films.

It is important to consider the stress levels on film-substrate bilayer as the magnitude of stress was found to play an important role in determining both surface morphology and magnetic properties of thin films [Koch, 1994].

2.5.3 Characterisation

In this study, thin films prepared by PLD were characterised in order to help understand their structure, orientation, composition, morphology, magnetic and domain features. The properties measured and the techniques used are listed in Table 2.2.

Table 2.2: Thin film characterisation techniques used in this study.

Characterisation	Technique used
Crystallography	X-ray diffraction (XRD)
Composition	Energy dispersive X-ray spectroscopy (EDX)
Deposition rate	Cross-sectional scanning electron microscopy (SEM)
Magnetic hysteresis	Vibrating sample magnetometer (VSM)
Magnetostriction	Vibrating sample magnetometer (inverse technique)
Surface morphology	Atomic force microscopy (AFM)
Magnetic domain structure	Magnetic force microscopy (MFM)

2.5.3.1 Crystallography

X-ray diffraction (XRD) is a non-destructive technique to identify crystalline phase and orientation of a material. The technique is based on the interference pattern of X-rays scattered by crystals as explained by Bragg [Bragg, 1920]. The atoms in a crystal are arranged in a regular pattern. When an X-ray beam hits the crystal plane, there will be constructive interference in particular directions and there will be well defined diffracted X-ray beams leaving the sample in various directions. Hence, a diffracted beam is composed of a large number of scattered rays from the crystal mutually reinforcing one another. The peaks of the diffraction pattern of many materials can be identified using the powder diffraction file (PDF) database. The crystallographic properties were characterised using a Philips-PW1710 XRD system. This used a Cu K_α radiation at wavelength of $\sim$0.154 nm. All samples were scanned from 10° to 80° (2θ) with a step size of 0.02° at 35 KV, 40 mA and scanning speed 20 steps/min.

2.5.3.2 Composition

The stoichiometry of the thin films was determined using energy dispersive X-ray (EDX) spectroscopy. The composition was averaged over 15 locations on the surface of the thin films. In oxide films, the content of oxygen can be accurately determined using sophisticated techniques such as Xray photoelectron spectroscopy (XPS). However, in this study, the oxygen content was assumed to be the expected stoichiometric value.

2.5.3.3 Deposition rate

The thickness of the thin films and hence the deposition rate of the system was found from cross-sectional imaging of the film samples in high magnification scanning electron microscopy (SEM). All of the oxide films were deposited on silicon substrates that had a 300 nm thick thermal oxide layer on top. The layers of deposited thin film, thermal oxide and the substrate can be seen in the cross-sectional image obtained from SEM shown in Fig. 2.8.

2.5.3.4 Magnetic hysteresis

The characterisation of magnetic hysteresis, a measure of magnetisation of the sample at different applied magnetic fields, is very important in the investigation of magnetic materials. Although this can be done using several techniques, a vibrating-sample magnetometer (VSM) [Foner, 1959] was used in this study. When a magnetic sample is continuously vibrated, it induces a flux change or alternating electromotive force (emf) in the detection coils as shown in Fig 2.9. The vibrating rod also carries a reference specimen, usually a small

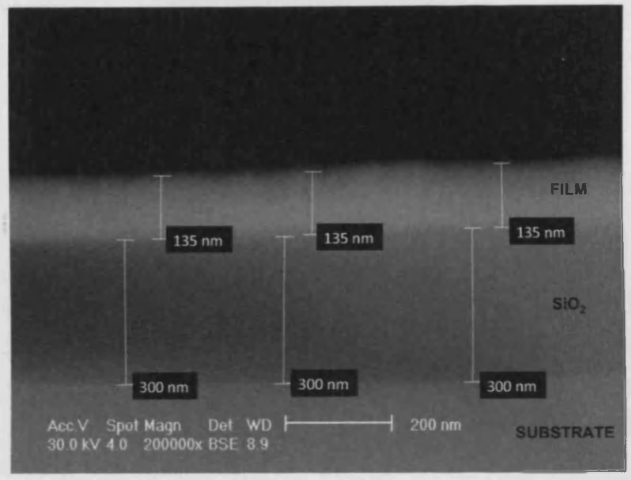

Figure 2.8: Cross-sectional SEM image of a typical thin film.

permanent magnet whose oscillating field induces another an emf in the reference coils. The difference between the voltages induced in two sets of coils is directly proportional to the magnetic moment of the sample.

Magnetic hysteresis measurements were made on a LakeShore model 7400 VSM system at room temperature. The VSM system was calibrated using a Nickel thin film of size 5 mm x 5 mm whose magnetic properties are known. Thin film samples of appropriate sizes (typically 5 mm x 5 mm) were prepared by scribing and breaking 2″ diameter film-substrate wafers prepared using PLD technique. As all thin films are deposited on thick substrates (~300 μm), background subtraction is necessary in order to precisely determine the magnetic properties of thin films without background distortion. Hence the substrates of sizes 5 mm x 5 mm were prepared and their responses to magnetic fields were measured on the VSM before measuring the film-substrate bi-layer. The measured response of the substrate is then subtracted from the

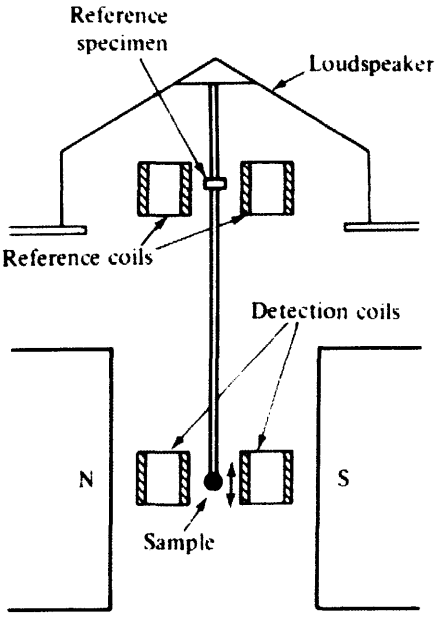

Figure 2.9: Schematic of a vibrating sample magnetometer [Foner, 1959].

film-substrate bi-layer measurement, in order to get the net response of thin films to applied magnetic fields.

2.5.3.5 Magnetostriction

The magnetostriction of thin films can be determined by using direct and inverse techniques. In the direct technique, the sample is subjected to an external magnetic field. The applied magnetic field induces strain in the magnetoelastic sample and causes the bending of the film-substrate bi-layer. By measuring the deflection by means of an optical setup the magnetostriction of the material can be calculated [Tam & Schroeder, 1989]. In the inverse technique, a known stress is applied to the sample and the change in anisotropy field is measured. This change in the anisotropy field is related to the magnetostriction of the material. In this study magnetostriction was measured on thin film samples using

the inverse technique.

In order to measure magnetostriction based on the inverse technique, a VSM sample holder with a 3-point bender assembly was designed in order to apply a known amount of strain on thin films. This bender was designed specifically for this project. The bender assembly was made from a light-weight ceramic material and was non-magnetic. The bender was fit to the VSM vibrating rod so as to measure the anisotropy field of the material in both zero-applied stress and applied stress state. The magnetostriction can then be calculated from [O'Handley, 2000]

$$\lambda_s = \frac{\Delta H_k}{\epsilon} \frac{M_s(1-v^2)}{3Y_f} \tag{2.5}$$

where ΔH_k is the difference in anisotropy field between zero-stress and stressed state, M_s is the saturation magnetisation of the material, v is Poisson's ratio of film, ϵ is the applied mechanical strain and Y_f is the Young's modulus of the film. Poisson's ratio is a measure of the Poisson effect in which a material compressed in one direction tends to expand in the other two directions. It is the ratio between the fraction of expansion and the fraction of compression in a material that is compressed in one direction.

The inverse technique relies on the assumption that the magnetic moments are in the plane of the material and that there is no perpendicular anisotropy. It can only be applied to materials that have an in-plane uniaxial anisotropy, because it relies on measurement of hard axis hysteresis loops to determine H_k.

The inverse magnetostriction technique was validated against the direct

technique using four thin film samples of different compositions: $Co_{95}Fe_5$, $Co_{60}Fe_{20}B_{20}$, $Ni_{65}Fe_{15}Co_{20}$, and $Ni_{80}Fe_{20}$, representing both positive and negative magnetostriction, and having saturation magnetostriction of magnitudes ranging from 10^{-7} to 10^{-5}. The direct measurements were carried out on a high precision optical cantilever beam system and the inverse magnetostriction measurements were carried out on a non-destructive inductive B-H looper with three-point bending stage. The difference between the measured values of magnetostriction from both techniques was calculated to be less than 18%. This work has been published and a more detailed analysis of this technique and its comparison to the direct technique can be found in [Raghunathan et al., 2009].

2.5.3.6 Surface morphology

Atomic force microscopy (AFM) is a form of scanning probe microscopy (SPM) where a small cantilever probe tip of diameter less than 10 nm is scanned across the sample to obtain information about the sample's surface. The technique to measure topography of the thin film surface involves tapping the surface with the oscillating probe tip. The inter-atomic forces between the probe tip and the sample surface cause the cantilever to deflect as the samples surface topography changes. A laser light reflected from the back of the cantilever measures the deflection which is then transformed into a map of topography.

Thin film surface topography and roughness can be determined by AFM. The grain size can also be calculated from the surface topographical image. The optimum resolution of this technique is about 5 nm lateral and <0.1 nm height [Veeco, 2004].

2.5.3.7 Magnetic domains

Magnetic force microscopy (MFM) is also a form of SPM where the probe tip is coated with a thin film of magnetic material. During scanning, the resonance frequency of the tip shifts in proportion to vertical gradients in the magnetic forces on the tip. The shifts in resonance frequency can be detected by measuring the cantilever's phase of oscillation relative to the piezo drive while the probe scans at a constant height (typically 25 nm) above the sample surface. MFM is a three-step procedure:

- cantilever probe tip traces surface topography on the first trace,
- the tip ascends to a preset lift height (typically 25 nm),
- lifted tip traces topography while responding to magnetic forces.

2.6 Theory of hysteresis

In 1881, Warburg observed irreversibility in the response of iron when subjected to magnetic field [Warburg, 1881]. This phenomenon was claimed to be due to lagging of the materials response behind its stimulus. The term 'hysteresis' was coined by Ewing to represent this behaviour in magnetic materials. Fifty-years later he described hysteresis as the most significant feature of ferromagnetic materials.

> *Of the distinguishing features none is more significant than hysteresis. In my own early experiments it forced itself on my attention at every turn. I became soaked in hysteresis, and was led to invent that name, feeling the*

need of a word that should be sufficiently wide to include not only the phenomena of magnetic retentiveness, but other manifestations of what seemed to be essentially the same thing, though some of them were not associated with any visible magnetic change. [Ewing, 1930]

Hysteresis curves, in general, exhibit the path- or history-dependent response of the material to a stimulus. In ferromagnetism, the magnetising field, H, is the stimulus and magnetisation, M, is the response. The magnetic flux density, B (also known as the magnetic induction) is the vector sum of magnetisation and field:

$$B = \mu_0(H + M) \tag{2.6}$$

According to Ewing [Ewing, 1900], magnetic hysteresis exhibits three distinct stages in one cycle of applied field:

- In the first stage of hysteresis, at very low fields, the response is almost proportional to the applied field and is reversible.
- The second stage is an irreversible process, which involves higher dissipation of energy and a new equilibrium state. It is this state that gives rise to hysteresis.
- The final stage is a state of complete parallelism with the applied field.

At the microscopic level, magnetic hysteresis can be explained as follows:

- In the demagnetised state, the magnetic domains are arranged in such a way that along any direction, there are an equal number of positive and negative components, resulting in no net magnetisation.

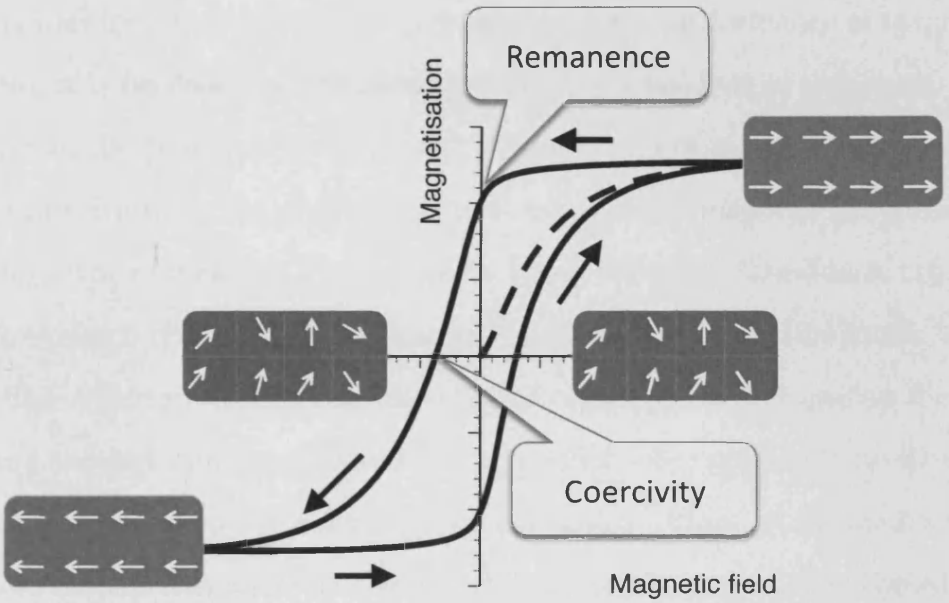

Figure 2.10: A domain-level schematic of a typical magnetic hysteresis.

- At the saturation field, the domains align parallel to the direction of applied field.
- On reducing the field to zero, a considerable amount of domains still have aligned components and hence the material retains substantial amount of magnetisation. This is the basis of magnetic recording media and data storage.
- On further reversing the field to a larger magnitude in the opposite direction, the retained magnetisation can be brought back to a initial state of zero magnetisation. The amount of field that is required to reach a state of no net magnetisation is the coercivity of the system, which together with remanence is widely exploited today in magnetic memory devices.

In order to reduce the design cycle and improve performance of magnetic devices, it is necessary to precisely predict the behaviour of magenetic materials. In the past, there were many attempts to build a hysteresis model. Many of them were not generic and can only predict magnetic properties of a certain type of material. Four models: Landau-Lifshitz [Landau & Lifshitz, 1935], Preisach [Preisach, 1935], Stoner-Wohlfarth [Stoner & Wohlfarth, 1948] and Jiles-Atherton [Jiles & Atherton, 1986], that were developed in the last century showed a prolonged success and are still being applied to predict and understand the magnetic behaviour of various materials. A detailed review of these models was made by Liorzou et al. [Liorzou et al., 2000]. The advantages and disadvantages of the four main hysteresis models are compared in Table 2.3.

Table 2.3: Models of magnetic hysteresis [Liorzou et al., 2000].

Features	Landau-Lifshitz	Stoner-Wohlfarth	Preisach	Jiles-Atherton
Scale	atomic	micro	micro	meso
Mechanism	rotation	rotation	switching	motion
Anisotropy	uniaxial	any	any	any
Interaction	yes	yes	no	yes
Minor loops	yes	yes	yes	approximate
Anhysteresis	yes	yes	yes	yes
Parameters	3	4	3	5
Run-time	very large	average	average	low

The Landau-Lifshitz model was developed to describe the behaviour of individual magnetic moments under the influence of a magnetic field. It was

known, at least at the macroscopic level, that the magnetic moments rotate when a magnetic field is applied. This model was built by applying this idea at the microscopic level of individual magnetic moments, but it was never quite clear on what scale these moments were. The model is really a continuum model, so they are not individual "atomic" moments, but neither are they domains. The behaviour of the entire material can then be determined by integrating the rotation process over the volume. The major practical problem in using this model is the processing time as the calculations have to be made on large number of individual magnetic moments.

The Stoner-Wohlfarth model was built to describe the reorientation of magnetic moments of individual domains by coherent rotation or flipping of all moments within the domain. Unlike Landau-Lifshitz model, this model does not take in to account individual moments. Although the model originally assumed that there were no magnetic interactions between the domains, the model was improved subsequently to incorporate the coupling between domains. The effects of anisotropy on the orientation of magnetisation was also built in to the model.

The Preisach model is an empirical model that describes hysteresis on a macroscopic scale. The model treats hysteresis as summation of a series of switching events occurring at the microscopic level in a material. As this is a mathematical model that treats hysteresis as a mathematical structure, it can be applied to any other physical system that exhibits hysteresis. The main assumption of this model is that each domain in the material has the same magnetisation but different switching fields. Hence the magnetic characteristics are described as a volume fraction of domains with particular combination

of switching fields.

The Jiles-Atherton model was developed based on statistical thermodynamic principles at a multidomain mesoscopic level. The basis of this model is the mechanism of domain boundary movement. The model was shown to perform well in materials with low anisotropy and, with minor modifications, can be applied to axial and planar anisotropic materials. Built on Langevin-Weiss theory, this model assumes that the orientations of magnetic moments are distributed statistically. By integrating the moment distribution over all possible orientations the magnetic characteristics can be obtained. The model also incorporates coupling between magnetic moments in the form of a strong internal magnetic field proportional to magnetisation that tends to align moments in a domain parallel to each other. A more detailed review of this model can be found in Chapter 5 of this thesis.

2.7 Summary

- Magnetoelastic effects and the properties of materials that exhibit these phenomena have been discussed.
- The various thin film deposition techniques have been compared. Pulsed-laser deposition of thin films and the influence of growth parameters on thin film properties have been explained in detail.
- The origin of hysteresis in magnetic materials was described. The four main successful models that are being used to describe and predict hysteresis behaviour in magnetic materials were explained.

Chapter 3

Magnetoelastic thin films

3.1 Introduction

This chapter describes the deposition of magnetoelastic thin films (cobalt ferrite, in particular) using the pulsed-laser deposition technique and the optimisation of the growth process. Section 3.2 reviews the previous work on cobalt ferrite thin films. Section 3.3 explains the present work on the growth of cobalt ferrite thin films on silicon substrates at various substrate temperatures and oxygen pressures and the influence of deposition conditions on the magnetic properties and crystal structure of thin films. Section 3.4 investigates the effect of magnetic annealing on magnetic properties of cobalt ferrite thin films. Section 3.5 elaborates the measurement of magnetostriction in the optimised cobalt ferrite thin film based on the inverse measurement technique.

3.2 Magnetoelastic thin films

Ferrite thin films are applied extensively in microwave magnetic devices. Recently magnetoelastic ferrites have sparked considerable research interest in order to explore the potential for sensor applications. The growth of ferrite thin films range from nanocrystalline or polycrystalline to epitaxial using techniques such as spin-spray coating, electroplating, sputtering, pulsed-laser deposition, evaporation and molecular beam epitaxy. Due to the complexity of the crystal structure of ferrites, structural disorders such as cation vacancies, oxygen deficiencies, non-equilibrium cation distributions, grain boundaries etc., influence the magnetic and electronic properties of the films.

High coercivity, large perpendicular anisotropy, large saturation magnetisation and high resistivity of ferrite thin films have been a focus of perpendicular media applications [Hiratsuka et al., 1997; Zhuang et al., 2000].

$CoFe_2O_4$, a partially inverse spinel structure ferrite is unique among spinel ferrites due to its large magnetic anisotropy along with large anisotropic magnetostriction. The first order magnetocrystalline anisotropy constant (K_1) of $CoFe_2O_4$ is positive (which means that the easy axes are along the (100) directions) and is an order of magnitude greater than other spinel structure ferrites. An analysis with the help of Mössbauer spectroscopy showed that the $CoFe_2O_4$ is not completely inverse spinel and the degree of inversion depends on the heat treatment of the material [Sawatzky et al., 1968]. It was also found that the cation distribution and the strain due to lattice and thermal expansion mismatch between the film and substrate has substantial effect on the properties of $CoFe_2O_4$ thin films [Suzuki, 2001]. The growth of epitaxial $CoFe_2O_4$ thin films

on (100) MgO substrates at high temperatures was found to induce a strong tension in the film and produce a high perpendicular anisotropy [Dorsey et al., 1996]. Antiphase boundaries (APBs) are a kind of structural disorder formed at the interface of ordered regions where the structures at either side of the boundary are "out-of-phase". APBs were found in $CoFe_2O_4$ thin films deposited directly on MgO substrates and thought to be due to lattice mismatch [Hu et al., 2001]. Such APBs were also observed in magnetite films deposited on MgO substrates [Margulies et al., 1996]. It was reported by Suzuki et al. that the APBs vanish when the $CoFe_2O_4$ films were deposited on $CoCr_2O_4$ buffered oxide substrates. However the buffered substrates induce a slight compressive strain in the film [Suzuki et al., 1999].

Post-deposition annealing treatments can play a major role in the properties of ferrite thin films. For example, in magnetite Fe_3O_4 film, Fe^{2+} ions can be oxidised to Fe^{3+} ions resulting in either α- or γ-Fe_2O_3 phase. Since γ-Fe_2O_3 is ferrimagnetic with net magnetic moment less than magnetite and α-Fe_2O_3 is a canted antiferromagnet, the overall magnetisation of the thin film is reduced [Suzuki, 2001].

3.3 Growth and characterisation of cobalt ferrite films

Cobalt ferrite thin films were deposited from a $CoFe_2O_4$ target using a 248 nm wavelength KrF excimer laser at 210 mJ and 13 Hz repetition rate. The laser spot size was 9 mm x 1.5 mm. The target-to-substrate distance was maintained at 50 mm. Substrates were Si (100) wafers with 300 nm thermal SiO_2 on top. The chamber was pumped down to $1x10^{-7}$ Torr before depositions.

3.3.1 Influence of substrate temperature

In order to study the influence of substrate temperature on the properties of cobalt ferrite thin films, a series of films were deposited at five different substrate temperatures or deposition temperatures (T_{DEP}): 250 °C, 350 °C, 450 °C, 550 °C and 600 °C. All films were deposited in 22 mTorr of oxygen, and cooled to room temperature under the same oxygen pressure. The properties of cobalt ferrite thin films at different substrate temperatures are detailed below.

a. Crystallography

The crystal structure and orientation of cobalt ferrite thin films were investigated by θ-2θ X-ray diffraction (XRD) scans, the patterns of which are shown in Fig. 3.1. All films were found to be crystalline, even at lower substrate temperatures. They all appear single-phase with cubic spinel structure. The films that were deposited at lower temperatures are predominantly (111)-textured whereas at higher temperatures, they are (100)- and (311)-textured. The compositions of films were determined using energy-dispersive X-ray spectroscopy (EDX) and were found to be $Co_{1.1}Fe_{1.9}O_4$. The oxygen content was assumed to have the stoichiometric value since EDX cannot determine the content of oxygen accurately.

The growth of crystalline cobalt ferrite films at low temperatures (~250 °C) indicates the potential for integration with multilayer structures that require low processing temperatures.

b. Deposition rate

The thicknesses of thin films were measured from cross-sectional imaging in

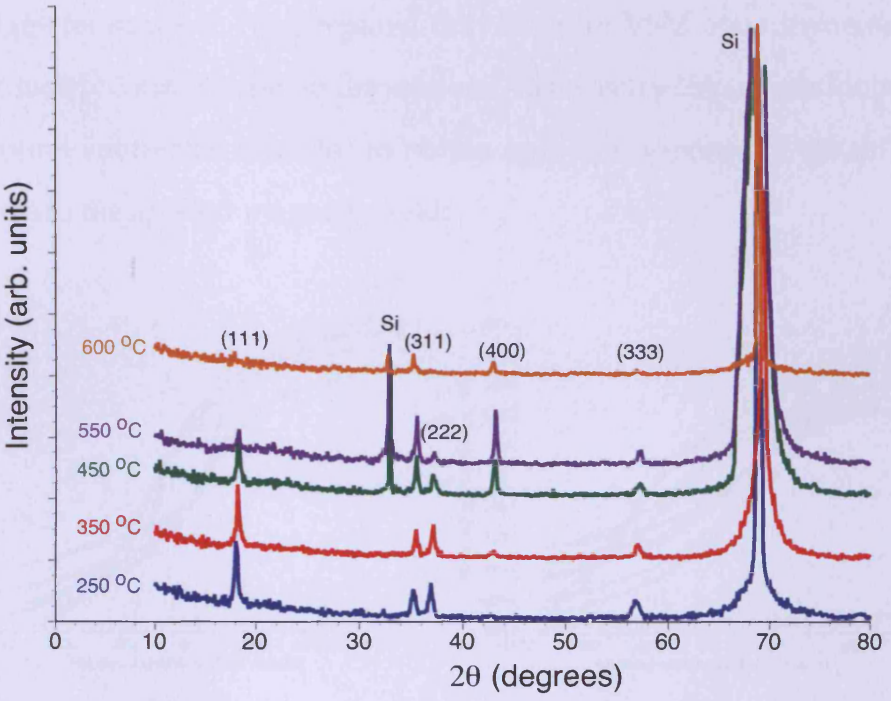

Figure 3.1: XRD powder diffraction patterns of cobalt ferrite thin films deposited at different substrate temperatures.

the SEM. All films were deposited for one hour and were 135±5 nm thick. The deposition rate was calculated to be 2.25±0.08 nm/min, which was found to be independent of substrate temperature.

c. Magnetic properties at room temperature

The magnetic hysteresis loops of cobalt ferrite thin films were measured at room temperature using a vibrating sample magnetometer (VSM). The VSM was calibrated using a thin film Nickel sample of dimension 5 mm x 5 mm. The response of a silicon substrate of the same size as the calibration sample was measured and used as background. In order to measure hysteresis loops in the VSM, cobalt ferrite thin films were prepared by scribing and breaking

a 2" diameter sample. The prepared thin films for VSM measurements were approximately 5 mm x 5 mm in dimension. All measured hysteresis loops were background subtracted in order to obtain only the response of cobalt ferrite thin films to the applied magnetic field.

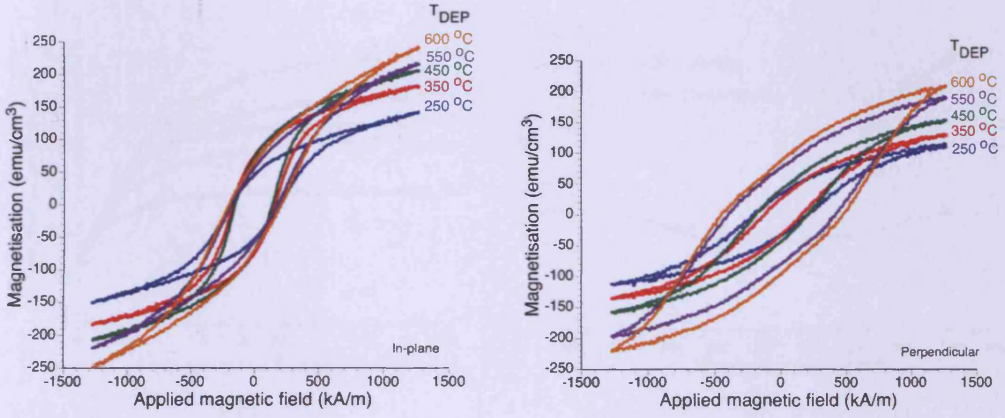

Figure 3.2: (a) In-plane hysteresis curves of cobalt ferrite thin films measured from VSM at room temperature. The magnetisation increases with increasing substrate temperature whereas the in-plane coercivity is almost same for all thin films. (b) The perpendicular hysteresis loops of thin films show the same trend in magnetisation as in-plane measurements.

A set of hysteresis loops for each cobalt ferrite thin film sample was measured by keeping the surface of thin films parallel (in-plane) and perpendicular to the applied magnetic field. All films were found to be isotropic in the plane and have high perpendicular anisotropy. Figures 3.2(a) and 3.2(b) show respectively the in-plane and perpendicular hysteresis loops measured at room temperature of cobalt ferrite thin films deposited at different substrate temperatures. The films did not seem to saturate at ~1200 kA/m (15 kOe). Figure 3.3(a) shows the initial magnetisation curves of the thin film samples measured from the SQUID magnetometer up to an applied magnetic field of ~4000

kA/m (50 kOe). Room temperature saturation magnetisation increased with substrate temperature. The variation of the magnetisation with substrate temperature can be explained based on the grain size effects and varying amounts of oxygen vacancies and cation site occupancies in the films.

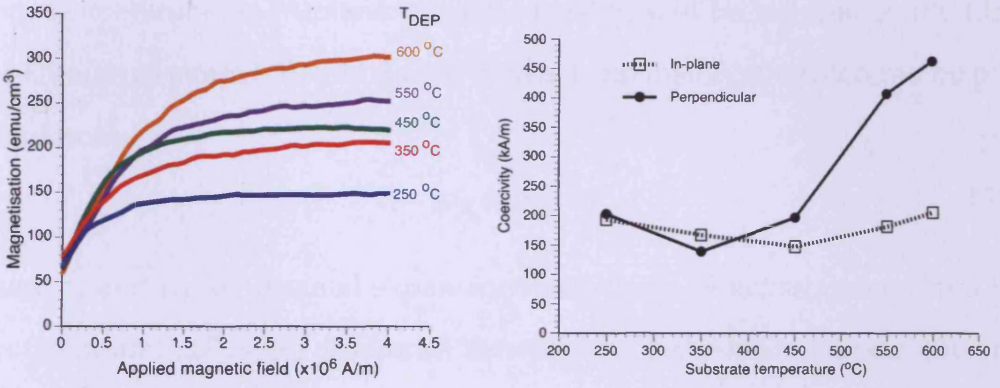

(a) (b)

Figure 3.3: (a) Initial magnetisation curves measured from SQUID. (b) The dependence of coercivity of cobalt ferrite thin films on the deposition temperature.

Large perpendicular anisotropy was observed in films deposited at higher substrate temperatures (600 °C and 550 °C). For decreasing substrate temperature, the hysteresis loops show reduction in the perpendicular anisotropy contribution. However, although the effect of perpendicular anisotropy contribution is less significant at lower temperatures, it is still high enough to produce substantial out-of-plane magnetisation, and contribute to the high coercivity of the films.

It is evident from Fig. 3.3(b) that in-plane coercivity is almost constant with temperature whereas the coercivity measured from perpendicular loops increases with temperature indicating also that the perpendicular magnetic anisotropy increases with substrate temperature.

Origin of perpendicular magnetic anisotropy

The thermal expansion coefficients of silicon substrate and cobalt ferrite are reported to be 3.5x10^{-6} K^{-1} and 10x10^{-6} K^{-1} respectively [Zhou et al., 2007]. Due to the mismatch, when the substrate-film combination is cooled down to room temperature, an in-plane isotropic tension will be induced in the film. The amount of strain induced due to thermal expansion mismatch can be predicted from

$$\epsilon = (\alpha_s - \alpha_f)\,\Delta T \tag{3.1}$$

where α_s and α_f are thermal expansion coefficients of substrate and film respectively, and ΔT is the difference between the deposition temperature and measuring temperature (usually room temperature).

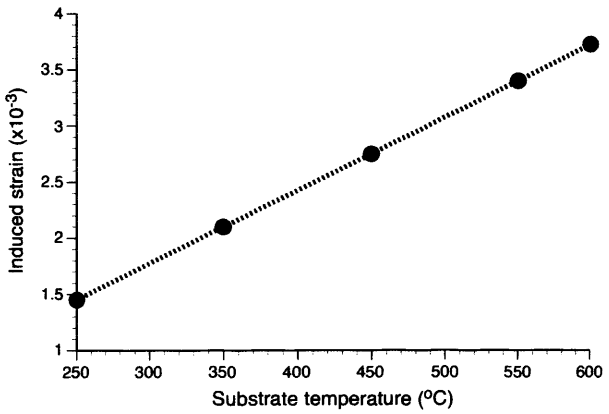

Figure 3.4: The calculated strain due to thermal expansion mismatch between the substrate and film at different substrate temperatures.

Figure 3.4 shows the predicted induced strain due to thermal expansion mismatch versus substrate temperature. As the substrate temperature increases, strain induced on the film becomes larger showing a linear relationship. Since cobalt ferrite has predominantly negative magnetostriction, in-plane tension

is expected to give rise to perpendicular magnetic anisotropy, which increases with increasing substrate temperatures.

Crystallographic texture together with magnetocrystalline anisotropy can also contribute to perpendicular anisotropy. To the extent that the high substrate temperature films show some preferred (100)-texture, that would be expected to contribute some in-plane anisotropy (since K_1 is reported to be positive for cobalt ferrite) and to the extent that the lower substrate temperature films show some preferred (111)-texture that would be expected to contribute some perpendicular anisotropy. However for the films of this study, it is apparent that the magnetoelastic contribution predominates, since the perpendicular anisotropy shows the reverse trend (highest for highest substrate temperature and lowest for lowest substrate temperature) [Zou et al., 2002].

d. Surface morphology

Figure 3.5 shows the surface morphology of cobalt ferrite thin films deposited at different substrate temperatures seen in atomic force microscopy (AFM). The RMS surface roughness was found to be around 3 nm for all samples. The grain size increases with increasing substrate temperature as shown in Fig. 3.6 from about 25 nm for T_{DEP}=250 °C, to about 100 nm for T_{DEP}=600 °C.

e. Domain imaging

Irregular domain patterns with global non-equilibrium character observed in these films are commonly observed in materials with strong perpendicular anisotropy and high domain wall coercivity. The as-deposited films were subjected to a magnetic field of ~400 Oe in the MFM in order to investigate magnetic domain patterns. Though the magnetic domains are in a global non-

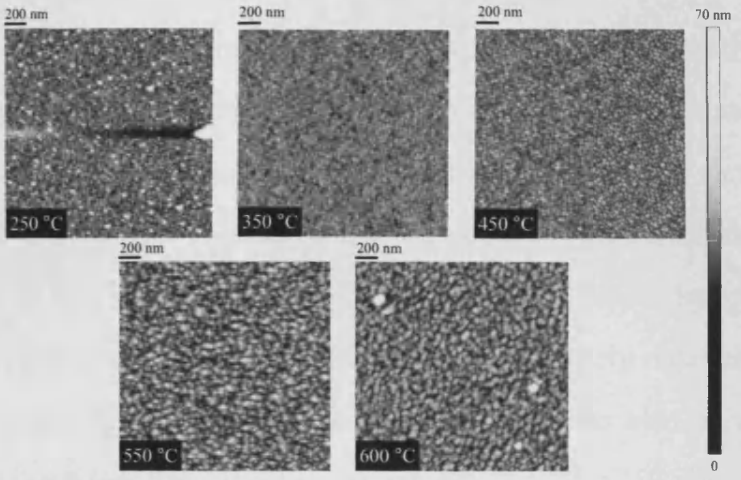

Figure 3.5: The surface morphology of cobalt ferrite thin films seen in AFM.

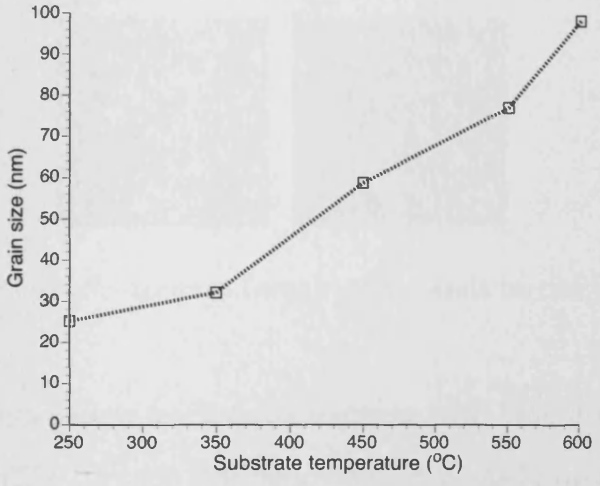

Figure 3.6: The grain size of cobalt ferrite films versus substrate temperature.

equilibrium condition, they nonetheless reflect a typical feature size similar to the equilibrium period of maze-type domains [Hubert & Schafer, 1998].

As shown in Fig. 3.7, the magnetic feature size increases with increasing deposition temperature. According to a simple stripe domain model, for materials with easy axis perpendicular to the crystal surface, the domain width (or magnetic feature size) increases with increasing perpendicular anisotropy constant K_u (as $K_u^{\frac{1}{4}}$) [Chikazumi, 1997]. Hence the observed increase in magnetic domain size is consistent with the magnetic property measurements discussed previously, where perpendicular anisotropy was also observed to increase with increasing deposition temperature.

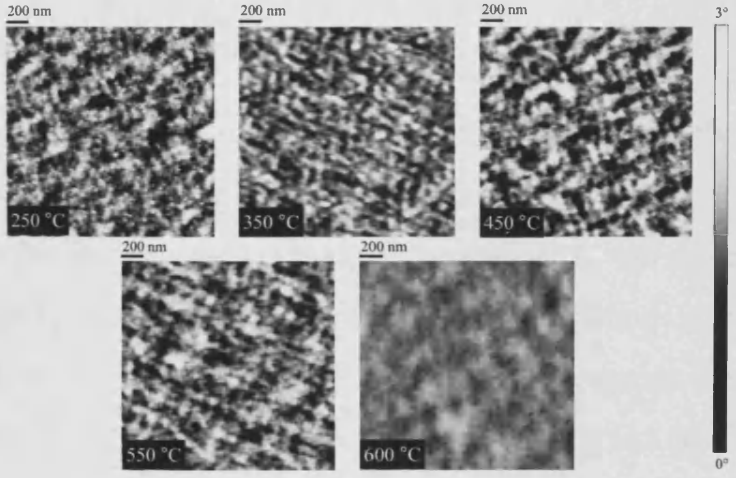

Figure 3.7: The magnetic domain imaging of cobalt ferrite thin films seen in MFM.

Grain size and magnetic feature size increase with T_{DEP} at different rates. In films deposited at 250 °C each magnetic domain is made up of approximately 100 grains whereas for films deposited at 600 °C, each magnetic domain is made up of about 25 grains.

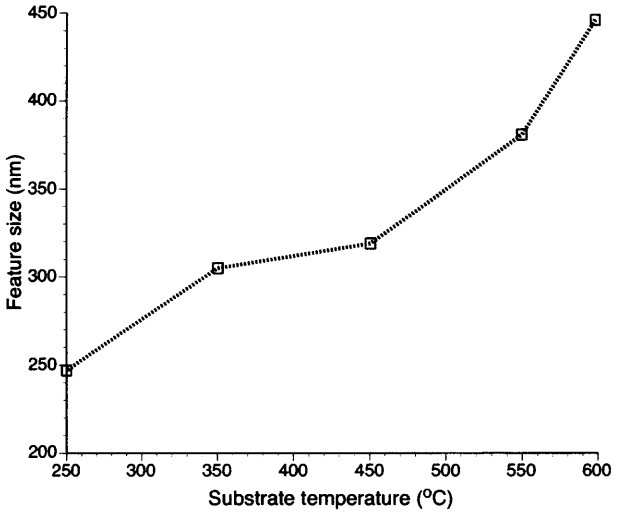

Figure 3.8: The magnetic feature size of cobalt ferrite films versus substrate temperature.

3.3.2 Influence of reactive oxygen

In order to study the effects of reactive oxygen atmosphere on the growth and properties of cobalt ferrite, a series of thin films were grown on SiO_2/Si(100) substrates at the lowest substrate temperature of 250 °C and oxygen pressures from 5 mTorr to 50 mTorr. Five different oxygen pressures were chosen for the study: 5, 15, 22, 35 and 50 mTorr. The laser parameters were the same as given in Section 3.3. The chamber was pumped down to $1x10^{-7}$ Torr before depositions.

a. Crystallography

The XRD θ-2θ scans of cobalt ferrite thin films deposited at various oxygen pressures are shown in Fig. 3.9. The films deposited at 22 mTorr and 35 mTorr appear single phase with cubic spinel structure whereas the films grown at oxygen pressures lower than 22 mTorr (5 mTorr and 15 mTorr) are mixed-

phase. This is probably due to the formation of cobalt-rich (Co,Fe)O and iron-rich Fe_2O_3 phases in the film. A similar observation of secondary phase was made on bulk cobalt ferrite material when vacuum-annealed [Nlebedim et al., 2009].

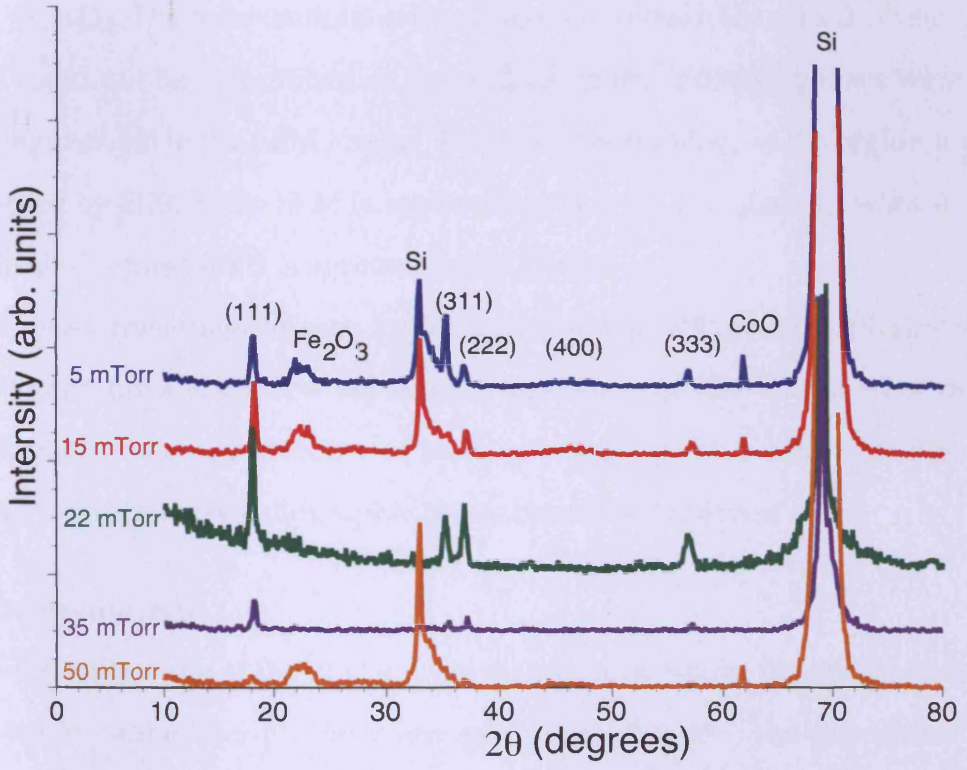

Figure 3.9: XRD powder diffraction patterns of cobalt ferrite thin films deposited at different oxygen pressures.

It has been known that at higher oxygen pressures, the ablated species can reactively collide with ambient oxygen forming clusters [Chen et al., 1997]. Hence deposition of thin films at high oxygen pressures and low substrate temperatures (in this case, 250 °C) can result in iron oxide and cobalt oxide clusters causing iron oxide and cobalt oxide regions in the film, with insufficient ionic mobility to uniformly intermix them. Thus the sample deposited at

high oxygen pressure also shows several structural phases, although the cation compositions of the phases could be considerably different than what forms at low oxygen pressures.

From EDX, the average composition of all thin films was found to be $Co_{1.1}Fe_{1.9}O_4$. The compositions of the different phases in the mixed-phase samples could not be determined as the regions of the different phases were not distinguishable in the SEM image. This is not surprising, as the region that is sampled by EDX in the SEM is approximately 1 μm dimensions, whereas the grain size in these films is approximately 25 nm.

This analysis suggests that, for the optimised growth of single phase cobalt ferrite thin films at the low substrate temperature of 250 °C and these deposition rates, there is a window of reactive oxygen pressure above and below which the correct crystallographic phase cannot be achieved.

b. Deposition rate

The deposition rate of the PLD system mainly depends on the orientation and directivity of the laser plume at any given laser fluence. The deposition rate was calculated as

$$\mathrm{d} = \frac{\text{thickness}}{\text{duration}} \tag{3.2}$$

The duration of deposition for all thin films was 1 hour.

Figure 3.10 shows that the deposition rate decreases rapidly after ~22 mTorr. This observation is consistent with the study by Gorbunov and Konov who showed that the laser plume broadens due to collisions between ejected species and ambient oxygen at oxygen pressures above 22 mTorr [Gorbunov & Konov, 1991]. These collisions also reduce the mean free path of the ejected species and

hence enable particulate formation even before they reach the substrate.

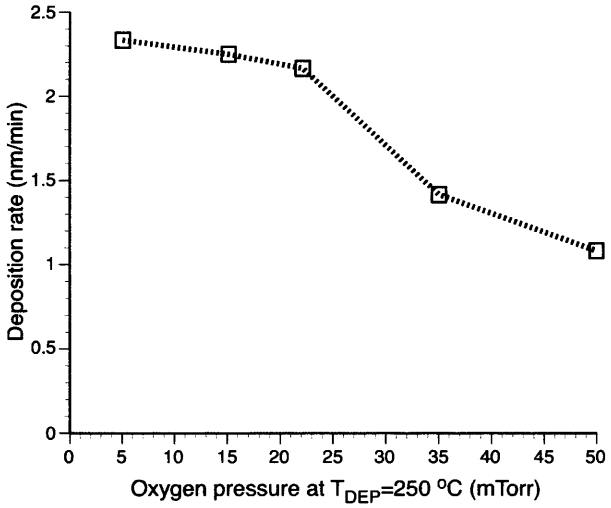

Figure 3.10: Variation of deposition rate with reactive oxygen pressures.

c. Magnetic properties at room temperature

The in-plane and perpendicular hysteresis loops of cobalt ferrite thin films deposited at different oxygen pressures were measured in the VSM and are shown in Figs 3.11(a) and 3.11(b) respectively. The magnetic properties show a high perpendicular anisotropy due to thermal expansion mismatch between the film and the substrate as explained in Section 3.3.1(c).

The initial curves measured from SQUID magnetometer indicate that the mixed-phase films show higher saturation magnetisation than single phase films. This may be attributed to the cation site occupancies in the films. Although neither CoO, FeO nor α-Fe_2O_3 themselves are expected to contribute significant moment at room temperature, to the extent that Co-rich (Co,Fe)O forms, it leaves behind Fe-rich material and Fe-rich spinel phase will have a higher moment than $CoFe_2O_4$ due to the fact that Fe^{3+} ions have moments of

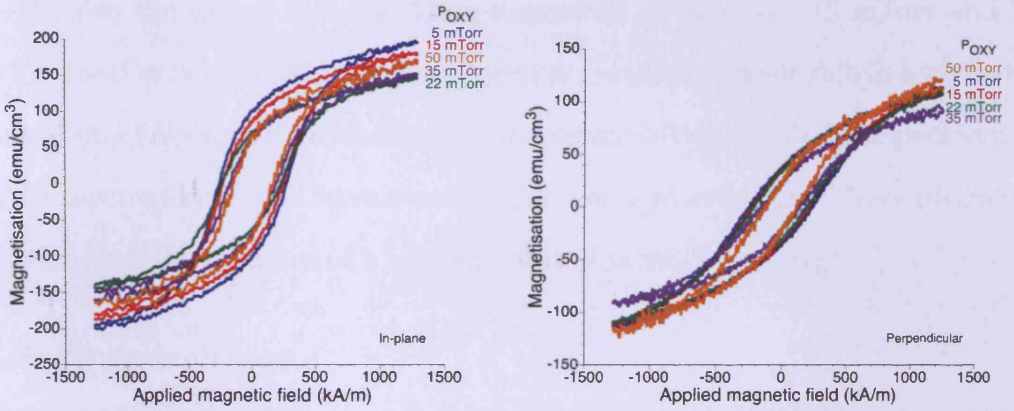

(a) (b)

Figure 3.11: (a) In-plane and (b) perpendicular hysteresis curves of cobalt ferrite thin films deposited at different oxygen pressures measured from VSM at room temperature.

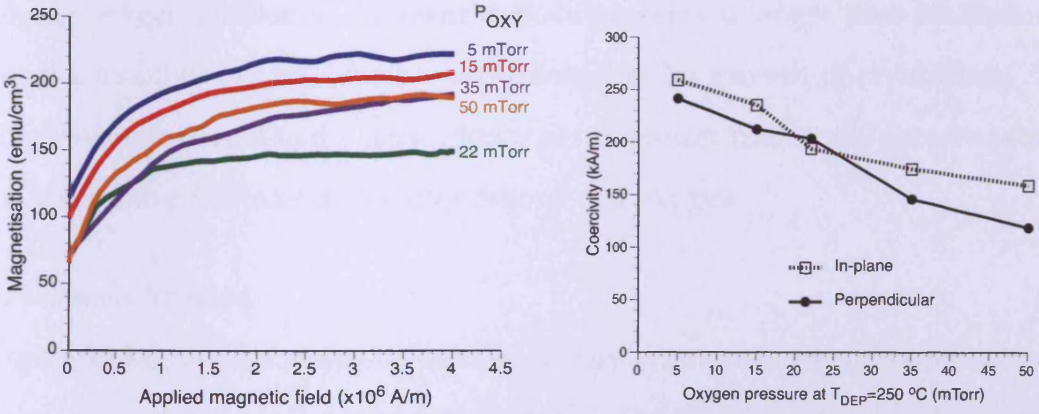

(a) (b)

Figure 3.12: (a) Initial magnetisation curves measured from SQUID magnetometer. (b) The dependence of coercivity of cobalt ferrite thin films on the reactive oxygen pressure.

$\sim 5\mu_B$ whereas Co^{2+} have moments of $\sim 3\mu_B$.

Also to the extent that the films deposited at very low (5 mTorr and 15 mTorr) and very high (50 mTorr) oxygen pressures are cobalt-rich in their tetrahedral sites (A-sites), then an increase in magnetisation would be expected due to the fact that Fe^{3+} ions have moments of $\sim 5\mu_B$ whereas Co^{2+} have moments of $\sim 3\mu_B$ and the moment of a formula unit of spinel is m_B-m_A.

d. Surface morphology

Figure 3.13 shows surface morphology of cobalt ferrite thin films deposited at different reactive oxygen pressures as seen in AFM. The RMS surface roughness was found to be around 3 nm for all samples. The grain size increases with increasing oxygen pressure as shown in Fig. 3.14 from about 6 nm for P_{oxy}=5 mTorr, to about 115 nm for P_{oxy}=50 mTorr. The grain size increases drastically after P_{oxy}=22 mTorr. This could be related to the decrease in deposition rate at higher oxygen pressures. At lower deposition rates, a longer time is allowed for the mobility of ions which would enhance the growth of crystallites. It might also be related to the dependence of nucleation and crystal growth rates on the relative fluxes of depositing cations and oxygen.

e. Domain imaging

Figure 3.15 shows the magnetic domain images of cobalt ferrite films deposited at various oxygen pressures as seen in MFM. The magnetic domains look like clusters. The cluster-like magnetic domains are commonly found in high perpendicular anisotropy materials with large coercivity [Hubert & Schafer, 1998].

It can be noted from the above analysis that for the optimised growth of single phase cobalt ferrite thin films at low substrate temperatures (say 250 °C

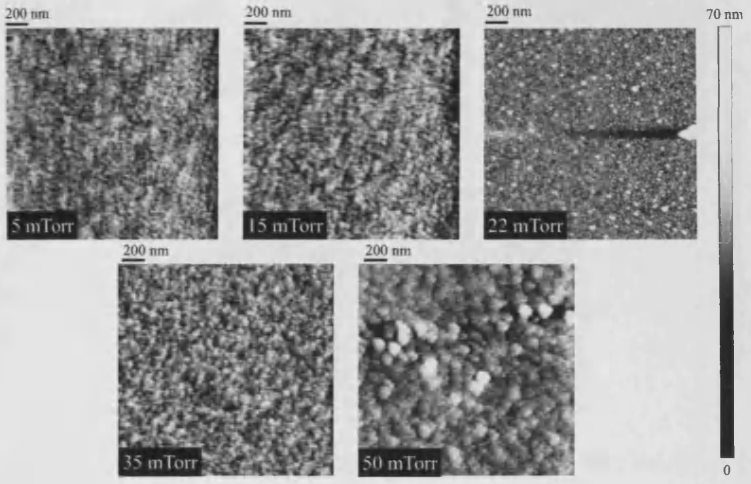

Figure 3.13: The surface morphology of cobalt ferrite thin films seen in AFM for different reactive oxygen pressures.

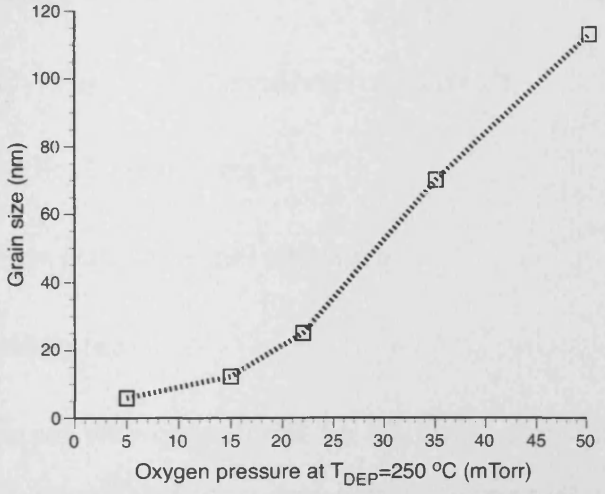

Figure 3.14: The grain size of cobalt ferrite films versus reactive oxygen pressure.

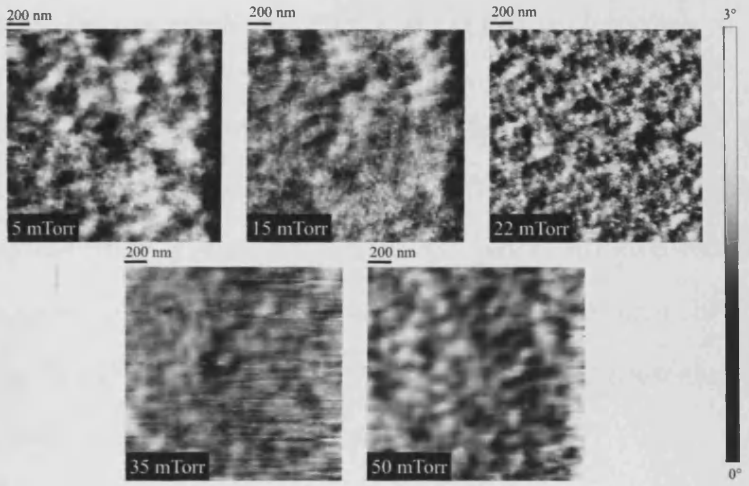

Figure 3.15: The magnetic domain images of cobalt ferrite thin films seen in MFM for different reactive oxygen pressures.

the reactive oxygen pressure should be chosen in the range of 20 mTorr to 40 mTorr. The optimised cobalt ferrite thin film sample grown for this study is the one grown at a substrate temperature of 250 °C and oxygen pressure of 22 mTorr. The reasons for this are

- comparatively less thermal expansion mismatch,
- lower perpendicular anisotropy,
- single phase crystalline spinel structure,
- better deposition rate.

Hence this sample was considered for magnetic annealing to induce in-plane uniaxial anisotropy and for measurement of magnetostriction using inverse technique.

3.4 Effect of magnetic annealing

Magnetic annealing is a process by which a uniaxial anisotropy is induced in a magnetic sample by heat-treatment in the presence of a magnetic field. In cobalt ferrite, this effect is thought to be due to short-range directional order of the cations around the Co^{2+} in octahedral sites [Chikazumi, 1997]. This phenomenon was found to improve the magnetic and magnetoelastic properties of the material [Bozorth et al., 1955; Lo et al., 2005].

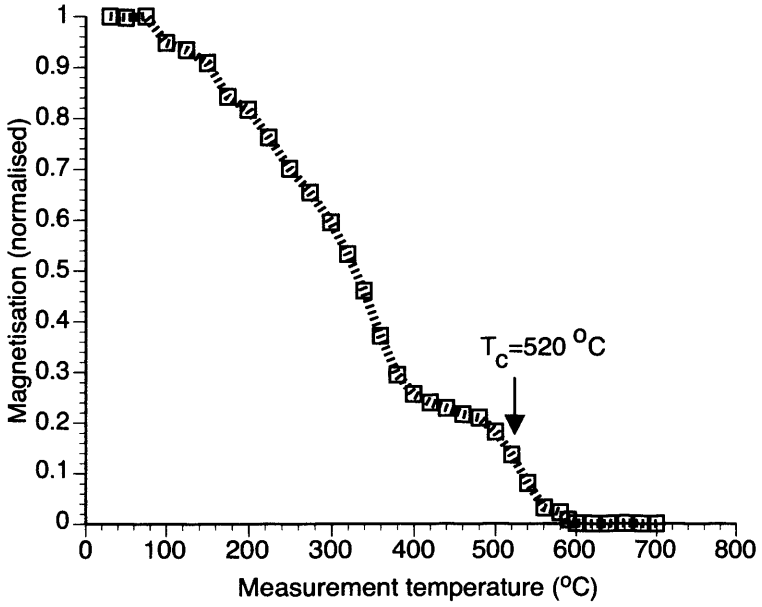

Figure 3.16: The magnetisation versus temperature of cobalt ferrite thin film (at 1600 kA/m (mu_0H=2 T) applied field) deposited at 250 °C and 22 mTorr oxygen. The Curie temperature was found to be at 520 °C using the point of inflection procedure.

In order to magnetically anneal a sample, it is necessary to know the Curie temperature of the material. The Curie temperature is the temperature above which the magnetic material becomes paramagnetic. The heat treatment during the magnetic annealing should be carried out at temperatures below the

Curie temperature so as to achieve required magnetic ordering. The Curie temperature of a magnetic specimen can be obtained by measuring magnetisation at different temperatures as shown in Fig. 3.16. The magnetisation of the thin film was measured in the presence of a magnetic field of ~1600 kA/m (20 kOe) at temperatures ranging between 30 and 700 °C.

The measured magnetisation versus temperature curve shows the unusual feature of a dip at about 400 °C. This could be due to

- compensation point-type behaviour or
- phase separation into Co-rich and Fe-rich spinel phases.

In general the sublattice magnetisations were assumed to decrease monotonically with increasing temperature. However if the moment in A-sublattice decreases less rapidly than that of B-sublattice, a compensation point-type behaviour is expected [Smit & Wijn, 1959]. Although it is possible to observe compensation point-type behaviour in spinel ferrites, it appears to be very rare. The compensation point-type behaviour is only known to occur in spinel ferrites with a large amount of cation substitution (especially non-magnetic cation substitution) onto the octahedral sites. However, it does not appear in any known reports of M vs. T for cobalt ferrite.

The phase separation into Co-rich and Fe-rich spinel phases has been reported [Muthuselvam & Bhowmik, 2009]. Although XRD scan appears to show single phase spinel crystal structure, it is doubtful whether it would resolve small peak splitting in nanograined films with relatively small signal and broad peaks. Furthermore, since the films are grown at low temperature where there is low ionic mobility, there could be some distribution of composition.

Fe_3O_4 is reported to have a Curie temperature of 585 °C, which is quite close to the upper Curie temperature of the film [Smit & Wijn, 1959]. Bulk $CoFe_2O_4$ is reported to have a Curie temperature of 520 °C [Smit & Wijn, 1959]. Single phase spinel Co_2FeO_4 is reported to have a Curie temperature of about 180 °C and the compositions between latter two are reported to have Curie temperatures in-between [Muthuselvam & Bhowmik, 2009].

The magnetic annealing of cobalt ferrite thin film (deposited at a substrate temperature of 250 °C and oxygen pressure of 22 mTorr) was carried out using the VSM. The sample was heat-treated in the VSM furnace at 450 °C for 48 hours in argon atmosphere in the presence of a in-plane magnetic field of ~2000 kA/m (25 kOe). After the heat treatment, the furnace and magnetic field were turned off and the sample was allowed to cool in the argon atmosphere.

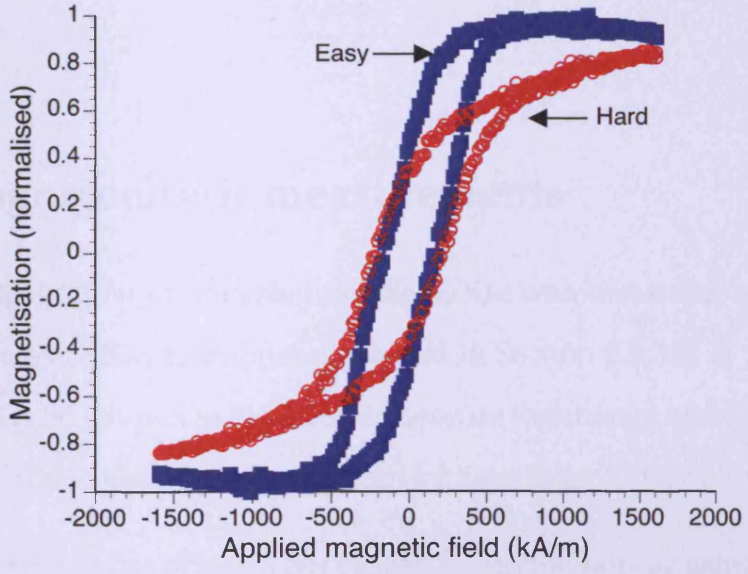

Figure 3.17: Induced uniaxial anisotropy in cobalt ferrite thin films by magnetic annealing at 450 °C. Hysteresis loops measured at room temperature in the plane along (easy) and orthogonal (hard) to the direction of applied field during magnetic anneal.

The magnetisation of this annealed sample was then measured by VSM with the sample held at 0° (easy axis) and 90° (hard axis) in-plane to the direction of applied field. The measured hysteresis loops are shown in Fig 3.17. It is evident from the loops that the magnetic annealing induced an change in the magnetic anisotropy of cobalt ferrite thin film sample with the easy axis being along the direction of the annealing field. Table 3.1 lists the values of coercivities before and after magnetic annealing.

Table 3.1: Effect of magnetic annealing on coercivity

Annealing		Coercivity (kOe)
Before		2.42
After		
	Easy	2.15
	Hard	2.64

3.5 Magnetoelastic measurements

The magnetostriction of annealed cobalt ferrite was measured using the inverse magnetostriction technique explained in Section 2.5.3.5. A 3-point bender was designed (shown in Fig 3.18) to measure the change in anisotropy field in the VSM. The strain on the sample can be determined by two ways.

- A known amount of stress can be applied on the sample using the bender assembly by means of a calibrated screw.
- Alternatively, the strain on the film can be measured using a strain gauge.

In this study, the latter method was used. A compressive stress was applied on the sample by turning the screw clockwise in the bender and the induced compressive strain was measured using a strain gauge as shown in Fig 3.18.

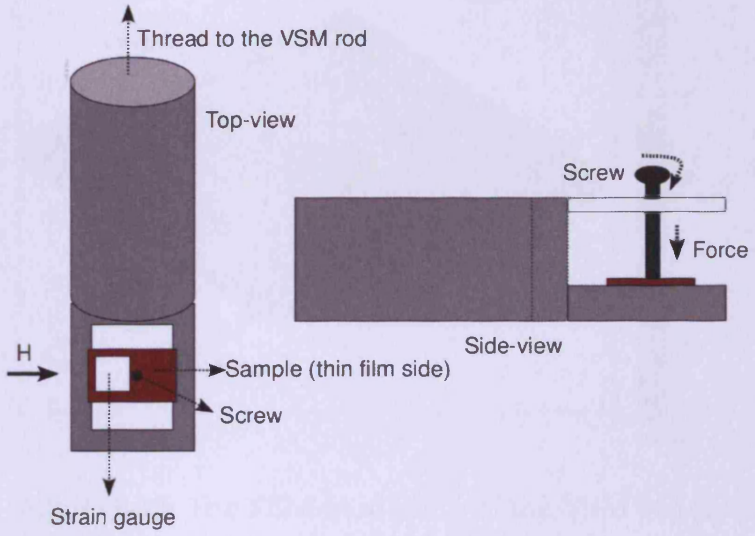

Figure 3.18: The schematic of a bender assembly designed for VSM to apply known amount of stress on thin film samples. The strain gauge was on the film-side and the screw was in contact with the film while applying compressive stress.

The VSM bender was modelled and analysed using finite element modelling in COMSOL multiphysics software (see Fig. 3.19). The main objective of this model is to determine the average strain on the film. During the measurement, strain was averaged over the active area of strain gauge (2 mm x 2 mm). Hence the average strain value measured from strain gauge will be larger than the average strain on the sample. In COMSOL, strain was averaged over the entire sample (approximately 6 mm x 6 mm). It was found that the strain measured using strain gauge (3.5×10^{-5}) overstates the average strain on the sample ($\sim 2.19 \times 10^{-5}$) by 60%.

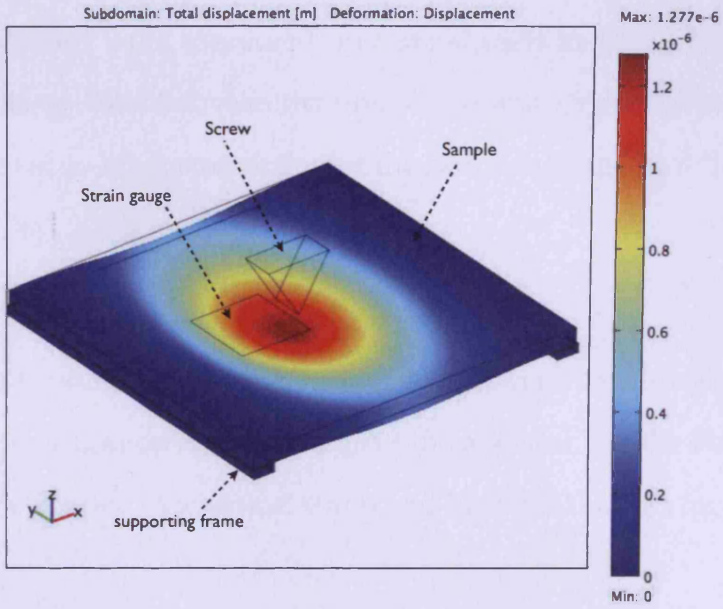

Figure 3.19: The FEM modelling of the VSM bender.

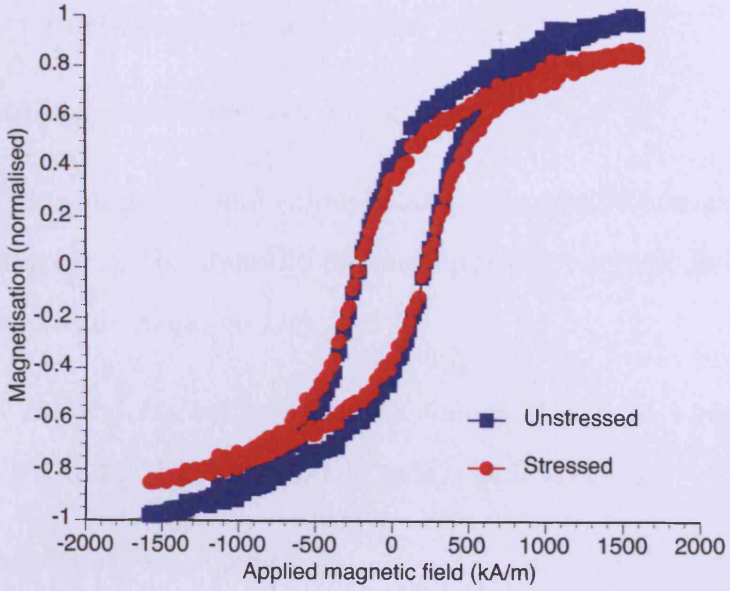

Figure 3.20: Influence of compressive stress on cobalt ferrite thin films.

The hard axis hysteresis loops of the cobalt ferrite film at unstressed and stressed conditions were measured and are shown in Fig. 3.20. The difference in anisotropy field between the unstressed and stressed hysteresis loops was then related to magnetostriction of the sample using the following equation [O'Handley, 2000]

$$\lambda_s = \frac{\Delta H_k}{\epsilon} \frac{M_s(1-v^2)}{3Y_f} \tag{3.3}$$

where ΔH_k is the difference in anisotropy field between zero-stress and stressed state, M_s is the saturation magnetisation of the material, v is the Poisson's ratio of film, ϵ is the applied mechanical strain and Y_f is the Young's modulus of the film.

The anisotropy field can be obtained from the measured curves in a similar way as the one used in commercial BH looper system [Choe & Megdal, 1999]. The procedure that was used to calculate anisotropy field from the measured hysteresis loop can be explained as follows:

1. Measure hysteresis (MH) loop of the sample.

2. Identify the magnetic field values at 50% of saturation or maximum magnetisation (M_S). There should be four values of magnetic field (two each for positive and negative M_S).

3. Assign H_A and H_B to the two field values at 50% of $+M_S$. Similarly, assign H_C and H_D to the two field values at 50% of -M_S.

4. Find the average of H_A and H_B.

5. Find the average of H_C and H_D.

6. Find the difference between the two averages. The resulting value is the anisotropy field of the sample.

The above procedure was carried out on both unstressed and stressed samples. The difference in the anisotropy field between unstressed and stressed sample was found to be 144.7 Oe. The saturation magnetisation, M_s, was measured using SQUID magnetometer (shown in Fig. 3.3(a)) as 150 emu/cm^3 (150 kA/m). The Poisson ratio, v, was assumed to be 0.3 and the Young's modulus, Y_f, of Cobalt ferrite is 141.6 GPa [Zheng et al., 2004]. The applied mechanical strain, ϵ, was calculated from finite element modelling and was 2.19x10^{-5}. Substituting these values in the equation (3.3) gives

$$\lambda_s \approx -211.3 \times 10^{-6} \tag{3.4}$$

The saturation magnetostriction of polycrystalline cobalt ferrite in bulk form was reported as -210 x 10^{-6} [Bozorth, 1951]. However, bulk cobalt ferrite has also been reported in the literature to have values ranging from -65 x 10^{-6} to -225 x 10^{-6} depending on sample fabrication and processing conditions [Nlebedim et al., 2010]. The deposited thin film falls close to the upper end of this range.

It is interesting to note that despite the facts that the thin film has very different M_s and coercivity than bulk cobalt ferrite, it nonetheless has a measured magnetostriction comparable to some of the highest values measured for bulk material.

3.6 Summary

- The growth of magnetoelastic thin films using pulsed-laser deposition technique was detailed. The influence of substrate temperature and oxygen pressure on the magnetic properties and crystal structure of cobalt ferrite thin films was studied.

- The growth process of cobalt ferrite thin films was optimised for low substrate temperature. It was found that there is only a narrow window of reactive oxygen pressure for the growth of single phase spinel crystalline cobalt ferrite thin films at low substrate temperatures.

- Cobalt ferrite films grown at low substrate temperature and optimised oxygen pressure on thermal expansion matched substrates, can be applied in multilayer sensors on micro electro mechanical systems (MEMS) devices.

- The optimised cobalt ferrite thin film was magnetically annealed to successfully induce in-plane uniaxial anisotropy.

- Saturation magnetostriction was measured on the magnetically annealed cobalt ferrite thin film based on inverse measurement technique in the VSM. A 3-point bender was designed for this purpose.

- Despite the fact that the cobalt ferrite thin film differs from bulk material in a number of ways, nonetheless the measured magnetostriction value coincides with the upper end of the range of values reported for bulk material.

Chapter 4

Magnetocaloric thin films

4.1 Introduction

This chapter describes the growth and characterisation of magnetocaloric thin films. The films are deposited from a $Gd_5Si_2Ge_2$ target on AlN substrates using pulsed-laser depostion (PLD). Section 4.2 discusses the only reported previous work in the literature on growing $Gd_5Si_2Ge_2$ thin films. Section 4.3 explains the growth conditions for the deposition of thin films. Section 4.4 determines the best deposition temperature to grow $Gd_5Si_2Ge_2$ thin films of desired phase and composition. Section 4.5 describes several characterisation techniques used. The measurements on crystallographic structure, composition and scanning electron microscopy are detailed. The observation of magnetic phase transformation from the measured magnetisation at different temperatures is also discussed.

4.2 Magnetocaloric thin films

Magnetocaloric materials, in particular $Gd_5(Si_xGe_{1-x})_4$ alloys have been extensively studied in their bulk form [Pecharsky & Gschneidner Jr., 1997a,b,c]. Yet with the exception of one unsuccessful attempt, there are no thin films of these alloys reported in the literature until now. The reason for this could be their complexity in stabilisation of crystal and phase structures which are highly dependent on the purity of components and post-annealing processes [Mozharivskyj et al., 2005].

The only published article in the literature is on the growth of $Gd_5Si_2Ge_2$ on Si_3N_4/Si substrates [Sambandam et al., 2005]. The films were sputtered from a $Gd_5Si_2Ge_2$ target. The deposited films were vacuum annealed at three different temperatures: 700, 900 and 1150°C for 1 hr. It was found that the formation of $GdSi_2$ phase in the films was enhanced with increasing temperature. At 1150 °C, $Gd_5Si_2Ge_2$ formed along with the $GdSi_2$ phase. Sambandam et al. concluded that although the magnetocaloric phase formed, the Si_3N_4 was not a stable diffusion barrier. The secondary ion mass spectrometry (SIMS) analysis at the interface of film/Si_3N_4/Si indicated a breakdown of the diffusion barrier (Si_3N_4) and an evident inter-diffusion between the film and the substrate.

4.3 Growth of $Gd_5(Si_xGe_{1-x})_4$ thin films

In bulk form, $Gd_5(Si_xGe_{1-x})_4$ alloy composition, phase, crystal structure and the resulting magnetocaloric effect are determined by the heat treatments and purity of the components [Mozharivskyj et al., 2005; Pecharsky & Gschneid-

ner Jr., 1997c; Pereira et al., 2008]. It can be ascertained that, also in thin films, the growth conditions play a crucial role in achieving the correct phase and crystal structure in $Gd_5Si_2Ge_2$. Hence the growth conditions, in particular the deposition temperature should be carefully chosen.

As a part of this work, thin films of $Gd_5Si_2Ge_2$ were grown on polycrystalline AlN substrates from a commercial $Gd_5Si_2Ge_2$ target using PLD with a 248 nm wavelength KrF excimer laser. The laser was maintained at 210 mJ and 13 Hz repetition rate throughout the deposition. The target-to-substrate distance was maintained at 50 mm. The chamber was baked out for 36 hours at 450 °C in order to achieve suitable vacuum. The chamber was pumped down to $7x10^{-9}$ Torr before the deposition. The films were deposited in an argon atmosphere at a pressure 20 mTorr for 1 hour. After deposition, the films were cooled at a rate of 15 °C/min in vacuum.

4.4 Deposition temperature

The deposition temperature was determined from Fig. 4.1, which shows the fraction of orthorhombic phase versus heating and cooling in a $Gd_5Si_2Ge_2$ sample with predominantly monoclinic phase [Mozharivskyj et al., 2005]. These samples were prepared by arc-melting, followed by heat treatment for an hour at 1570 K. These samples were then heated to high temperatures (up to 600 °C) at a rate of 20 °C/min and the in situ XRD pattern at each temperature was measured to determine the monoclinic to orthorhombic transition in $Gd_5Si_2Ge_2$ samples.

It is evident from the graph (Fig. 4.1) that the orthorhombic phase de-

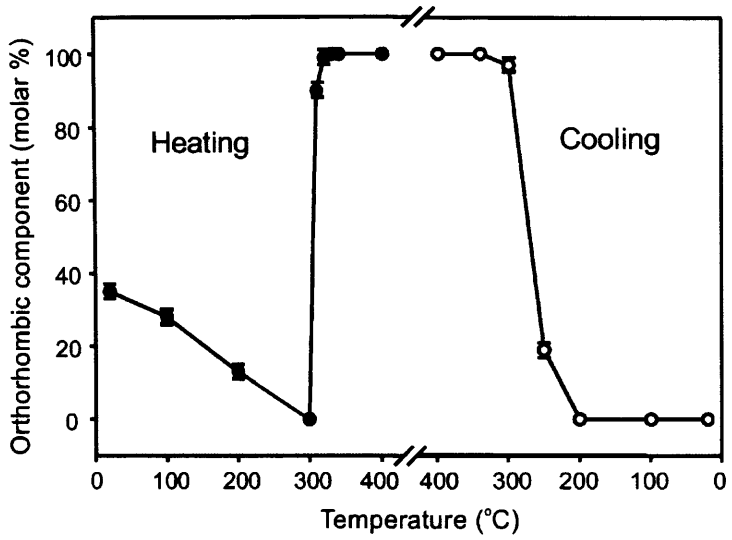

Figure 4.1: The amount of orthorhombic phase versus heating and cooling in $Gd_5Si_2Ge_2$. The 400 °C point during heating and cooling is the same experimental point [Mozharivskyj et al., 2005].

creases almost linearly with heating until 300 °C (from 38% at 20 °C to 0% at 300 °C). On further heating, the amount of orthorhombic component increases suddenly to 90% and at 320 °C, monoclinic phase disappears completely [Mozharivskyj et al., 2005].

Hence the temperature for the growth of $Gd_5Si_2Ge_2$ thin films on AlN substrates was set at 285 °C (very close to 300 °C) in order to achieve maximum monoclinic phase and very little orthorhombic phase in thin films.

4.5 Characterisation of $Gd_5(Si_xGe_{1-x})_4$ thin films

4.5.1 X-ray diffraction patterns

The θ-2θ XRD pattern of the thin film deposited on AlN substrate from a $Gd_5Si_2Ge_2$ target is shown in Fig. 4.2. The average composition of the film

was determined as $Gd_5Si_{2.08}Ge_{1.92}$ in the EDX. The measured θ-2θ XRD pattern was matched with the powder diffraction file (PDF) library pattern of monoclinic structure of bulk $Gd_5Si_2Ge_2$. It can be seen from matching the measured pattern with the library pattern, as shown in Fig. 4.2, that the film is predominantly monoclinic.

The XRD patterns of the secondary phases of Gd-Si-Ge were generated using FULLPROF software [Rodriguez-Carvajal, 1993] and are plotted with the measured pattern for comparison in Fig. 4.3. None of the secondary phase (5:3 and 1:1) peaks was found in the measured XRD pattern of thin film. Since orthorhombic and monoclinic phases possess similar crystal structure, it is not very easy to distinguish between their peaks. For a thorough analysis and understanding of the crystal structure of this thin film, a Rietveld refinement of the measured XRD pattern is required [Pereira et al., 2008].

4.5.2 Scanning electron microscopy

The SEM image of $Gd_5Si_{2.08}Ge_{1.92}$ is shown in Fig. 4.4. The average grain size was measured as $\sim$1.5 μm. The grain size indicates that the film is crystalline even when grown at a substrate temperature of 285 °C. As can be seen from the SEM image, the film appears to have a smooth surface with no or minimum amount liquid droplets found on the surface of the film, which is otherwise a commonly occurring problem in the growth of metallic thin films [Chrisey & Hubler, 1994].

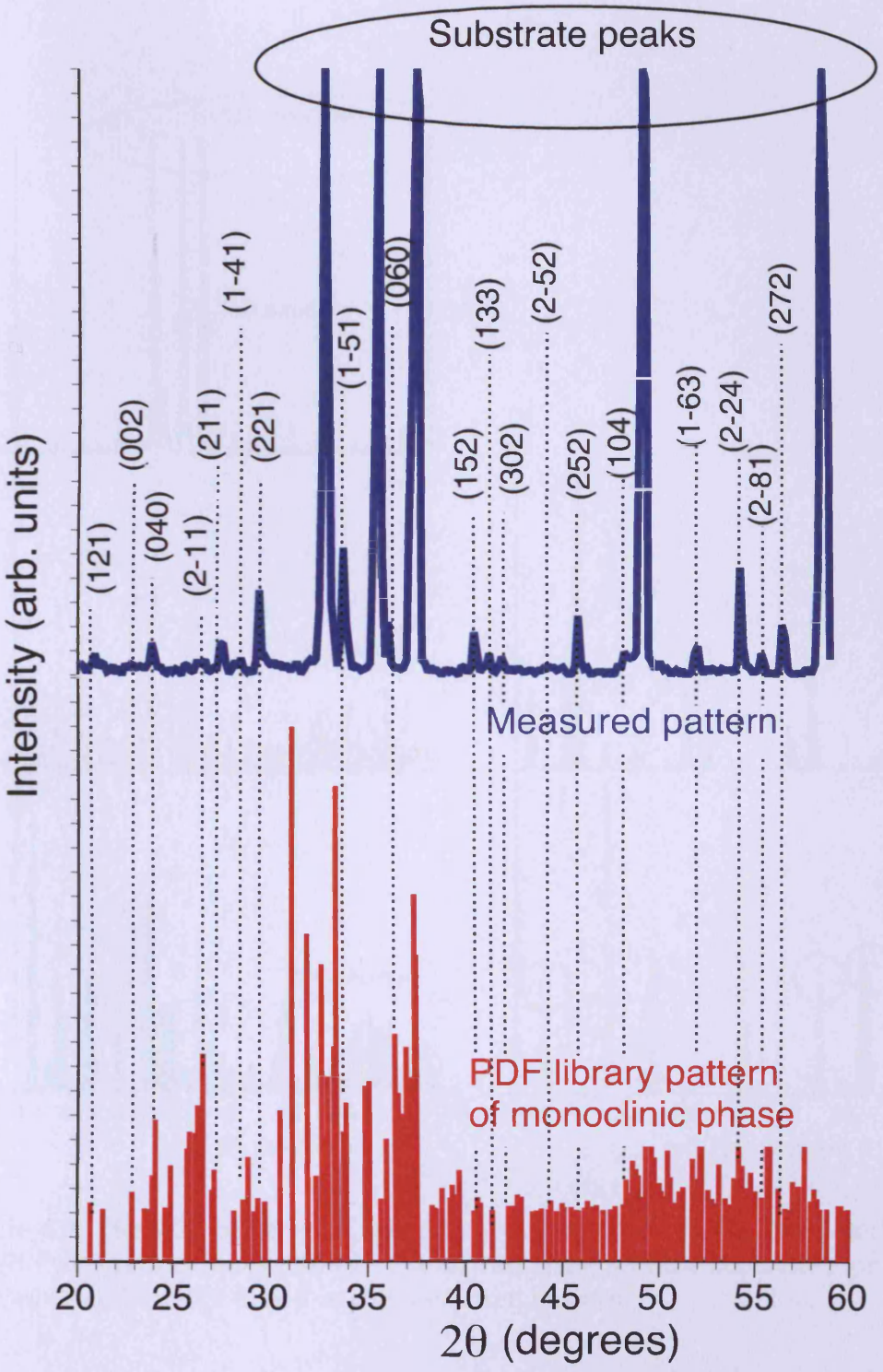

Figure 4.2: The θ-2θ XRD pattern of $Gd_5Si_{2.08}Ge_{1.92}$ thin film deposited at 285 °C on AlN substrate.

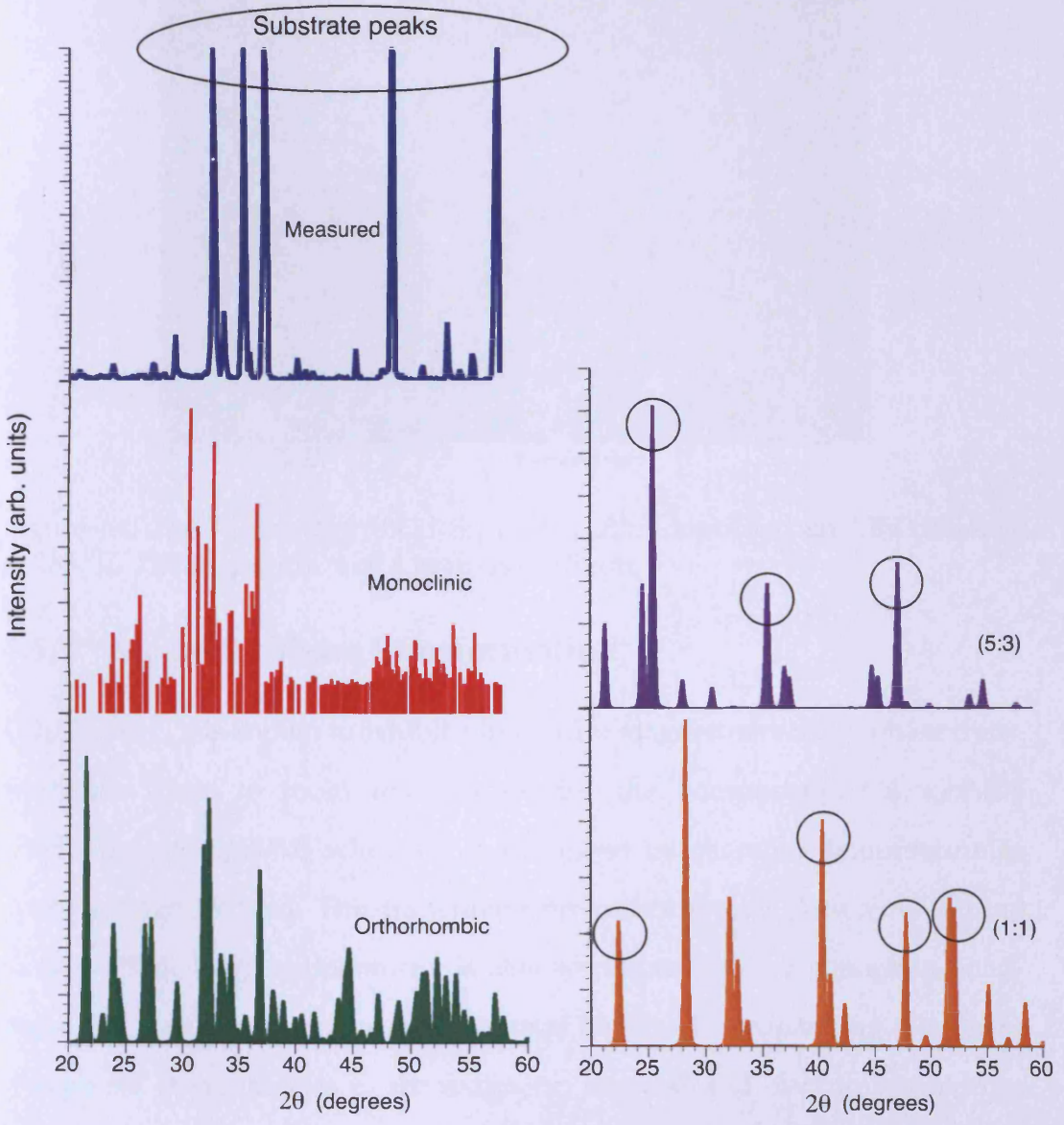

Figure 4.3: The θ-2θ patterns of secondary phases of Gd-Si-Ge calculated using Rietveld refinement method. The distinct peaks of the secondary phases (circled peaks) are not found in the measured pattern.

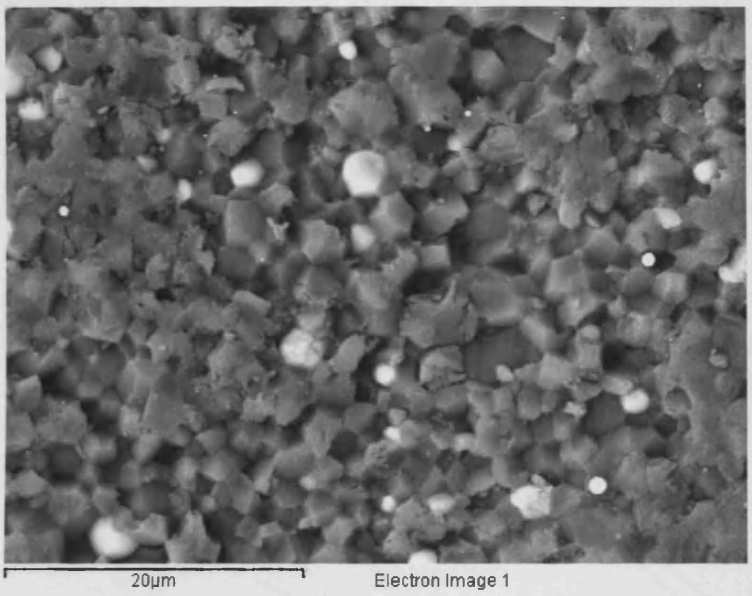

Figure 4.4: The SEM image of $Gd_5Si_{2.08}Ge_{1.92}$ film deposited on AlN substrate at 285 °C. The average size of a grain is $\sim$1.5 μm.

4.5.3 Magnetic phase transformation

$Gd_5(Si_xGe_{1-x})_4$ is known to exhibit a first order magnetostructural phase transformation close to room temperature for the composition $0.4<x<0.575$ [Pecharsky et al., 2002] which can be induced by changing temperature or applied magnetic field. This transition from orthorhombic (low temperature) to monoclinic (high temperature) is also accompanied by a change in bonding and a volumetric change in the crystal lattice. Accompanying this phase change are large changes in the magnetic, thermal and electrical properties of the material. These are giant magnetocaloric, giant magnetoelastic and giant magnetoresistance effects. The first order phase transformation in magnetocaloric materials exhibits hysteresis.

The first order phase transformation of $Gd_5(Si_xGe_{1-x})_4$ ($0.4<x<0.575$) can

be determined from measuring magnetic moment as a function of temperature at an applied magnetic field. It should also be noted that the magnetic order/disorder transition temperature is a function of applied magnetic field. The first order transition temperature was found to increase with increasing magnetic field in both single crystal and polycrystalline $Gd_5(Si_xGe_{1-x})_4$ ($0.4<x<0.575$) materials at a rate of ~5 K/T [Hadimani, 2010].

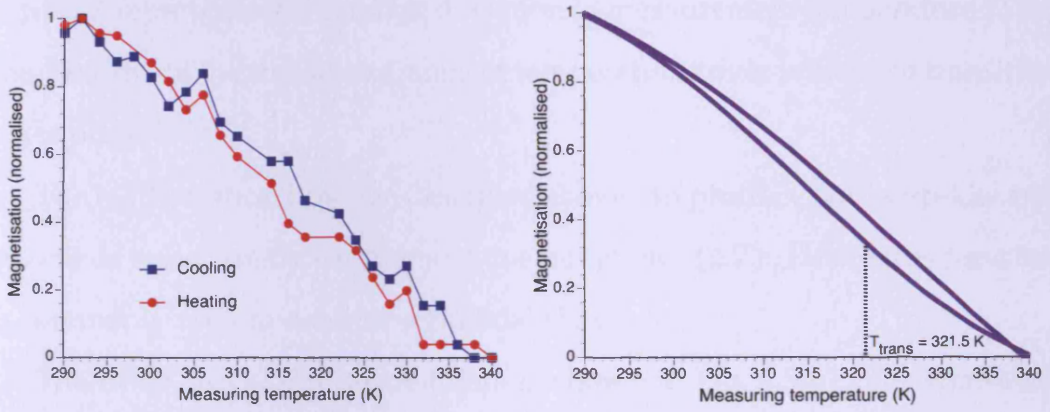

Figure 4.5: Magnetisation versus temperature curve of $Gd_5Si_{2.08}Ge_{1.92}$ thin film deposited on AlN substrate at 285 °C (a) Measured and (b) Sigmoidal fit of the measured data.

The moment versus temperature measurements were carried out on a SQUID magnetometer. The temperature was swept from 340 K to 290 K (cooling) and 290 K to 340 K (heating) at a rate of 2 K/min. A magnetic field of 4000 kA/m (μ_0H=5 T) was applied during the measurement to enhance the signal-to-noise ratio in the data.

The measured variation of magnetisation with temperature is shown in Fig. 4.5(a). In order to determine the transition temperature, the measured data was fitted to a Boltzmann function of the form given in equation (4.1).

For example, to fit the heating curve (from 290 K to 340 K), the equation is

$$y = \frac{M_{290K} - M_{340K}}{1 + e^{\frac{|T| - T_s}{\Delta T}}} + M_{340K} \tag{4.1}$$

where y is the fitted curve, M_{290K} is the value of M at 290 K, M_{340K} is the value of M at 340 K, T is the temperature, T_s is the phase transition temperature, ΔT represents the standard deviation in measurement temperature T, i.e. the "width" of the transition (range of temperatures over which the transition takes place).

The mathematical function described above can produce both step-like and smoother transition by varying just one parameter (ΔT). Hence this function is commonly used to describe sigmoidal shapes.

The fitted curve of measured data is shown in Fig. 4.5(b). The transition temperature was then determined from the fit and is ~321.5 K. This value is consistent with the value of the first order magnetostructural transition temperature observed in polycrystalline $Gd_5Si_{2.09}Ge_{1.91}$ bulk material (~320 K) measured at ~4000 kA/m (μ_0H=5 T) applied field [Hadimani, 2010].

Although a magnetic phase transformation was observed (Fig. 4.5(a)), it is not easy to distinguish between first and second order transitions from only one M vs. T measurement. It is known that the first order phase transition temperature T_s shifts by 5 K for every ~800 kA/m (μ_0H=1 T) change in applied magnetic field. A second order phase transformation would be expected to change shape (become sharper with decreasing field) with little change in transition temperature. Hence to determine the type of magnetic phase transition (first or second order), M vs. T at different applied fields should be carried

out.

The growth of magnetocaloric films based on $Gd_5Si_2Ge_2$ at a lower substrate temperature (285 °C) and the magnetic phase transformation at near room temperature indicate that these films are potential candidates in micro-cooling applications.

As the research on $Gd_5Si_2Ge_2$ thin films is in its initial stage, only the preliminary results are reported here. The electrical resistivity, heat capacity, magnetic hysteresis, moment vs. temperature at different applied fields and magnetostriction measurements on this thin film are underway and will be reported subsequently.

4.6 Summary

- The first successful thin film of $Gd_5Si_{2.08}Ge_{1.92}$ was grown on AlN substrate using PLD at a substrate temperature of 285 °C. The choice of deposition parameters was explained.
- The film was characterised to study crystallographic structure, composition and grain size.
- The θ-2θ XRD scans show monoclinic structure. This was confirmed by matching the PDF library pattern of monoclinic $Gd_5Si_2Ge_2$.
- The secondary phases were calculated using FULLPROF software and were compared with the measured XRD scan. There was no evidence of a substantial amount of secondary phases found in the film.

- It was concluded that for a thorough understanding of crystal structure, Rietveld refinement is required.
- A magnetic phase transformation near room temperature was observed in the magnetisation versus temperature study. The type of magnetic phase transformation (first or second order) is yet to be determined.
- This property of thin film makes it an attractive candidate for micro-cooling applications.

Chapter 5

Extensions to Jiles-Atherton theory of hysteresis

5.1 Introduction

This chapter focuses on modelling aspects of magnetic hysteresis curves. The theory and principle of Jiles-Atherton (JA) model of hysteresis are discussed in the following section. The extensions to this theory carried out as part of this research work are elaborated in the subsequent sections. Firstly, the modelling of temperature dependence of hysteresis based on JA theory is explained in Section 5.3. The functional form of anhysteretic magnetisation has been derived in Section 5.4. The extension of JA theory to model and predict the behaviour of two-phase materials is described in Section 5.5.

5.2 Jiles-Atherton theory

The theory of ferromagnetic hysteresis developed by Jiles and Atherton (JA), compared to other existing theories takes a more general approach in modelling the behaviour of magnetic materials in microscopic scale [Jiles & Atherton, 1986]. The model is built on the Langevin-Weiss classical model and considers an array of magnetic domains in thermal equilibrium at a particular temperature. The orientations of the magnetic moments are assumed to follow a statistical distribution. The bulk magnetisation can be obtained by simply integrating the distribution of moments over all possible orientations. This technique depends highly on the anisotropy of the material and the resulting magnetisation can take different forms based on whether the material is axially anisotropic or planar anisotropic or isotropic as explained in Section 5.4.

Ferromagnetic materials when subjected to external magnetic field change their magnetisation path. The path the magnetisation curve takes depends on whether the field is increasing or decreasing. This path-dependent behaviour exhibits irreversibility and hence hysteresis. According to JA theory, the change in total magnetisation, M, of a ferromagnetic material can be calculated from microstructural domain processes that contribute to irreversible, M_{irr}, and reversible, M_{rev}, changes in magnetisation components.

$$\Delta M = \Delta M_{irr} + \Delta M_{rev}. \tag{5.1}$$

Before proceeding further, it is important to describe the five microstructural parameters that form the basis of JA theory:

a. **Spontaneous magnetisation (M_S)**

The spontaneous magnetisation is one of the hallmarks of strong magnetic behaviour in ferromagnetic materials, which is produced by the parallel alignment of moments in a domain with the applied field. Technical saturation is reached when the spontaneous magnetisation of all domains is parallel to the field and hence there is only one domain in the material.

b. **Pinning parameter (k)**

The pinning parameter is a microstructural representation of the coercivity of the material. It is proportional to the product of pinning site energy and pinning density. In soft magnetic materials, the pinning parameter can be approximated by the coercive field [Jiles, 1991].

c. **Domain density (a)**

The domain density, a factor representing the number of magnetic domains in the material, influences the slope of the hysteresis curve and hence is a measure of permeability of the material.

d. **Domain coupling (α)**

The domain coupling represents the indirect mean field coupling between the domains in the material. This parameter is related to remanence point in the hysteresis behaviour.

e. **Reversibility parameter (c)**

The reversibility parameter, a representation of reversible domain wall motion and bending, is a measure of reversible magnetisation compo-

nent.

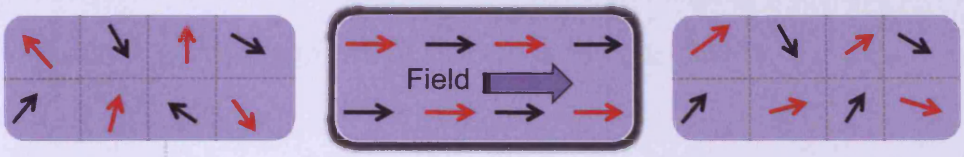

Figure 5.1: Origin of irreversible and reversible magnetisation.

A simple schematic of the origin of irreversible and reversible components is shown in Fig. 5.1. In ferromagnetic materials, when there is no external magnetic field the orientations of magnetic moments are random in nature. As soon as the field is applied and approaches saturation, the moments tend to align themselves parallel to the field. When the field is removed, not all moments go back to their initial state resulting in an irreversible magnetisation component. This simplified sketch does not show in detail the complex irreversible and reversible domain wall motion.

1. Irreversible component

   In the model the irreversible component of magnetisation is mainly attributed to the pinning of domain walls. However it can also include other loss mechanisms where the loss is proportional to the change in magnetisation.

2. Reversible component

   The reversible magnetisation component results from the contribution of reversible bowing of domain walls. This mainly arises from the domain wall displacement which is reversible in nature.

Considering the two magnetisation components, M_{irr} and M_{rev}, derived from microstructural processes, the equations describing the dependence of magnetisation, M, on magnetic field, H, can be constructed:

$$M_{irr} = M_{an} - k\delta\frac{dM_{irr}}{dH_e} \tag{5.2}$$

$$M_{rev} = c\,(M_{an} - M_{irr}) \tag{5.3}$$

where M_{an} is the anhysteretic magnetisation and δ is the directional parameter that takes the value +1 when H increases and -1 when H decreases. The effective field term, $H_e = H + \alpha M$, arises from the contributions of applied field and magnetic interactions between domains.

Substituting equations (5.2) and (5.3) into (5.1) gives the microstructure-dependent model of hysteresis based on JA theory. Figure 5.2 shows a typical hysteresis loop of a magnetic material generated using JA theory with microstructural parameters that influence the shape of the loop and hence the magnetic properties of the material.

Several studies have been carried out successfully to extend the JA theory to include magnetoelastic, thermal, frequency and anisotropy effects. In 1984, the JA theory was applied to explain the magnetomechanical effect on the assumption that the applied stress causes the domain walls to break away from their pinning sites and hence the magnetisation approaches an anhysteretic state [Jiles & Atherton, 1984]. Later, Sablik and Jiles had developed a magnetoelastic model based on this theory to incorporate stress dependence of hysteresis [Sablik & Jiles, 1993]. The model couples magnetic and magnetostrictive hysteresis through the derivative of magnetostriction with respect

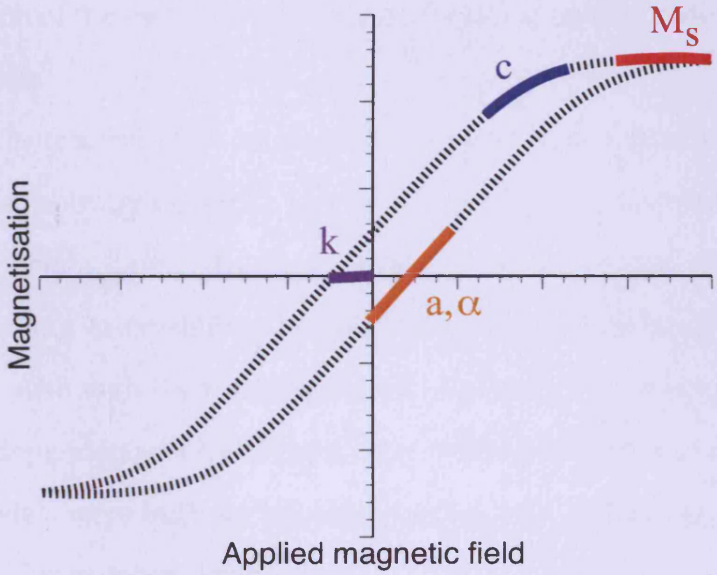

Figure 5.2: Typical hysteresis curve showing the magnetic response of a material to the applied magnetic field. The five microstructural parameters influence the respective specified regions of the hysteresis curve.

to magnetisation. This physical model was validated against measurements made on wide range of materials from polycrystalline iron to Ni-Zn ferrites and was found to be in excellent agreement in all cases.

Further attempts to extend the JA model to include thermal effects were based on fitting of model parameters to the experimental data [Andrei et al., 2007; Wilson et al., 2002].

The JA theory of hysteresis had been extended to incorporate the frequency dependence in both electrically non-conducting [Jiles, 1993] and conducting [Jiles, 1994a] magnetic materials. For the electrically conducting case, the theory was built on the classical and anomalous loss terms by modelling the influence of eddy current losses [Jiles, 1994b]. For the electrically non-conducting materials where eddy currents do not play a role, the model was based on the

representation of the motion of domain walls using second order linear differential equation.

The effects of anisotropy on hysteresis was modelled by Ramesh et al. by deriving an anisotropy-dependent anhysteretic magnetisation function [Ramesh et al., 1997, 1996]. Later, Jiles et al. applied the anisotropy-dependent hysteresis modelling to crystalline and textured materials [Jiles et al., 1997; Shi et al., 1998]. Although there were partially successful attempts to incorporate anisotropy dependence of hysteresis, the resulting model was not complete as all these models were built for known specific cases and do not have a generalised form of anisotropy dependence.

Several algorithms have been developed to extract microstructural parameters from the measured hysteresis loop based on this theory of hysteresis. A review of estimation methods can be found in [Chwastek, 2008]. One such algorithm based on numerical determination of microstructural parameters developed by Jiles et al. has been well-established and proven to be reliable [Jiles & Thoelke, 1989; Jiles et al., 1992].

It is worth mentioning here the recent work on developing new capabilities of JA theory to model dynamic hysteresis loops [Chwastek, 2009].

5.3 Thermal dependence of hysteresis

The magnetisation processes in ferromagnetic materials are highly dependent on temperature. In order to understand thoroughly the behaviour of magnetisation processes in ferromagnetic materials at different temperatures, a temperature-dependent hysteresis model based on the microstructural pro-

cesses is necessary.

5.3.1 Temperature dependence of microstructural parameters

In the present work, the effects of temperature on magnetic hysteresis have been incorporated into the existing theory by representing the five microstructural model parameters: spontaneous magnetisation, M_S, pinning, k, domain density, a, domain coupling, α, and reversibility, c, as functions of temperature, T. The material dependent parameters such as Curie temperature, T_C, and critical exponent, β, have also been added as additional variables to the existing model. The Curie temperature is the temperature at which the ferromagnetic material becomes paramagnetic. In other words, the orientation of moments becomes random and hence the spontaneous magnetisation becomes zero. The critical exponent is a representation of mean field interactions in the material and can be derived from mean field theory [Arrott & Noakes, 1967].

a. M_S vs. T

The spontaneous magnetisation of a ferromagnetic material decreases with increasing temperature and reaches zero at the Curie temperature when it becomes paramagnetic. The Weiss theory of ferromagnetism describes this temperature dependence of spontaneous magnetisation as [Chikazumi, 1984]

$$M_S(T) = M_S(0)\left(1 - \frac{T}{T_C}\right)^{\beta} \tag{5.4}$$

b. k vs. T

The pinning parameter is proportional to the coercivity of the material, which

decreases exponentially with increasing temperature, indicating that the pinning energy of domain walls decays with temperature.

$$k(T) = k(0)\exp\left(\frac{-1}{\beta'}\frac{T}{T_C}\right) \tag{5.5}$$

The critical exponent factor β' of pinning parameter is different from the critical exponent β of spontaneous magnetisation and this indicates that there can be different critical exponent values for different parameters.

c. a vs. T

The temperature-dependent JA model was developed for two cases of domain density as follows:

case 1: In this case, the domain density was assumed to be constant as it showed only negligible variation with temperature [Wilson et al., 2002].

case 2: As the temperature increases, the domain walls break away from pinning sites and consequently cause a reduction in the density of domains in the material. Hence the domain density, similar to the pinning parameter, was made to decrease exponentially with temperature in this case.

$$a(T) = a(0)\exp\left(\frac{-1}{\beta''}\frac{T}{T_C}\right) \tag{5.6}$$

d. α vs. T

For isotropic materials, the domain coupling can be represented as a function of domain density and spontaneous magnetisation and is given by [Jiles et al., 1992]

$$\alpha = \frac{3a}{M_S} - \frac{1}{\chi_{an}} \tag{5.7}$$

At higher anhysteretic susceptibilities, χ_{an}, the contribution of the second term to domain coupling is negligible. Hence by substituting the corresponding expressions of M_S and a, the temperature dependence of domain density can be obtained.

e. c vs. T

For isotropic materials, the reversibility parameter can be treated in an analogous way to that of domain coupling and is given by [Jiles et al., 1992]

$$c = \frac{3a}{M_S}\chi_{in} \tag{5.8}$$

Assuming constant initial susceptibility, χ_{in}, and substituting the expressions of M_S and a, the relation between reversibility parameter and temperature can be determined.

5.3.2 Parameter identification

The initial conditions of the model such as the values of parameters at 0 K, the initial susceptibility and anhysteretic susceptibility can be determined, using well-documented identification procedures, from measured data at low temperatures [Jiles et al., 1992]. The Curie temperature and critical exponent can be estimated from measuring M_S vs. T and fitting the model equation given in (5.4) to the measured data. By following the above estimation procedure, all parameters that are necessary to describe the ferromagnetic behaviour below

the Curie temperature can be determined.

5.3.3 Model validation

The temperature dependent extension of the JA model was validated against measurements made on cation substituted cobalt ferrite material with composition $Co_{1.4}Ge_{0.4}Fe_{1.2}O_4$. The Curie temperature of this material was measured as 550 K [Song, 2007]. The hysteresis loops were measured using a SQUID magnetometer at various temperatures ranging from 10 K to 400 K. As the temperature capability of the SQUID system is from 4.2 K to 400 K, measurements cannot be made up to the Curie temperature. The measured hysteresis loops were compared with those calculated using the proposed model.

The measured spontaneous magnetisation versus temperature is shown in Fig. 5.3(a). The measured data was fitted to the model equation (5.4) to determine the critical exponent ($\beta = 0.45$). As shown in Fig. 5.3(b), the spontaneous magnetisation drops rapidly to zero at 550 K indicating the transition from a magnetically ordered state (ferrimagnetic) to a magnetically disordered state (paramagnetic).

The pinning parameter was calculated from equation (5.5) assuming that $\beta' = \frac{\beta}{2}$. As shown in Fig. 5.4(a), the pinning parameter drops exponentially with increasing temperature indicating the exponential decrease of coercive field [Hauschild et al., 2002]. Figure 5.4(b) compares the measured coercive field with the calculated pinning parameter and calculated coercive field. The measured and calculated coercive fields are in excellent agreement. The agreement between pinning parameter and coercive fields shows that, in soft mag-

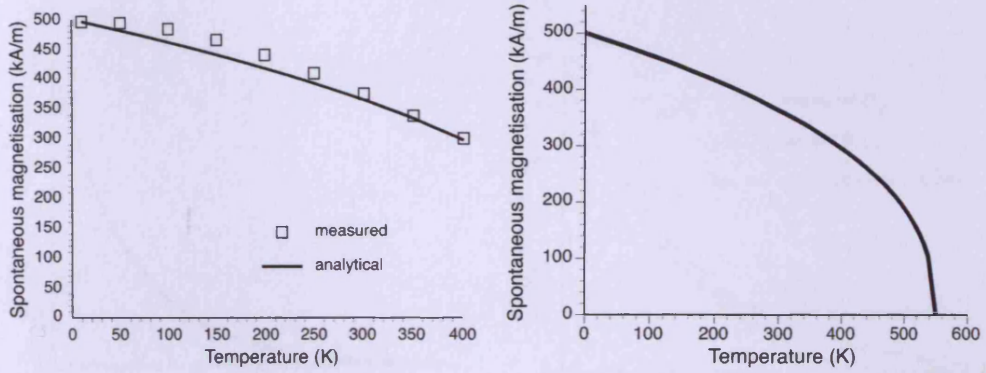

Figure 5.3: (a) The measured spontaneous magnetisation of a substituted cobalt ferrite at different temperatures. (b) The calculated temperature dependence of spontaneous magnetisation shows that at the Curie temperature (550 K) there is a transition from ferrimagnetic to paramagnetic state.

netic materials, the pinning parameter can be approximated to the coercive field of the material.

(a) Case 1

In this case, the domain density was assumed to be independent of temperature. Hence, from model equations (5.7) and (5.8), the domain coupling, α, and reversibility parameter, c, increase monotonically with temperature as shown in Figs. 5.5(a) and 5.5(b) respectively. However, the reversibility parameter has an upper limit of 1 at or before the Curie point.

(b) Case 2

As explained in Section 5.3.1, the domain density was modelled to exponentially decrease with increasing temperature as shown in equation (5.6) with an assumption that the critical exponent $\beta'' = \frac{\beta}{2}$. This behaviour, as shown in Fig. 5.6(a), is analogous to that of the pinning site density. The domain coupling and reversibility parameter, calculated from M_S and a using known

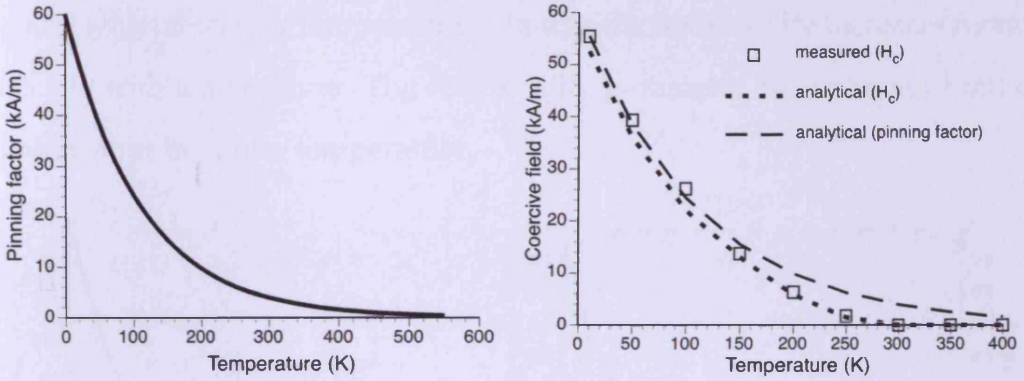

(a) (b)

Figure 5.4: (a) The pinning parameter calculated from the model equation up to the Curie temperature. (b) The measured coercive field is compared with the coercive field calculated from the model and the pinning parameter. It is clear from the figure that, in soft magnetic materials, the pinning parameter can be approximated to coercivity.

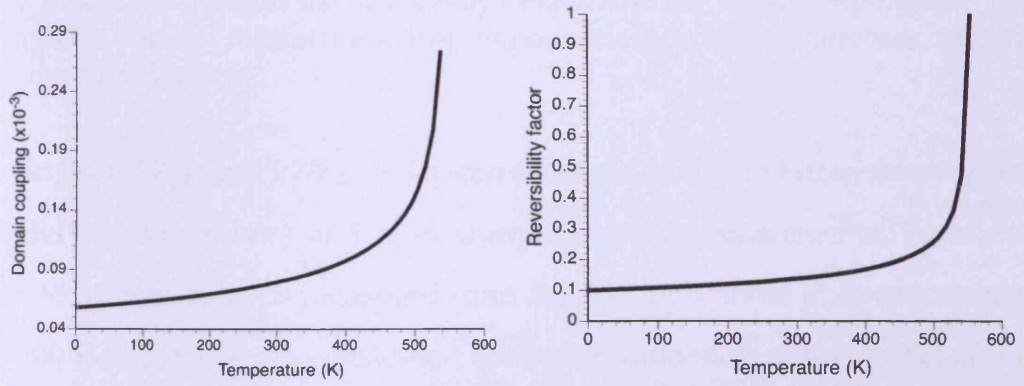

(a) (b)

Figure 5.5: (a) and (b) show the temperature dependence of domain coupling and reversibility parameter respectively when the domain density was assumed to be constant with temperature. Although both the parameters increase monotonically with increasing temperature, reversibility parameter has an upper limit of 1.

equations, are plotted in Fig. 5.6(b). The magnetic domain interactions decay rapidly with increasing temperature whereas the reversibility increases monotonically with temperature. The reversibility parameter has an upper limit of 1 before or at the Curie temperature.

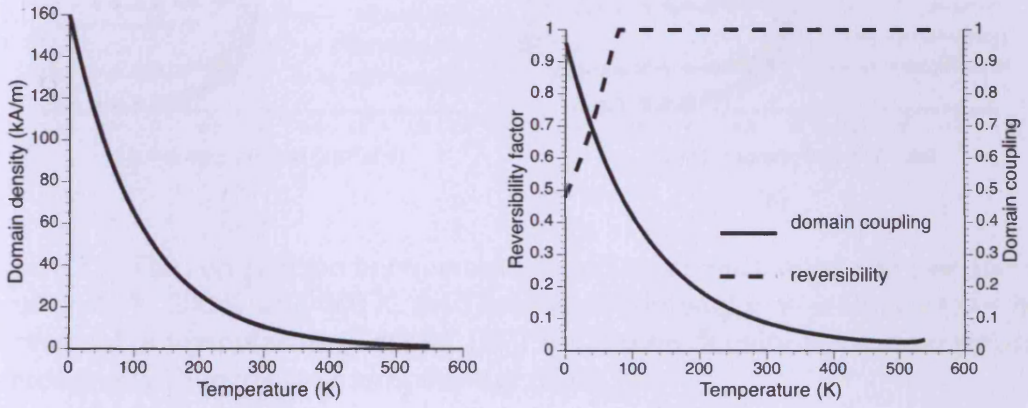

Figure 5.6: (a) The exponential decrease of domain density with temperature. (b) The temperature dependence of domain coupling and reversibility parameter when the domain density decays exponentially with temperature. The magnetic domain interactions drop exponentially with temperature, same as the domain density.

In Figs. 5.7(a) and 5.7(b), the hysteresis loops, calculated from the proposed model based on cases 1 and 2, are compared with measurements. From a series of hysteresis loops measured from SQUID, only those at temperatures 0 K, 200 K and 400 K are considered for better validation of the model at low, intermediate and high temperatures (near Curie temperature). The measured hysteresis loops flatten at higher temperatures indicating the decrease of spontaneous magnetisation and the existence of a transition from ferrimagnetic to paramagnetic state.

As can be seen from Fig. 5.7(a), the loops calculated based on Case 1 show a

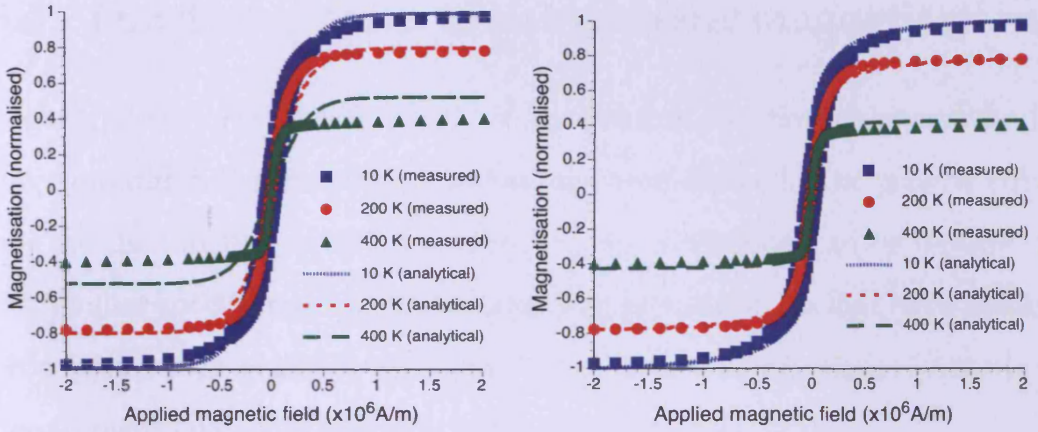

Figure 5.7: The comparison between measured hysteresis loops and calculated loops at 10 K, 200 K, and 400 K. (a) The domain density was assumed to be independent of temperature (Case 1). (b) The domain density was exponentially decreasing with increasing temperature (Case 2).

reasonably good match with measured loops at lower temperatures (10 K and 200 K), but deviate at higher temperatures (400 K). This is mainly due to the assumptions that the domain density and the susceptibilities are independent of temperature. The Case 2, shown in Fig. 5.7(b) in which the domain density varies with temperature shows an excellent agreement between the calculated and measured hysteresis loops at all temperatures. However, at higher temperatures, there seems to be a deviation but comparatively smaller than the ones calculated based on Case 1.

Implementing an analytical expression of temperature dependence of initial and anhysteretic susceptibilities can further improve the proposed model.

5.4 Functional form of anhysteretic magnetisation

A generalised form of anhysteretic magnetisation function to extend the JA theory to different forms of anisotropy has been derived. The general equation for the function, with necessary limiting conditions, can be reduced to the familiar specific model equations in the particular cases that have already been solved such as axially anisotropic (one-dimensional), planar anisotropic (two-dimensional), and isotropic (three-dimensional).

5.4.1 Anhysteretic magnetisation

The JA theory of hysteresis is built on the anhysteretic magnetisation function, which is the function of energy of moments in a domain. As the name indicates, it is the response of the material to applied field that does not involve hysteresis. In other words, the loss factor or the pinning is zero. In the model, the magnetic hysteresis is obtained by combining a loss factor in the form of pinning constant, k, with the anhysteretic magnetisation function. A typical anhysteretic magnetisation vs. applied magnetic field curve of an isotropic material and its corresponding hysteresis curve are shown in Figs. 5.8(a) and 5.8(b).

The anhysteretic magnetisation function can take different forms depending on the anisotropy of the material. The anhysteretic function for an axially anisotropic material with applied field along the easy axis, is [Bertotti, 1998]:

$$M_{an} = M_S \left(\tanh\left(h\right)\right) , \tag{5.9}$$

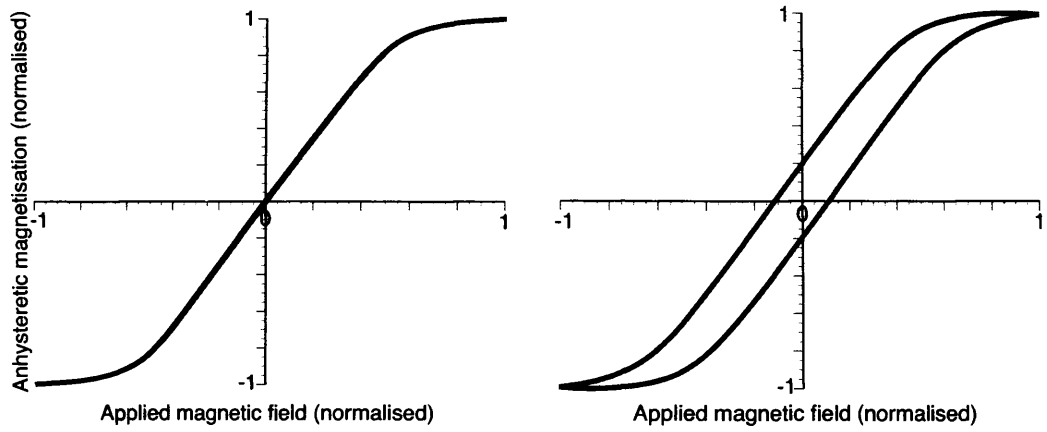

Figure 5.8: (a) A typical anhysteretic magnetisation curve of isotropic material modelled using Langevin function. (b) The corresponding hysteresis curve obtained by combining the anhysteretic with the loss factor.

For a planar anisotropic material (2-D case) with applied field in the easy plane [Jiles et al., 2000],

$$M_{an} = M_S \left(\frac{\sum_{n=0}^{\infty} \frac{h^{2n+1}}{(n+1)!\, 2^{2n+1}}}{1 + \sum_{n=0}^{\infty} \frac{h^{2(n+1)}}{(n+1)!\, 2^{2(n+1)}}} \right), \tag{5.10}$$

For completely isotropic materials (3-D case) [Jiles, 1991],

$$M_{an} = M_S \left(\coth(h) - \frac{1}{h} \right), \tag{5.11}$$

where $h = \frac{H_e}{a}$; H_e is the effective field; $a = \frac{k_B T}{\mu_0 m}$; k_B is Boltzmann constant; T is the temperature; μ_0 is the permeability of vacuum and m is the magnetic moment of a typical domain.

5.4.2 Need for a functional form

Until recently the hysteresis behaviour of anisotropic or isotropic materials was modelled using JA theory by solving the respective known anhysteretic magnetisation function shown in equations (5.9)–(5.11). It is important to note that there are only three specific cases of anisotropy that have already been solved. This limits, to a greater extent, the capability of the model to describe several other anisotropies that exist in real-world materials. Moreover, none of those specific cases described in Section 5.4.1 is a function of the anisotropy constant, which is an important parameter to be considered while modelling anisotropic materials. Hence, in order to extend the JA theory to study or predict the hysteresis behaviour in anisotropic materials, there is a need to derive a functional form of anhysteretic magnetisation function.

5.4.3 Thermodynamics of the anhysteretic function

When subjected to an external magnetic field, each magnetic moment has a potential energy that tries to align it parallel to the applied field. This energy is given by

$$\begin{aligned} E_m &= -\mu_0 m \cdot H_e \\ &= -\mu_0 m H_e \cos\theta \end{aligned} \tag{5.12}$$

where m is the moment and H_e is the effective magnetic field, which represents the contributions of applied magnetic field and domain coupling. The

anisotropy energy, for uniaxial materials, can be written to lowest order as

$$E_a = K_u \sin^2 \Omega \tag{5.13}$$

where K_u is the anisotropy constant; Ω and θ are the angles made by the magnetic moment with respect to the unique axis and applied field respectively.

According to statistical thermodynamics, assuming no direct interaction between the domains, the individual partition function can be represented as [Bertotti, 1998]

$$\begin{aligned} Z_m &= \sum_{states} \exp\left(\frac{-(E_m + E_a)}{k_B T}\right) \\ &= \sum_{states} \exp\left(h\cos\theta - \kappa \sin^2 \Omega\right) \end{aligned} \tag{5.14}$$

where h and κ are energy ratios and are given by

$$h = \frac{H_e}{a}; \kappa = \frac{K_u}{k_B T}; a = \frac{k_B T}{\mu_0 m}.$$

The interaction in this case depends on an indirect mean field coupling. The total partition function, Z, associated with N independent moments is given in terms of individual partition functions by $(Z_m)^N$. The Gibbs free energy can be calculated from the total partition function as

$$\begin{aligned} G &= -k_B T \ln Z \\ &= -N k_B T \ln Z_m \,. \end{aligned} \tag{5.15}$$

The anhysteretic magnetisation, M_{an}, which is a function of energy of N moments occupying a volume ΔV in a domain, can be expressed as a change in

Gibbs free energy with respect to the field at constant temperature [Bertotti, 1998].

$$M_{an} = -\frac{1}{\mu_0 \Delta V}\left[\frac{\partial G}{\partial H_e}\right]_T . \tag{5.16}$$

5.4.4 Derivation of functional form

From equations (5.15) and (5.16), in order to derive a functional form of anhysteretic magnetisation, the partition function, Z, should have a generalised form. Hence the integral form of individual partition function, Z_m, based on the spherical coordinate system shown in Fig. 5.9, can be written as

$$Z_m = \int_0^{2\pi}\int_0^{\pi} \exp\left(h\cos\theta - \kappa \sin^2\Omega\right) \sin\theta \, d\theta \, d\varphi . \tag{5.17}$$

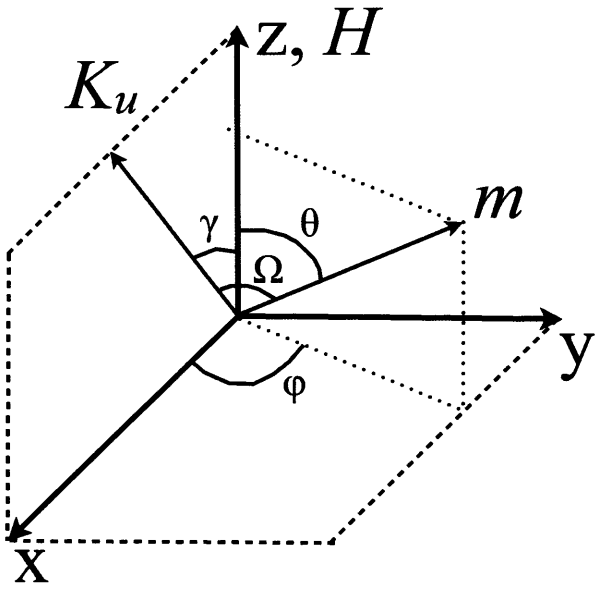

Figure 5.9: The spherical coordinate system representation of magnetic vectors. The applied magnetic field is along z-direction, the anisotropy vector K_u and the moment m make angles γ and θ with the applied field respectively.

From equation (5.15), the Gibbs free energy can be calculated as

$$G = -Nk_BT \ln \left(\int_0^{2\pi} \int_0^{\pi} \exp\left(h\cos\theta - \kappa \sin^2 \Omega\right) \sin\theta \, d\theta \, d\varphi \right), \tag{5.18}$$

The anhysteretic magnetisation can then be derived from Gibbs free energy using equation (5.16) as

$$M_{an} = \frac{Nk_BT}{\mu_0 \Delta V} \frac{\partial}{\partial H_e} \left[\ln \left(\int_0^{2\pi} \int_0^{\pi} \exp\left(h\cos\theta - \kappa \sin^2 \Omega\right) \sin\theta \, d\theta \, d\varphi \right) \right] \tag{5.19}$$

Taking the partial derivative w.r.t H_e we get,

$$M_{an} = M_S \frac{\int_0^{2\pi} \int_0^{\pi} \exp\left(h\cos\theta - \kappa \sin^2 \Omega\right) \sin\theta \cos\theta \, d\theta \, d\varphi}{\int_0^{2\pi} \int_0^{\pi} \exp\left(h\cos\theta - \kappa \sin^2 \Omega\right) \sin\theta \, d\theta \, d\varphi}. \tag{5.20}$$

where M_S is the spontaneous magnetisation and is given by $M_S = \dfrac{Nm}{\Delta V}$.

In order to generalize the anhysteretic magnetisation function shown in equation (5.20), the angle made by moments with anisotropy axis, Ω, should be represented in terms of other known angle parameters. This can be achieved by defining the direction cosines of K_u and m from the spherical coordinate system.

From Fig. 5.9(a)), the direction cosines of K_u and m can be written as

$$\begin{aligned} K_u &: (\sin\gamma, 0, \cos\gamma) \\ m &: (\sin\theta\cos\varphi, \sin\theta\sin\varphi, \cos\theta) \end{aligned}$$

The scalar product yields

$$m \cdot K_u = |m||K_u| \cos \Omega, \tag{5.21}$$

On substitution of direction cosines,

$$\cos \Omega = \sin \gamma \sin \theta \cos \varphi + \cos \gamma \cos \theta \tag{5.22}$$

On substituting equation (5.22) into (5.20) using a known trigonometric identity ($\sin^2 \Omega + \cos^2 \Omega = 1$), we get

$$M_{an} = M_S \frac{\int_0^{2\pi}\int_0^{\pi} \exp\left(h \cos\theta - \kappa\left[1 - \cos^2 \Omega\right]\right) \sin\theta \cos\theta \, d\theta \, d\varphi}{\int_0^{2\pi}\int_0^{\pi} \exp\left(h \cos\theta - \kappa\left[1 - \cos^2 \Omega\right]\right) \sin\theta \, d\theta \, d\varphi} \tag{5.23}$$

Equation (5.23) is the generalised form of anhysteretic magnetisation function, which with suitable limiting conditions, can be reduced to known specific model equations of particular cases.

5.4.5 Validation of functional form

The generalised form of anhysteretic magnetisation function can be validated against the model equations for specific cases: axially anisotropic, planar anisotropic and isotropic. Figure 5.10 shows the three specific cases of anisotropic materials that have known expressions for anhysteretic magnetisation function.

a. Axially anisotropic case

Consider the axially anisotropic case where the anisotropy constant is positive

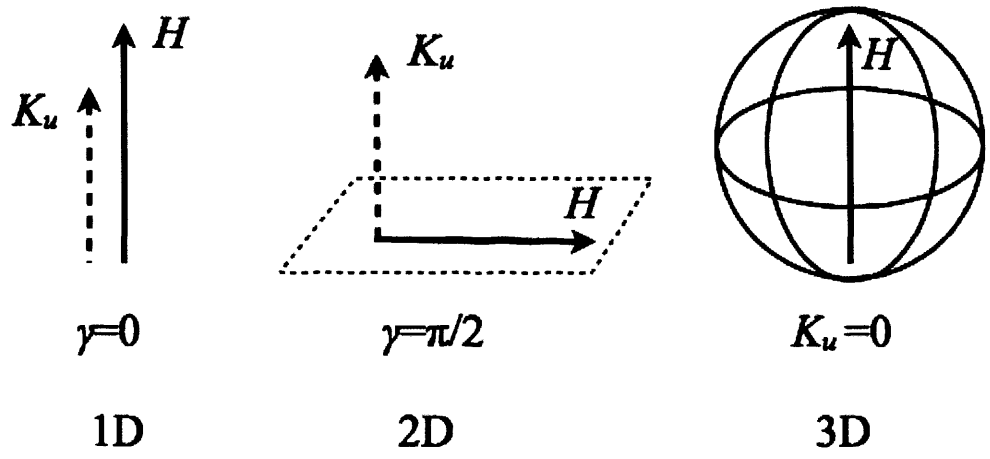

Figure 5.10: Multi-dimensional representation of anisotropy. The 1-D case represents easy axis, 2-D case represents easy plane and 3-D case represents isotropy where there is no preferred orientation.

and the applied field is parallel to the anisotropic easy direction, i.e. γ=0. In the case of extremely high anisotropy, the moments can be either spin-up or spin-down reducing to a one-dimensional problem as shown in Fig. 5.10.

On substituting γ=0 in the generalised form in equation (5.23) we get,

$$M_{an} = M_S \frac{\int_0^{2\pi}\int_0^{\pi} \exp\left(h\cos\theta - \kappa[1-\cos^2\theta]\right)\sin\theta\cos\theta\, d\theta\, d\varphi}{\int_0^{2\pi}\int_0^{\pi} \exp\left(h\cos\theta - \kappa[1-\cos^2\theta]\right)\sin\theta\, d\theta\, d\varphi} \tag{5.24}$$

On integration,

$$M_{an} = M_S \frac{\left[[\exp(2h)-1]\sqrt{\kappa} + hF\left(\frac{h-2\kappa}{2\sqrt{\kappa}}\right) - \exp(2h)hF\left(\frac{h+2\kappa}{2\sqrt{\kappa}}\right)\right]}{2\kappa\left[-F\left(\frac{h-2\kappa}{2\sqrt{\kappa}}\right) + \exp(2h)F\left(\frac{h+2\kappa}{2\sqrt{\kappa}}\right)\right]} \tag{5.25}$$

where F(x) is Dawson's integral and is given by

$$F(x) = \exp(-x^2) \int_0^x \exp(t^2) dt$$

For large $|x|$, the function $F(x) \approx \frac{1}{2x}$. The complete derivation of equation (5.25) from (A.1) is given in Appendix A.

In the case of extremely high anisotropy, K_u tends to $+\infty$ (i.e. κ tends to $+\infty$), applying the above boundary condition in equation (5.25) and neglecting higher order terms, we get

$$M_{an} \approx M_S \left(\tanh\left(h\right)\right). \tag{5.26}$$

This solution is the same as the axially anisotropic case shown in equation (5.9). The derivation is given in Appendix B.

b. Planar anisotropic case

Consider that the anisotropy is negative and the applied field is in the easy plane i.e. $\gamma = \frac{\pi}{2}$. As shown in Fig. 5.10, unlike the 1D case, the preferred direction in this case is a plane. Hence this case can be reduced to a two-dimensional problem in case of extremely high negative anisotropy.

On substitution of the boundary condition ($\gamma = \frac{\pi}{2}$) in the generalised functional form given in equation (5.23), we get

$$M_{an} = M_S \frac{\int_0^{2\pi}\int_0^{\pi} \exp\left(h\cos\theta - \kappa[1 - \sin^2\theta\cos^2\varphi]\right) \sin\theta\cos\theta \, d\theta \, d\varphi}{\int_0^{2\pi}\int_0^{\pi} \exp\left(h\cos\theta - \kappa[1 - \sin^2\theta\cos^2\varphi]\right) \sin\theta \, d\theta \, d\varphi} \tag{5.27}$$

On integration with respect to φ,

$$M_{an} = M_S \frac{\int_0^{\pi} \exp\left(h\cos\theta - \frac{\kappa}{4}[3+\cos 2\theta]\right) I_0\left(\frac{\kappa}{2}\sin^2\theta\right) \sin\theta\cos\theta\, d\theta}{\int_0^{\pi} \exp\left(h\cos\theta - \frac{\kappa}{4}[3+\cos 2\theta]\right) I_0\left(\frac{\kappa}{2}\sin^2\theta\right) \sin\theta\, d\theta} \tag{5.28}$$

where $I_0(x)$ is the modified Bessel function of the first kind. The derivation of the above equation can be found in Appendix B.

The procedure to solve this integral is similar to the one shown by Jiles et al. [Jiles et al., 2000] and the solution is given in equation (5.10). The solution is an infinite series and has no closed form. This can also be solved numerically and the solution gives the anhysteretic curve of planar anisotropic materials.

c. Isotropic case

When there is no preferred direction in a material, that is anisotropy is zero, i.e. K_u=0 and hence κ=0, this case has three-dimensional solution as shown in Fig. 5.10.

On substitution of the boundary condition in equation (5.23) we get

$$M_{an} = M_S \frac{\int_0^{2\pi}\int_0^{\pi} \exp\left(h\cos\theta\right) \cos\theta \sin\theta\, d\theta\, d\varphi}{\int_0^{2\pi}\int_0^{\pi} \exp\left(h\cos\theta\right) \sin\theta\, d\theta\, d\varphi} \tag{5.29}$$

Solving the above integral yields,

$$M_{an} = M_S \left(\coth\left(h\right) - \frac{1}{h}\right) \tag{5.30}$$

This Langevin's function is the same as the one shown in equation (5.11)

and it gives the anhysteretic magnetisation of isotropic materials.

Other than these specific cases, the hard direction anhysteretic magnetisation curve, when the applied field is orthogonal to the easy axis, can be calculated from the generalised function by using the limiting conditions $K_u > 0$ and $\gamma=\frac{\pi}{2}$, and is plotted in Fig. 5.11, which shows the plots of anhysteretic magnetisation function for various values of K_u and γ. These plots were obtained by numerically solving the generalised functional form, shown in equation (5.23), for various values of K_u and γ.

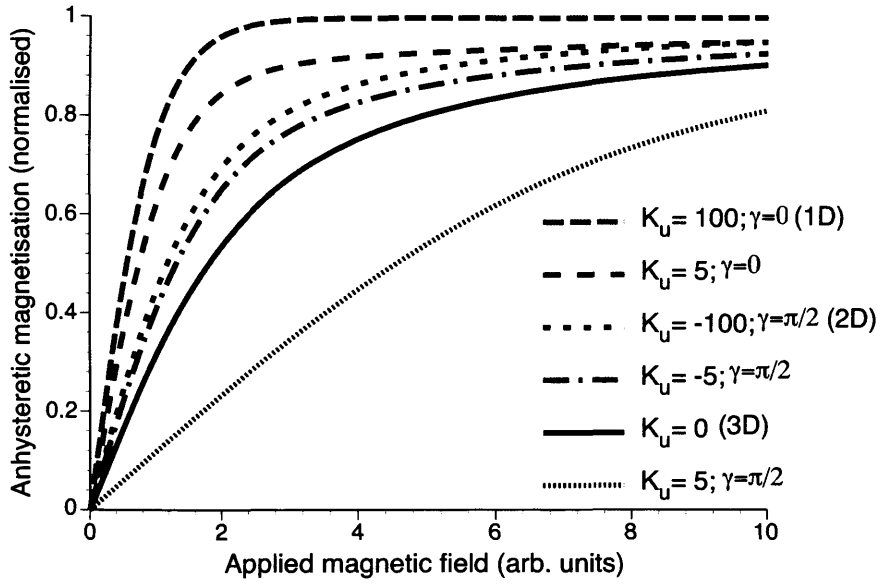

Figure 5.11: The plots show the anhysteretic magnetisation function for different anisotropies. The curves were calculated from the generalised functional form. The ($K_u > 0$, γ=0) represent uniaxial anisotropy with applied field along the easy axis, ($K_u < 0$, $\gamma=\frac{\pi}{2}$) represents planar anisotropy with applied field in the easy plane, K_u=0 represents isotropy, and ($K_u > 0$, $\gamma=\frac{\pi}{2}$) represents the hard direction anhysteretic magnetisation when the applied field is orthogonal to the uniaxial easy axis.

This generalised form of anhysteretic magnetisation function can also be extended for the easy cone or the multi-axial case by considering more than

one anisotropy constant in the anisotropy energy equation given in (5.13). Replacing the uniaxial anisotropy energy with cubic anisotropy energy and deriving the generalised form predicts precisely the hysteresis behaviour of cubic anisotropy materials.

5.5 Modelling of magnetic two-phase materials

Magnetic two-phase materials are those that exhibit two magnetic phases in one hysteresis cycle: one at lower fields and the other at higher fields. The transition from one phase to the other, i.e. low field phase to high field phase occurs at the exchange field. The exchange field is an inherent property of the material that represents the coupling between two different types of magnetic phases in a material. In order to understand completely the behaviour of magnetic two-phase materials, a reliable model based on microstructural processes is necessary. Hence, the JA theory of hysteresis has been extended to model magnetic two-phase materials by representing the five microstructural parameters: spontaneous magnetisation, M_S, pinning parameter, k, domain density, a, domain coupling, α, and reversibility parameter, c, as functions of the exchange field.

5.5.1 The model

Magnetic two-phase behaviour can be induced in magnetic materials by subjecting them to thermal treatment [Alexandrakis et al., 2009] or compressive stress [Moses & Davies, 1980]. Typical hysteresis behaviour of a two-phase material is shown in Fig. 5.12(a). It is evident from the figure that the hystere-

sis loop has two distinct regions, low field and high field, having completely different magnetic phase. Hence to model this hysteresis behaviour, two sets of microstructural parameters, one set for each magnetic phase, are required. Also, a simple-yet-robust mathematical function that could switch between two states in various ways, e.g. step-like, smooth etc., is necessary to describe easily the sharper or smoother transitions from one magnetic phase to the other based on the exchange field. A known mathematical function that can produce both step-like and smoother transition by varying just one parameter is the Boltzmann function and is represented as [Bender & Orszag, 1978]

$$y = \frac{A_1 - A_2}{1 + e^{\frac{|H| - H_{ex}}{\Delta H}}} + A_2 \tag{5.31}$$

where y is one of the JA parameters (M_S, k, a, c, and α), A_1 is the value of y in the low field magnetic phase, A_2 is the value of y in the high field magnetic phase, H is the applied magnetic field, H_{ex} is the exchange field of the material at which the transition from one magnetic phase to the other occurs, ΔH represents the range of fields over which the transition takes place i.e. the smoothness of transition between two magnetic phases.

Figure 5.12(b) shows the plot of Boltzmann function given in equation (5.31). Larger values of ΔH correspond to smoother transition whereas smaller values indicate abrupt transition (or step-like function).

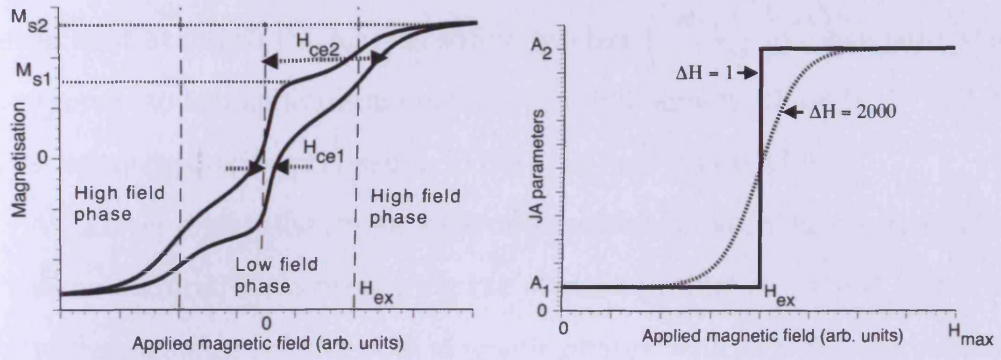

Figure 5.12: (a) Typical magnetic two-phase hysteresis behaviour. The material exhibits a low-field and a high-field magnetic phase below and above an exchange field, H_{ex}. (b) Boltzmann function that describes both step-like and smooth transition by variation of parameter ΔH.

5.5.2 Parameter identification

The initial values of the JA parameter set in Boltzmann's function can be estimated with the help of a well-established algorithm [Jiles et al., 1992] from measured initial and hysteresis curves of the samples in respective magnetic phases. Since the field parameters, H_{ex} and ΔH, determine respectively the transition field and smoothness of transition in the hysteresis, they should be functions of both magnetic phases. By measuring the effective coercive fields at both magnetic phases, H_{ex} can be represented as

$$H_{ex} = \frac{H_{ce1} + H_{ce2}}{2} \tag{5.32}$$

The effective coercivity at the low field magnetic phase (H_{ce1}) can be determined by measuring the field at which the total magnetisation is zero. At high field magnetic phase, the effective coercivity (H_{ce2}) can be approximated

as the field at which the magnetisation reaches $\left(\frac{M_{S1}+M_{S2}}{2}\right)$, where M_{S1} is the spontaneous magnetisation in the low field magnetic phase (LFP) and M_{S2} is the spontaneous magnetisation in the high field phase (HFP).

As ΔH represents the smoothness of transition between the magnetic phases, it can be deduced from measuring the slopes of initial curve just below and above the exchange field for both magnetic phases, which can be approximated as

$$\Delta H = \frac{1}{\left|\left[\frac{dM}{dH}\right]_{\text{LFP}} - \left[\frac{dM}{dH}\right]_{\text{HFP}}\right|} \tag{5.33}$$

By substituting the exchange field-dependent parameter set into the existing model shown in equations (5.1)–(5.3), we obtain a complete model based on JA theory that can predict two-phase behaviour in magnetic materials.

5.5.3 Typical examples of magnetic two-phase materials

There is a wide range of magnetic materials that exhibit two-phase magnetic behaviour such as hard-soft bi-layer thin films, micro-wires, multilayer structures that are used for perpendicular recording and even grain-oriented silicon-iron under compressive stress. With suitable conditions, as tabulated in Table 5.1, typical features of magnetic two-phase behaviour of materials such as hard-soft bi-layer thin films, grain-oriented silicon-iron and magnetic micro-wires, can be described using the proposed model.

Case 1: Hard-soft bi-layer thin films

Consider CoPt based hard-soft bi-layer films deposited on SiO_2/Si substrates. The hard-soft bilayered structure can be produced by first depositing the bot-

Table 5.1: The boundary conditions for the two cases of magnetic two-phase materials discussed here. The domain coupling and reversibility parameters were assumed to be constant in all the cases, as it seemed to have no considerable effect on the resulting loops.

JA parameters	Case 1	Case 2
Spontaneous magnetisation	$M_{S1} < M_{S2}$	$M_{S1} > M_{S2}$
Pinning parameter	$k_1 > k_2$	$k_1 < k_2$
Domain density	$a_1 > a_2$	$a_1 < a_2$
Domain coupling	$\alpha_1 = \alpha_2$	$\alpha_1 = \alpha_2$
Reversibility parameter	$c_1 = c_2$	$c_1 = c_2$

tom CoPt layer, annealing it in high vacuum and cooling down the sample to room temperature. This produces a magnetically hard behaviour. Then the magnetically soft CoPt layer can be deposited [Alexandrakis et al., 2008]. These materials, due to the nucleation of domain walls that are pinned at the hard-soft interface, show two-phase hysteresis behaviour. This hysteresis behaviour can be modelled based on the limiting conditions that the material undergoes transition from one magnetic phase to the other during the hysteresis cycle with M_{S1}, the spontaneous magnetisation of the low field phase less than that of high field phase, M_{S2}, the pinning parameter k_1 greater than k_2, and the domain density, a_1, greater than a_2. The domain coupling, α, and reversibility, c, may be assumed to be independent of magnetic phase for simplicity. In other words, the values of parameters c and α are the same for both magnetic phases.

In this case, the parameter sets (M_{S1}, k_1, a_1) and (M_{S2}, k_2, a_2) do not represent the set of JA parameters of individual layers in the bi-layer film, but rather they are a "composite" parameter set that represent the complete bi-layer in the

low field and high field magnetic phase respectively.

The calculated hysteresis loop, shown in Fig. 5.13(a), has an excellent resemblance to the measured loop shown in Fig. 5.13(b) [Alexandrakis et al., 2008].

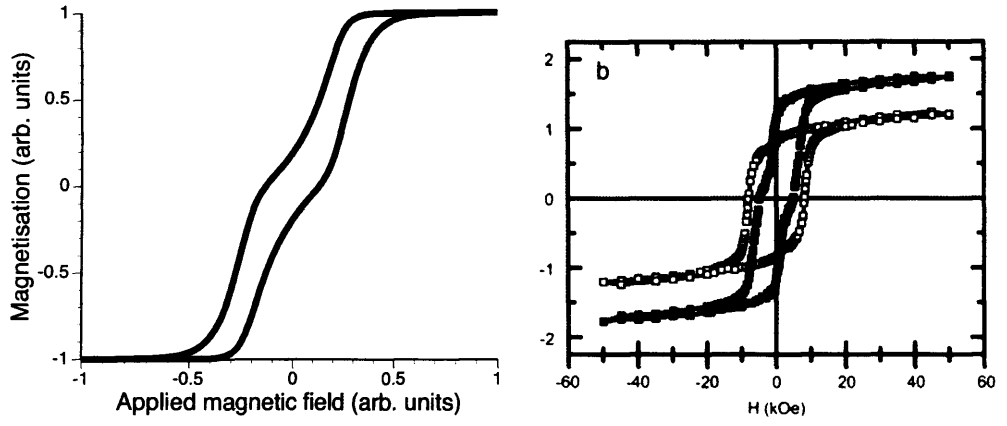

(a) (b)

Figure 5.13: (a) Two-phase hysteresis behaviour calculated using JA theory with variable hysteresis parameters. (b) The measured hysteresis behaviour of a CoPt based hard-soft bi-layer thin films on SiO_2/Si (reproduced from [Alexandrakis et al., 2008]). The hysteresis loop of single hard layer (in white squares) is given for comparison.

Similar hysteresis curves have been observed in grain-oriented silicon-iron under compressive stress, where the development of unfavourable domains and reduction in domain spacing under stress causes deformation of the hysteresis loop [Miyagi et al., 2010; Moses & Davies, 1980].

Case 2: Magnetic micro-wires

Consider the case of a two-phase behaviour with limiting conditions exactly opposite to that in Case 1, but maintaining the assumption that c and α are the same for both magnetic phases. Hence, the spontaneous magnetisation of the

low field phase, M_{S1}, is greater than that of high field phase, M_{S2}, the pinning parameter k_1 less than k_2, and the domain density a_1 less than a_2.

In this case, the parameter sets (M_{S1}, k_1, a_1) and (M_{S2}, k_2, a_2) do not represent the set of JA parameters of individual layers in the bi-layer film, but rather they are a "composite" parameter set that represent the complete bi-layer in the low field and high field magnetic phase respectively.

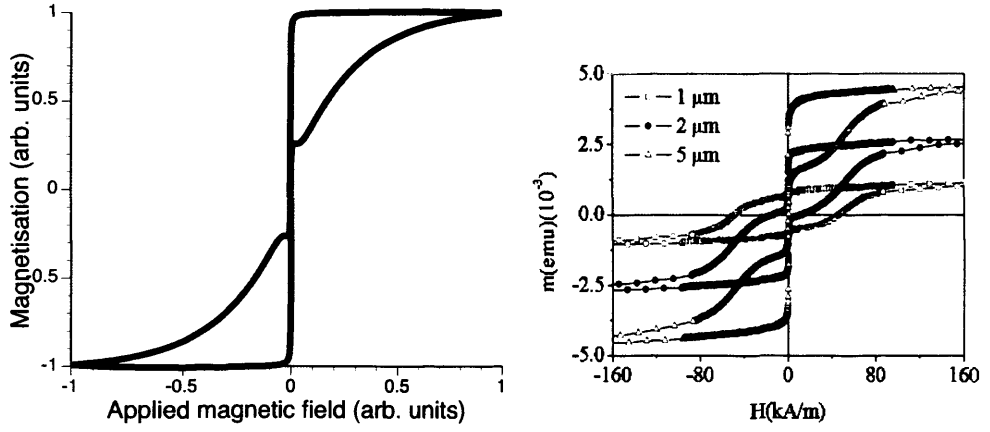

Figure 5.14: (a) Two-phase hysteresis behaviour calculated using JA theory with variable hysteresis parameters. (b) The measured hysteresis behaviour of a FePt/FeNi based magnetic micro-wires (reproduced from [Torrejon et al., 2008]).

The generated hysteresis curve under these conditions is shown in Fig. 5.14(a). This hysteresis behaviour is commonly found in magnetic micro-wires in which the magnetisation reversal of the soft outer shell occurs at lower fields whereas the reversal of the hard nucleus occurs at higher fields. The measured hysteresis loops of FePt/FeNi based hard/soft magnetic micro-wires are reported in literature [Torrejon et al., 2008] and are reproduced in Fig. 5.14(b) for comparison. As can be seen from Figs 5.14(a) and 5.14(b) that the hysteresis loops, both calculated and measured, are in excellent agreement.

In the two-phase material modelling, for better prediction of two-phase magnetic behaviour, the exchange field should be represented as a function of stress (in the case of silicon-iron) in the material. Also, the parameters c and α should be represented as functions of the exchange field rather than assuming constants. In order to understand completely the behaviour of two-phase materials, it is also necessary to model minor loops using JA theory.

5.6 Summary

- This chapter introduced the modelling aspects of magnetic hysteresis. The JA theory of hysteresis was discussed in detail. The extension of JA theory to incorporate temperature dependence of hysteresis was explained.
- The thermally dependent hysteresis model was validated against measurements made of a substituted cobalt ferrite material and was found to be in good agreement.
- The functional form of anhysteretic magnetisation that helps in modelling the influence of anisotropy effects on magnetic hysteresis in JA theory was derived. It was shown that, with necessary limiting conditions, the generalised form could be reduced to known model equations for specific cases.
- The procedure to model and predict the magnetic hysteresis behaviour of magnetic two-phase materials using JA theory was elaborated. Two different cases based on this model were discussed. It was found that

the calculated hysteresis behaviours were qualitatively in excellent agreement with those measured on hard-soft bi-layer thin film structures and micro-wires.

Chapter 6

Application of Jiles-Atherton theory to thin films

6.1 Introduction

This chapter introduces the modelling aspects of thin films based on Jiles-Atherton theory of hysteresis. Section 6.2 explains the need for a magnetic hysteresis model for thin films based on phenomenological approach. Section 6.3 gives a detailed approach to modelling of thin films using JA theory by choosing the correct anhysteretic magnetisation function. Section 6.4 elaborates the procedure to model thin films based on JA theory of hysteresis and applies the proposed model to cobalt ferrite thin films investigated in Chapter 3. The variations of microscopic JA parameters with substrate temperature and oxygen pressure are studied. The modelled and measured hysteresis loops are then compared.

6.2 Thin film hysteresis models

The first magnetic thin film was prepared by the German physicist August Kundt in the 1880s using electrochemical deposition process [Kundt, 1886]. Since then there has been a huge development in this field. The dynamics of domains and domain walls of magnetic thin films were studied and known in the early 1990s [Slonczewski, 1991a,b]. Although there were models to predict the magnetic behaviour in bulk materials, they cannot be used in their present form to predict behaviour in thin films. This is due to the kind of anisotropy, crystallographic structure, substrate induced strain, grain size, texture etc. that differentiate thin films from bulk materials and play a major role in determining the magnetic behaviour.

A theory of magnetic hysteresis for thin films developed by Slonczewski in 1960s based on Stoner-Wohlfarth model, which was previously circulated internally at IBM research, has recently been published [Slonczewski, 2009]. This model was primarily developed for thin films that approach single domain magnetic behaviour that are commonly found in small structures of iron-nickel alloy and are widely applied in the magnetic recording industry.

Micromagnetic models based on Landau-Lifshitz theory were conducted on thin films. Today micromagnetics is widely used in the modelling of spin valves, giant magnetoresistive heads and thin film media [Lee et al., 2010; Miles & Parker, 1996; Zhu & Bertram, 1988]. In micromagnetic models, thin film media were modeled as a planar hexagonal array of hexagonally shaped grains. Each grain is a single domain particle whose magnetisation reverses by coherent rotation. However, the main disadvantage of micromagnetic models

is their very large computation time as explained in Section 2.6.

Today thin films can be found in many applications ranging from magnetic recording media to solar panels. Although the properties of materials in bulk form are better for some applications, thin films attract the developing markets with the potential to produce next-generation nanoscale devices. However, growing good quality thin films to achieve desired properties is still considered as a challenge due to the influence of many deposition parameters as explained in Section 2.5.1. It is neither very easy nor inexpensive to experimentally optimise the deposition parameters for the growth of good quality thin films with desired properties for a particular application. Hence an attempt was made as a part of this research to develop a phenomenological model of magnetic hysteresis for thin films based on JA theory in order to understand the effects of deposition parameters on the properties of thin films without having to deposit and characterise large number of samples on a "try-and-test" basis.

6.3 JA model for thin films

As a part of this research work, an attempt was made to model magnetic properties of thin films using Jiles-Atherton theory of hysteresis. The JA theory is explained in detail in Chapter 5. The five parameters of the model are intrinsic properties of the material and hence are not directly influenced by the form factor of the material (bulk or thin film). One of the main parameters to be considered in thin film modelling is the anisotropy. In this work, thin film anisotropy was approximated to two-dimensional case due to their negligible

thickness and the model was assumed to have the anhysteretic magnetisation function of the form [Jiles et al., 2000]

$$M_{an} = M_S \left(\frac{\sum_{n=0}^{\infty} \frac{h^{2n+1}}{(n+1)!\,2^{2n+1}}}{1 + \sum_{n=0}^{\infty} \frac{h^{2(n+1)}}{(n+1)!\,2^{2(n+1)}}} \right) \tag{6.1}$$

where $h = \frac{H_e}{a}$, H_e is the effective field and a is the domain density.

In order to model the hysteresis loops of cobalt ferrite thin films shown in Section 3.3, the anhysterestic magnetisation of the form shown in equation (6.1) was assumed in the JA model.

6.4 Modelling procedure

In order to conceptually demonstrate the modelling of thin films based on JA theory, a simplistic approach was taken. This approach to model thin films and to understand the variations of JA parameters with deposition conditions has three steps:

1. extraction of JA parameters from measured hysteresis data of cobalt ferrite thin films deposited at various substrate temperatures and oxygen pressures,

2. construction of magnetic hysteresis loops using the extracted parameters in the JA model,

3. comparison of the measured and modelled hysteresis curves and determination of root mean square error (RMSE).

The five parameters of JA theory were extracted from the measurements using dividing rectangles (DIRECT) algorithm, an iterative optimisation technique with reliability and robustness. As the name indicates, the algorithm samples points in the domain and uses the information to decide the next search path iteratively until it converges globally to a minimal value of the objective function. A detailed explanation of the DIRECT algorithm can be found in [Perttunen et al., 1993]. The important inputs to this algorithm are

- objective function: any function that is to be minimised or maximised using optimisation algorithms. In this case, it is the solution of JA model equations (5.1)–(5.3).
- number of iterations: 1000
- global minimum: The smallest overall value of a function over its entire range. In this case, it is defined as

$$\min = \sum \left(\frac{M_{\text{model}} - M_{\text{meas}}}{M_{\text{meas}}} \right)^2 \tag{6.2}$$

  where M_{model} and M_{meas} are respectively the modelled and measured magnetisation data. This is a good approximation for the minimal value of the objective function as the modelled data is obtained by calculating the objective function.

For all the cases discussed in this Chapter, the optimised parameters were obtained after 1000 iterations at which the minimum value of the objective function reaches a value of the order of 10^{-2}.

The hysteresis loops of cobalt ferrite thin films were calculated by using the extracted parameters in the JA model equations (5.1)–(5.3) given in Chapter 5. The hysteresis model and the optimisation algorithm were coded in MATLAB. The boundaries of the five JA parameters were set as follows [Chwastek & Szczyglowski, 2007]:

M_s: $\langle 0.8{*}M_{tip}, 1.5{*}M_{tip} \rangle$

k: $\langle 0.2{*}H_c, 5{*}H_c \rangle$

a: $\langle 0.5{*}H_c, 5{*}H_c \rangle$

α: $\langle 0.7{*}H_{tip}/M_{tip}, H_{tip}/M_{tip} \rangle$

c: $\langle 0, 1 \rangle$

where, M_s is saturation magnetisation, k is pinning constant, a is domain density, α is domain coupling, c is reversibility factor, M_{tip} is the maximum value of magnetisation in the measured data, H_{tip} is the maximum value of magnetic field in the measured data and H_c is the measured coercivity.

The error between the measured and modelled hysteresis curves, a measure of reliability and robustness of the extraction procedure, was obtained by calculating RMSE as follows:

$$\mathrm{RMSE} = \sqrt{\frac{\sum_{i=1}^{n} \left(\frac{Y - y}{Y}\right)^2}{n}} \tag{6.3}$$

where Y is the measured magnetisation data, y is the modelled magnetisation data and n is the number of points. The lower the RMSE value the better the

fit between measurements and model. The RMSE value can be related to the minimum value of the objective function given in equation (6.2).

6.4.1 Thin films deposited at different substrate temperatures

The JA parameters are extracted using the DIRECT algorithm from the measured in-plane hysteresis loops of cobalt ferrite thin films deposited at different substrate temperatures shown in Fig. 3.2(a) to understand the influence of substrate temperature on microscopic parameters. Figure 6.1 shows the variation of extracted JA parameters of cobalt ferrite thin films with substrate temperature. The calculated saturation magnetisation increases with increasing substrate temperature as observed in the measurements. The domain wall pinning parameter increases with deposition temperature indicating an increase in domain wall pinning energy and/or pinning density. The domain density remains almost constant at substrate temperatures higher than 350 °C. The domain coupling, a measure of magnetic interactions between domains, decreases with increasing substrate temperature. The reversibility, a measure of domain wall bowing, is almost independent of substrate temperature.

The calculated and measured saturation magnetisation and coercivity are in very good agreement. The hysteresis loops calculated using the extracted parameters of the JA model are plotted against the measured loops for comparison and are given in Fig. 6.2. As can be seen from the figure, the modelled and measured hysteresis loops are in excellent agreement.

The RMSE increases with increasing substrate temperature indicating that the model deviates more from the measurements at higher substrate temper-

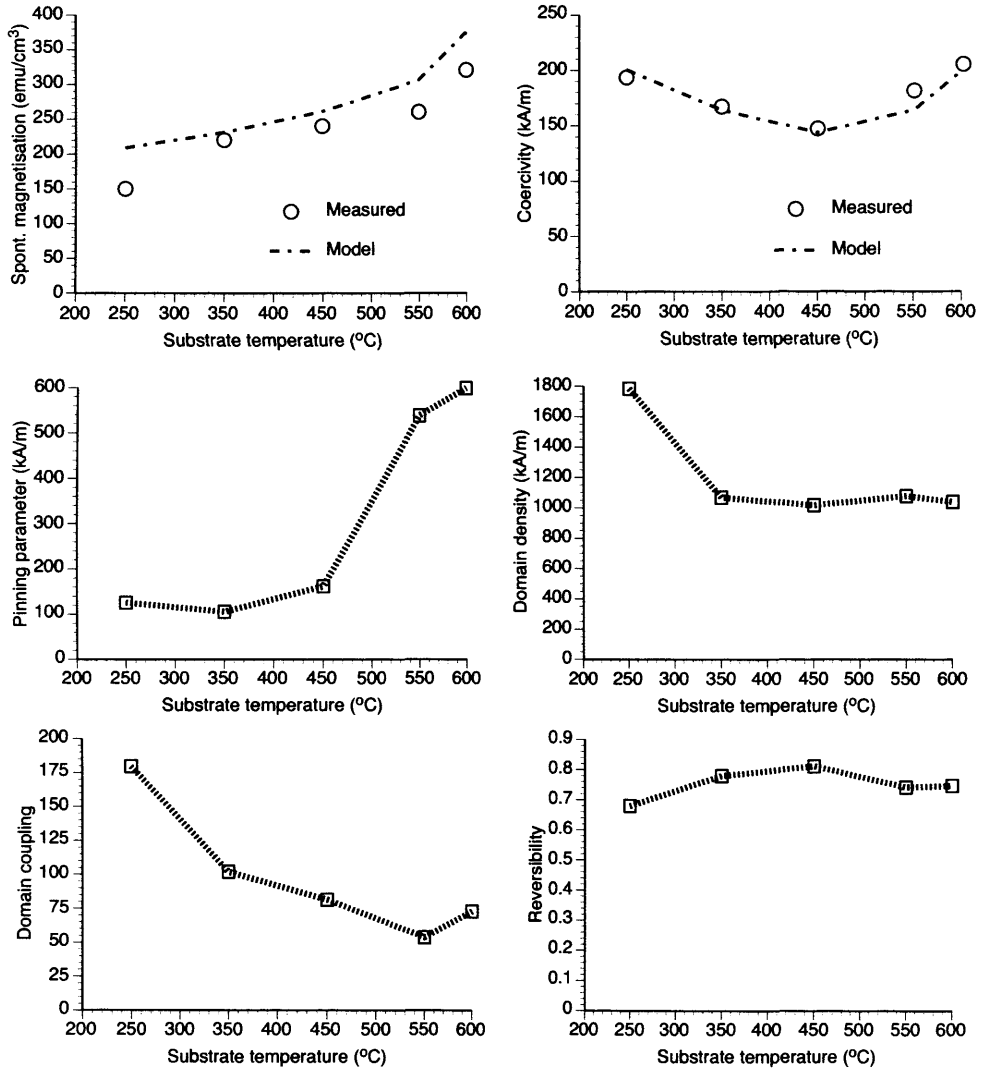

Figure 6.1: The variation of calculated JA parameters of cobalt ferrite thin films with substrate temperature.

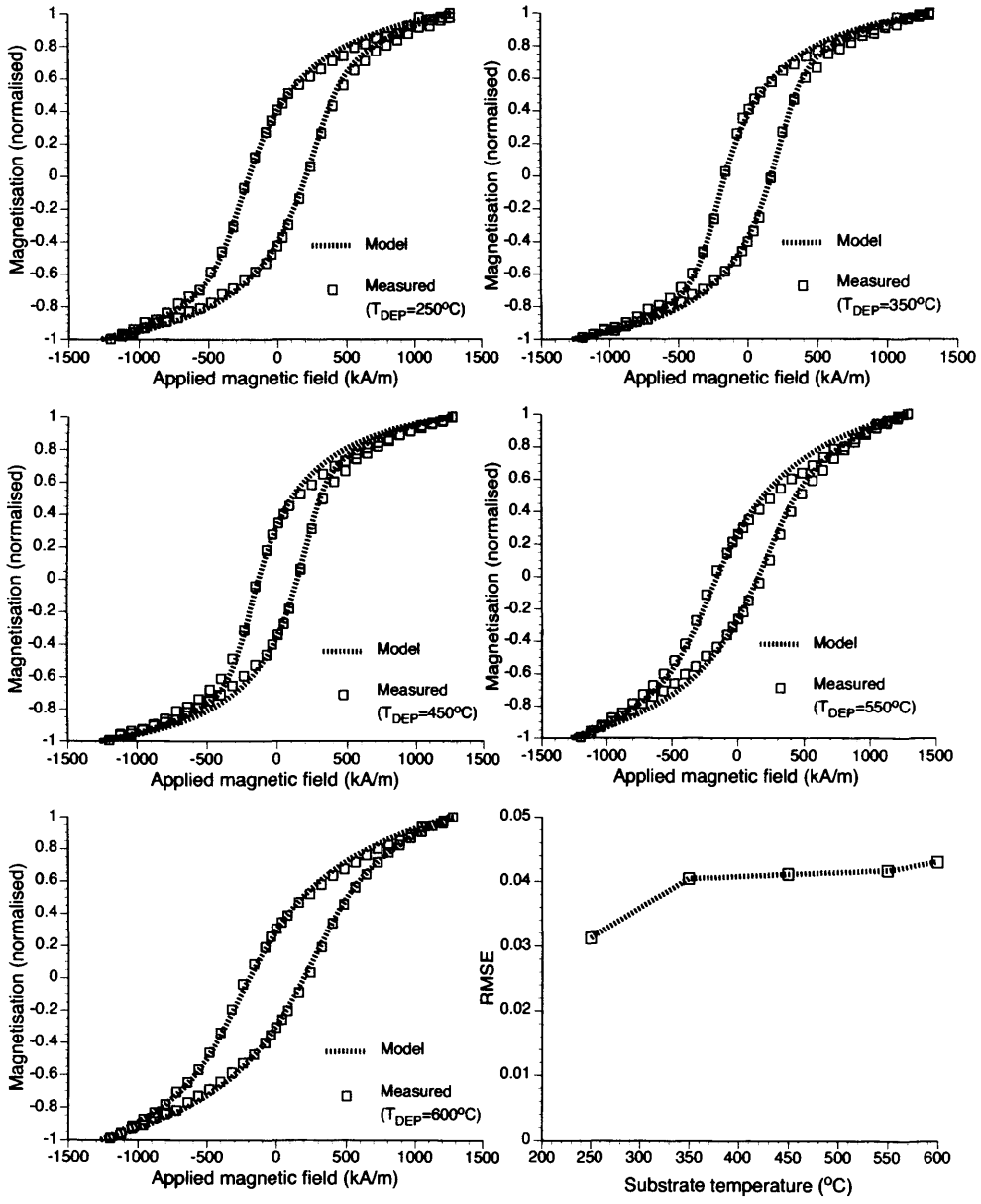

Figure 6.2: Comparison between measured in-plane hysteresis loops of cobalt ferrite thin films deposited at different substrate temperatures and calculated loops based on the JA model.

ature. It is already explained in Section 3.3.1 and also shown in Fig. 3.4 that there is a substantial amount of strain on the film at higher substrate temperatures due to thermal expansion mismatch between the film and substrate. But the JA model assumes the ideal case where there is no thermal expansion mismatch. This is probably the reason for deviation of the model predictions from measurements at higher substrate temperatures.

6.4.2 Thin films deposited at different oxygen pressures

In order to understand the effect of reactive oxygen pressure on microscopic parameters, the in-plane hysteresis loops of cobalt ferrite thin films deposited at various oxygen pressures were modelled using the procedure explained above. The JA parameters were extracted from the measured loops and are plotted against the reactive oxygen pressure and are shown in Fig. 6.3.

The variation of saturation magnetisation with oxygen pressure does not show a monotonic trend. This behaviour can be attributed to the oxygen deficiency, and formation of mixed phase films at lower (5 mTorr and 15 mTorr) and higher oxygen pressures (50 mTorr). The pinning parameter, although seems to be constant at lower oxygen pressures, increases at higher oxygen pressures. The domain density decreases with increasing oxygen pressures whereas the domain coupling increases with oxygen pressure until ~22 mTorr and then decreases. The measured and modelled values of saturation magnetisation and coercivity are in good agreement.

It is worth noting that the range of oxygen pressure for optimised growth of single phase cobalt ferrite thin films at lower substrate temperature is approx-

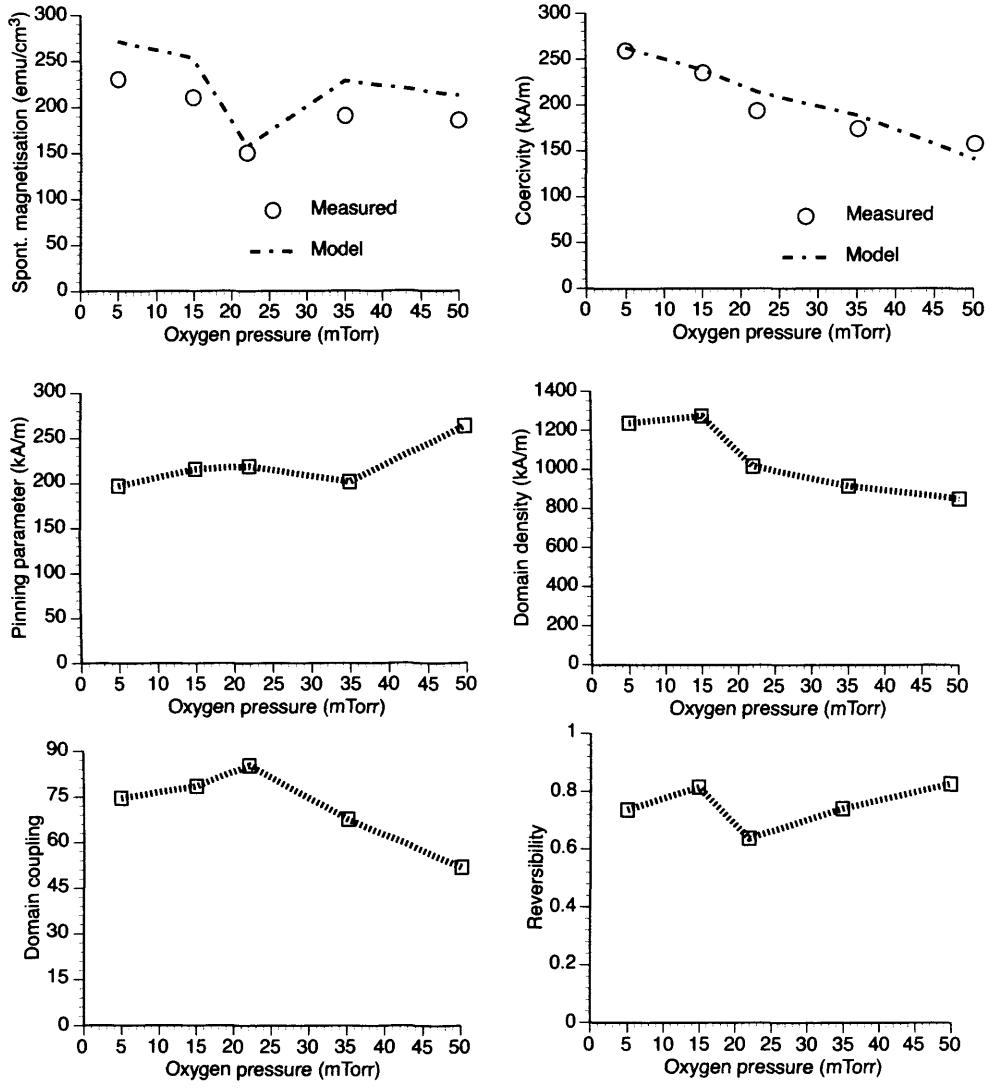

Figure 6.3: The variation of calculated JA parameters of cobalt ferrite thin films with reactive oxygen pressure.

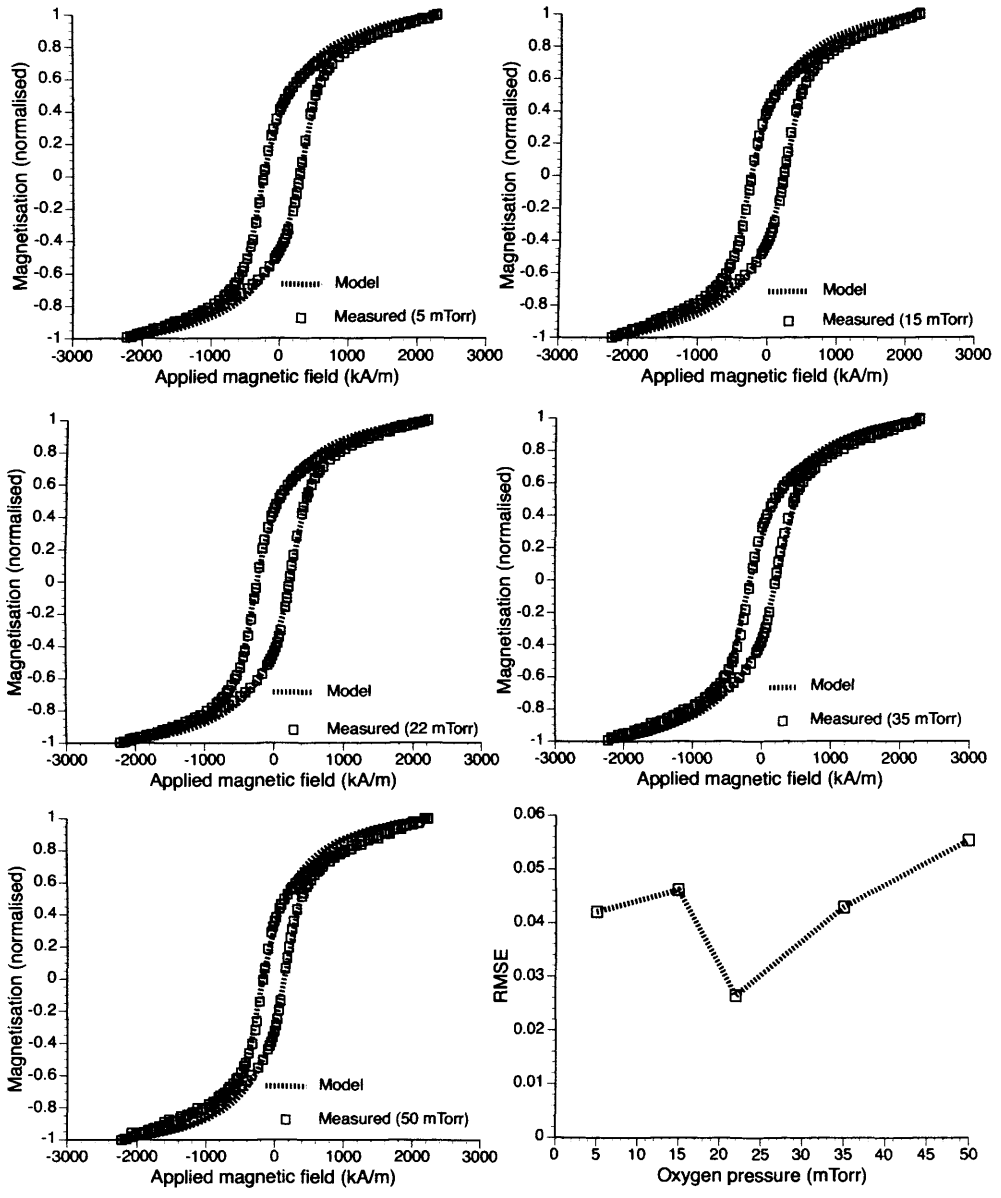

Figure 6.4: Comparison between measured in-plane hysteresis loops of cobalt ferrite thin films deposited at different oxygen pressures and calculated loops based on the JA model.

imately between 20 mTorr and 40 mTorr. Hence these irregular trends in the microscopic parameters versus oxygen pressures can be attributed to the presence of mixed phases in the films particularly at the higher and lower substrate temperatures.

The comparison of modelled hysteresis loops against the measurements made on cobalt ferrite thin films deposited at different oxygen pressures is shown in Fig. 6.4. It is evident that the thin film JA model is in excellent agreement with measurements.

The RMSE is low for the sample deposited at 22 mTorr which is single phase indicating that the deviation between the measurement and model is low. For samples deposited at lower and higher oxygen pressures, the deviation is higher. This maybe due to the inherent assumption of the JA model that the samples are single phase.

6.5 Summary

- The modelling aspects of thin films based on JA theory of hysteresis were discussed.
- The anhysteretic magnetisation function for planar anisotropy materials was used to model thin films using JA theory.
- The proposed model was applied to cobalt ferrite thin films investigated in Chapter 3.
- The JA parameters were extracted from measured data using the DIRECT optimisation algorithm.

- The variations of JA parameters with substrate temperature and oxygen pressure were studied. The modelled and measured hysteresis loops were found to be in excellent agreement.
- This model can be further improved by
  - considering thermal expansion coefficients and lattice constants of film and substrate in the model which would help incorporate strain due to thermal expansion and lattice mismatches.
  - modelling mixed phase compositions in thin films
  - modelling minor loops accurately using JA theory of hysteresis.

Chapter 7

Conclusions and future work

7.1 Conclusions

Magnetoelastic and magnetocaloric thin films were grown using the pulsed-laser deposition technique. The structural, microstructural and magnetic properties of these thin films were characterised using established procedures. Novel thin film growth techniques and characterisation procedures were developed, where necessary.

Many valuable additions have been made (including an application to thin films) to the Jiles-Atherton model, a well-established model of hysteresis. The thin film model of Jiles-Atherton theory was validated against measurements made on magnetoelastic thin films grown as part of this research work.

The thoroughly investigated findings and thereby derived conclusions from this extensive research work and recommendations for the future work are listed below:

7.2 Magnetoelastic thin films

- Magnetoelastic thin films based on cobalt ferrite were produced on SiO_2/Si(100) substrates using pulsed-laser deposition technique at various deposition conditions.
- The influence of deposition parameters: substrate temperature and oxygen pressure, on the magnetic properties and crystal structure of cobalt ferrite thin films was studied.
- The growth process of cobalt ferrite thin films was optimised for low substrate temperature.
- It was found that there is only a narrow window of reactive oxygen pressure for the growth of single phase spinel crystalline cobalt ferrite thin films at low substrate temperatures.
- Cobalt ferrite films grown at low substrate temperature and optimised oxygen pressure on thermal expansion matched substrates can be applied in multilayer sensors on micro electro mechanical systems (MEMS) devices.
- In-plane uniaxial anisotropy was induced by means of magnetic annealing in the optimised cobalt ferrite thin film.
- A 3-point bender was designed to measure magnetostriction in thin films in the vibrating sample magnetometer based on the inverse measurement technique.

- Using this 3-point bender, saturation magnetostriction was measured on the magnetically annealed polycrystalline cobalt ferrite thin film. The measured value of magnetostriction in thin films was found to reach the upper end of the range of bulk values of cobalt ferrite reported in the literature. This indicates that cobalt ferrite thin films can be used as magnetostrictive sensors and actuators.

7.2.1 Future work

Although research has been carried out on cobalt ferrite materials by several research groups around the world, the applications developed based on this material are few. Hence future work may focus on developing applications by exploiting magnetic, magnetoelastic and related properties of this material.

- The growth of cobalt ferrite thin films can be optimised further based on other deposition parameters such as deposition rate, laser fluence and laser repetition rate in order to achieve higher saturation magnetisation and softer magnetic properties (low coercivity).

- Cobalt ferrite thin films can be grown on thermal expansion matched substrates allowing wider range of substrate temperatures to be used for optimisation.

- Cation substituted cobalt ferrite thin films can be grown on thermal expansion matched substrates.

- The process of magnetic annealing of cobalt ferrite thin films can be optimised.

- The optimised cobalt ferrite thin films may be grown on piezoelectric substrates such as (Ba, Sr)TiO_3 or some other piezoelectric oxides. These thin film structures have potential in magnetoelectric sensor and high frequency device applications due to their strong magnetoelectric coupling.
- As the findings of this research work demonstrate, single phase crystalline spinel cobalt ferrite thin films can be produced at low substrate temperatures, these thin films can be grown on flexible substrates. This structure, cobalt ferrite thin film on flexible substrates, can be applied as non-contact strain sensor.

7.2.2 Magnetocaloric thin films

- The first successful thin film of $Gd_5Si_{2.08}Ge_{1.92}$ was grown on polycrystalline AlN substrate using pulsed-laser deposition technique.
- The crystallographic structure, composition, grain size and magnetic properties were studied.
- It was found that the film was predominantly monoclinic. There was no evidence of a substantial amount of secondary phases found in the film.
- The magnetic phase transformation near room temperature was determined in the magnetisation versus temperature study.
- This property indicates the potential for this thin film to be used in micro-cooling applications.

7.2.3 Future work

Since this is the first known reported successful growth of $Gd_5Si_2Ge_2$ thin film, there is a wide scope for research. The growth process of $Gd_5Si_2Ge_2$ thin films may be optimised with the goal to produce first order magnetic/structural phase transition temperature in the region of interest. Future research on $Gd_5Si_2Ge_2$ thin films with a focus on developing a prototype may help conserve energy in refrigeration applications. Although it is too early to give the approximate efficiency of these thin films in refrigeration applications, it was found that bulk $Gd_5Si_2Ge_2$ have 60% Carnot efficiency, which is twice than liquid-vapour cycle refrigeration. As $Gd_5Si_2Ge_2$ also has a giant magnetostrain, films of this material, especially highly oriented films, could be used for actuator or sensor applications.

7.3 Modelling

- The Jiles-Atherton theory was extended to incorporate temperature dependence of hysteresis.
- The proposed thermal dependence was validated against measurements made of a substituted cobalt ferrite material and the results were found to be in excellent agreement.
- A generalised functional form of anhysteretic magnetisation which is the basis of Jiles-Atherton theory was derived.
- It was shown that, with necessary limiting conditions, the generalised

form could be reduced to known model equations for specific cases such as uni-axially anisotropic, planar anisotropic and isotropic.

- A procedure to model and predict the magnetic hysteresis behaviour of two-phase magnetic materials using Jiles-Atherton theory was developed.
- The calculated magnetic two-phase hysteresis behaviours were qualitatively in excellent agreement with those measured on hard-soft bi-layer thin film structures and micro-wires.
- The Jiles-Atherton theory of hysteresis was extended for thin films.
- The thin film model based on Jiles-Atherton theory was validated against measurements made on cobalt ferrite thin films and was found to be in excellent agreement.

7.3.1 Future work

The Jiles-Atherton theory is being developed continuously since it was first proposed in 1986. There is nonetheless considerable scope for future research on this model. A few recommendations arise out of this research work are as follows:

- thermal expansion coefficients and lattice constants of film and substrate may be incorporated into the model in order to analyse the effects of strain due to thermal expansion and lattice mismatches on magnetic properties of materials,

- modelling of mixed phase compositions in thin films
- accurate modelling of minor loops.

Appendix A

Derivation of anhysteretic magnetisation (uniaxial anisotropy)

$$M_{an} = M_s \frac{\int_0^{2\pi}\int_0^{\pi} \exp\left(h\cos\theta - \kappa[1-\cos^2\theta]\right)\sin\theta\cos\theta\, d\theta\, d\varphi}{\int_0^{2\pi}\int_0^{\pi} \exp\left(h\cos\theta - \kappa[1-\cos^2\theta]\right)\sin\theta\, d\theta\, d\varphi} \tag{A.1}$$

On integration w.r.t φ,

$$M_{an} = M_s \frac{\int_0^{\pi} \exp\left(h\cos\theta - \kappa[1-\cos^2\theta]\right)\sin\theta\cos\theta\, d\theta}{\int_0^{\pi} \exp\left(h\cos\theta - \kappa[1-\cos^2\theta]\right)\sin\theta\, d\theta} \tag{A.2}$$

Substituting $x = \cos\theta$ and $dx = -\sin\theta\, d\theta$ in equation (A.2) we get,

$$M_{an} = M_s \frac{\int_{-1}^{1} \exp\left(hx - \kappa[1 - x^2]\right) x\, dx}{\int_{-1}^{1} \exp\left(hx - \kappa[1 - x^2]\right)\, dx} \tag{A.3}$$

$$= M_s \frac{\int_{-1}^{1} \exp\left(\kappa x^2 + hx - \kappa\right) x\, dx}{\int_{-1}^{1} \exp\left(\kappa x^2 + hx - \kappa\right) x\, dx} \tag{A.4}$$

Rearranging and cancelling the common terms,

$$M_{an} = M_s \frac{\int_{-1}^{1} \exp\left(\left[\sqrt{\kappa}x + \frac{h}{2\sqrt{\kappa}}\right]^2 - \left[\kappa + \frac{h^2}{4\kappa}\right]\right) x\, dx}{\int_{-1}^{1} \exp\left(\left[\sqrt{\kappa}x + \frac{h}{2\sqrt{\kappa}}\right]^2 - \left[\kappa + \frac{h^2}{4\kappa}\right]\right) dx} \tag{A.5}$$

$$= M_s \frac{\int_{-1}^{1} \exp\left(\left[\sqrt{\kappa}x + \frac{h}{2\sqrt{\kappa}}\right]^2\right) x\, dx}{\int_{-1}^{1} \exp\left(\left[\sqrt{\kappa}x + \frac{h}{2\sqrt{\kappa}}\right]^2\right) dx} \tag{A.6}$$

Let $y = \sqrt{\kappa}x + \frac{h}{2\sqrt{\kappa}}$; $dy = \sqrt{\kappa}\, dx$ and the limits $y_1 = -\sqrt{\kappa} + \frac{h}{2\sqrt{\kappa}}$; $y_2 = \sqrt{\kappa} + \frac{h}{2\sqrt{\kappa}}$

$$M_{an} = M_s \frac{\int_{y_1}^{y_2} \exp(y^2)\left(y - \frac{h}{2\sqrt{\kappa}}\right) dy}{\int_{y_1}^{y_2} \exp(y^2)\, dy} \tag{A.7}$$

Splitting the limits of integrals,

$$M_{an} = M_s \frac{\int_{y_1}^{y_2} \exp(y^2)\, y\, dy - \frac{h}{2\sqrt{\kappa}} \left[\int_0^{y_2} \exp(y^2)\, dy - \int_0^{y_1} \exp(y^2)\, dy \right]}{\int_0^{y_2} \exp(y^2)\, dy - \int_0^{y_1} \exp(y^2)\, dy} \tag{A.8}$$

On integrating the first term in the numerator,

$$M_{an} = M_s \frac{\left[\frac{\exp(y^2)}{2} \right]_{y_1}^{y_2} - \frac{h}{2\sqrt{\kappa}} \left[\int_0^{y_2} \exp(y^2)\, dy - \int_0^{y_1} \exp(y^2)\, dy \right]}{\int_0^{y_2} \exp(y^2)\, dy - \int_0^{y_1} \exp(y^2)\, dy} \tag{A.9}$$

Substituting the definition of Dawson's integral shown in equation (A.10) and rearranging we get equation (A.11)

$$F(z) = \exp(-z^2) \int_0^z \exp(t^2) dt \tag{A.10}$$

$$M_{an} = M_s \frac{\left[\exp(2h) - 1 \right] \sqrt{\kappa} + hF\left(\frac{h - 2\kappa}{2\sqrt{\kappa}} \right) - \exp(2h) hF\left(\frac{h + 2\kappa}{2\sqrt{\kappa}} \right) \Big]}{2\kappa \left[-F\left(\frac{h - 2\kappa}{2\sqrt{\kappa}} \right) + \exp(2h) F\left(\frac{h + 2\kappa}{2\sqrt{\kappa}} \right) \right]} \tag{A.11}$$

Appendix B

Validation of specific cases

B.1 Axial anisotropy case

From the asymptotic expansion of Dawson's integral [Bender & Orszag, 1978], for large $|z|$, the function $F(z) \approx \frac{1}{2z}$.

Applying the above boundary condition in equation (5.25),

$$
\begin{aligned}
M_{an} &= \lim_{\kappa \to \infty} M_s \frac{\left[[\exp(2h)-1]\sqrt{\kappa} + h\left(\frac{\sqrt{\kappa}}{h-2\kappa}\right) - \exp(2h)h\left(\frac{\sqrt{\kappa}}{h+2\kappa}\right)\right]}{2\kappa\left[-\left(\frac{\sqrt{\kappa}}{h-2\kappa}\right) + \exp(2h)\left(\frac{\sqrt{\kappa}}{h+2\kappa}\right)\right]} \\
&= \lim_{\kappa \to \infty} M_s \frac{\left[[\exp(2h)-1]\sqrt{\kappa} + \frac{h\sqrt{\kappa}}{h^2-4\kappa^2}\left(h(1-\exp(2h)) + 2\kappa(1+\exp(2h))\right)\right]}{\left[\frac{2\kappa^{3/2}}{h^2-4\kappa^2}\left(h(\exp(2h)-1) - 2\kappa(\exp(2h)+1)\right)\right]}
\end{aligned}
$$

Neglecting higher order terms, rearranging and applying limits we get equation (5.26).

B.2 Planar anisotropy case

Rearranging equation (5.27) and applying trigonometric identities in order to integrate w.r.t φ we get,

$$M_{an} = M_s \frac{\int_0^{\pi} \exp\left(h\cos\theta - \frac{\kappa}{4}(3+\cos 2\theta)\right) \sin 2\theta \left[\int_0^{2\pi} \exp\left(\frac{\kappa}{2}\sin^2\theta\cos 2\varphi\right) d\varphi\right] d\theta}{2\int_0^{\pi} \exp\left(h\cos\theta - \frac{\kappa}{4}(3+\cos 2\theta)\right) \sin\theta \left[\int_0^{2\pi} \exp\left(\frac{\kappa}{2}\sin^2\theta\cos 2\varphi\right) d\varphi\right] d\theta}$$

To evaluate the integral with respect to φ, Sonine's expansion for modified Bessel function was used [Bender & Orszag, 1978; Jiles et al., 2000].

$$\exp(y\cos\varphi) = I_0(y) + 2\sum_{p=1}^{\infty} I_p(y)\cos(p\varphi) \tag{B.1}$$

where $I_0(y)$ is the modified Bessel function of first kind. As the contributions of higher order ($p \neq 0$) Bessel functions to equation (B.1) are negligible [Jiles et al., 2000], only the first order Bessel function is considered. Substituting equation (B.1) into equation (B.2) and integrating with respect to φ will yield equation (5.28).

Appendix C

List of Publications

C.1 Peer reviewed journals

1. *Influence of reactive atmosphere on properties of cobalt ferrite thin films prepared using pulsed-laser deposition*, Journal of Applied Physics (under review).

2. *Modeling of two-phase magnetic materials based on Jiles-Atherton theory of hysteresis*, Journal of Magnetism and Magnetic Materials (2010) (under review)

3. *Growth of crystalline cobalt ferrite thin films at lower temperatures using pulsed-laser deposition technique*, Journal of Applied Physics 107, 09A516 (2010).

4. *Theoretical model of temperature dependence of hysteresis based on mean field theory*, IEEE Transactions on Magnetics 46 (6), 5467478 (2010).

5. *Generalized form of anhysteretic magnetization in Jiles-Atherton theory of hysteresis*, Applied Physics Letters 95 (17), 172510 (2009).

6. *Modeling the temperature dependence of hysteresis based on Jiles-Atherton theory of hysteresis*, IEEE Transactions on Magnetics 45 (10), 5257370 (2009).

7. *Comparison of alternative techniques in characterizing magnetostriction and inverse magnetostriction in magnetic thin films*, IEEE Transactions on Magnetics 45 (9), 5208521 (2009).

C.2 Conference presentations

1. 55^{th} Magnetism and Magnetic Materials Conference, Atlanta, Georgia, 14-18 Nov. 2010 (accepted for presentation).

2. The Joint European Magnetic Symposia, Krakow, Poland, 23-28 Aug. 2010.

3. APS March Meeting, Portland, Oregon, 15-19 March 2010.

4. 11^{th} Joint MMMIntermag Conference, Washington, DC, 18-22 Jan. 2010.

5. 19^{th} Soft Magnetic Materials Conference, Torino, Italy, 6-9 Sep. 2009.

6. The IEEE International Magnetics Conference, Sacramento, CA, 4-8 May 2009.

7. 53^{rd} Magnetism and Magnetic Materials Conference, Austin, Texas, 10-14 Nov. 2008.

8. 1& 2DM Conference, Cardiff, 1-3 Sep. 2008.

9. Speaking of Science-2008 Conference, Cardiff, April 2008.

Bibliography

Alexandrakis, V., Niarchos, D., Tsiaoussis, I., & Panagiotopoulos, I. (2008). Magnetization reversal in CoPt-based hard-soft homocomposites. Journal of Magnetism and Magnetic Materials, 320, 1020–1025.

Alexandrakis, V., Niarchos, D., Wolff, M., & Panagiotopoulos, I. (2009). Magnetization reversal in CoPt(111) hard/soft bilayers. Journal of Applied Physics, 105, 063908.

Andrei, P., Stancu, A., Hauser, H., & Fulmek, P. (2007). Temperature, stress, and rate dependent numerical implementation of magnetization processes in phenomenological models. Journal of Optoelectronics and Advanced Materials, 9, 1137–1139.

Arrott, A. & Noakes, J. E. (1967). Approximate equation of state for nickel near its critical temperature. Physical Review Letters, 19, 786–789.

Auciello, O., Krauss, A. R., Santiago-Aviles, J., Schreiner, A. F., & Gruen, D. M. (1988). Surface compositional and topographical changes resulting from excimer laser impacting on $YBa_2Cu_3O_7$ single phase superconductors. Applied Physics Letters, 52, 239–241.

Belov, K. P., Goryaga, A. N., & Lyamzin, A. N. (1989). Anomalous magnetic properties of $CoFe_2O_4$ ferrite. Soviet Phys. Solid State, 31, 191.

Bender, C. M. & Orszag, S. A. (1978). Advanced Mathematical Methods for Scientists and Engineers. (McGraw-Hill (New York)).

Benford, S. M. (1979). The magnetocaloric effect in dysprosium. Journal of Applied Physics, 50, 1868–1870.

Bertotti, G. (1998). Hysteresis in Magnetism. (New York: Academic Press).

Birnbaum, M. (1965). Semiconductor surface damage produced by Ruby lasers. Journal of Applied Physics, 36, 3688–3689.

Blank, D. H. A., Ijsselsteijn, R. P. J., Out, P. G., Kuiper, H. J. H., Flokstra, J., & Rogalla, H. (1992). High Tc thin films prepared by laser ablation: material distribution and droplet problem. Materials Science and Engineering B, 13, 67–74.

Bozorth, R. M. (1951). Ferromagnetism. (Princeton, NJ: D. Van Nostrand Company Inc.).

Bozorth, R. M., Tilden, E. F., & Williams, A. J. (1955). Anisotropy and magnetostriction of some ferrites. Physical Review, 99, 1788–1798.

Bragg, W. L. (1920). Crystal structure. Nature, 105, 646–648.

Chen, X. Y., Xiong, S. B., Sha, Z. S., & Liu, Z. G. (1997). The interaction of ambient background gas with a plume formed in pulsed laser deposition. Applied Surface Science, 115, 279–284.

Chikazumi, S. (1984). Physics of Magnetism. (New York: John Wiley and Sons).

Chikazumi, S. (1997). Physics of Ferromagnetism. (USA: Oxford University Press), 2nd edn.

Choe, G. & Megdal, B. (1999). High precision magnetostriction measurement employing the B-H looper bending method. IEEE Transactions on Magnetics, 35, 3959–3961.

Chrisey, D. B. & Hubler, G. K. eds. (1994). Pulsed laser deposition of thin films. (New York: John Wiley and Sons).

Chwastek, K. (2008). Frequency behaviour of the modified jiles-atherton model. Physica B: Condensed Matter, 403, 2484–2487.

Chwastek, K. (2009). Modelling of dynamic hysteresis loops using the Jiles-Atherton approach. Mathematical and Computer Modelling of Dynamical Systems, 15, 95–105.

Chwastek, K. & Szczyglowski, J. (2007). An alternative method to estimate the parameters of Jiles-Atherton model. Journal of Magnetism and Magnetic Materials, 314, 47–51.

Cullity, B. D. & Graham, C. D. (2009). Introduction to Magnetic Materials. (New Jersey: John Wiley and Sons), 2nd edn.

Dan'kov, S. Y., Tishin, A. M., Pecharsky, V. K., & Gschneidner Jr., K. A. (1998). Magnetic phase transitions and the magnetothermal properties of gadolinium. Physical Review B - Condensed Matter and Materials Physics, 57, 3478–3490.

Debye, P. (1926). Einige bemerkungen zur magnetisierung bei tiefer temperatur. Annalen der Physik, 386, 1154–1160.

Dorsey, P. C., Lubitz, P., Chrisey, D. B., & Horwitz, J. S. (1996). $CoFe_2O_4$ thin films grown on (100) MgO substrates using pulsed laser deposition. Journal of Applied Physics, 79, 6338–6340.

du Tremolet de Lacheisserie, E. (1993). Magnetostriction: Theory and Applications of Magnetoelasticity. (Boca Raton: CRC Press).

Dyer, P. E., Issa, A., & Key, P. H. (1990). An investigation of laser ablation and deposition of Y-Ba-Cu-O in an oxygen environment. Applied Surface Science, 46, 89–95.

Dyer, P. E., Key, P. H., & Monk, P. (1992). Ablation studies of Y-Ba-Cu-oxide in oxygen using a pulsed CO_2 laser. Applied Surface Science, 54, 160–165.

Ewing, J. A. (1900). Magnetic induction in iron and other metals. The electrician series. (London: The electrician printing and publishing company), 3rd edn.

Ewing, J. A. (1930). Ferromagnetism and hysteresis. Proceedings of the Physical Society, 42, 355–357.

Foltyn, S. R., Dye, R. C., Ott, K. C., Peterson, E., Hubbard, K. M., Hutchinson, W., Muenchausen, R. E., Estler, R. C., & Wu, X. D. (1991). Target modification in the excimer laser deposition of $YBa_2Cu_3O_{7-x}$ thin films. Applied Physics Letters, 59, 594–596.

Foner, S. (1959). Versatile and sensitive vibrating-sample magnetometer. Review of Scientific Instruments, 30, 548–557.

Foote, M. C., Jones, B. B., Hunt, B. D., Barner, J. B., Vasquez, R. P., & Bajuk, L. J. (1992). Composition variations in pulsed-laser-deposited Y-Ba-Cu-O thin films as a function of deposition parameters. Physica C: Superconductivity and its applications, 201, 176–182.

Geohegan, D. B. (1992). Fast intensified-ccd photography of $YBa_2Cu_3O_{7-x}$ laser ablation in vacuum and ambient oxygen. Applied Physics Letters, 60, 2732–2734.

Giauque, W. F. (1927). A thermodynamic treatment of certain magnetic effects. a proposed method of producing temperatures considerably below 1 absolute. Journal of the American Chemical Society, 49, 1864–1870.

Gorbunov, A. A. & Konov, V. I. (1991). Carbon films deposited from UV laser plasma. Surface and Coatings Technology, 47, 503–508.

Gumen, N. M. (1966). Variations of magnetostriction in heat-treated cobalt-ferrite. Soviet Phys. J. E. T. P., 22, 251.

Hadimani, R. L. (2010). Advanced magnetoelastic and magnetocaloric materials for device applications. Ph.D. thesis, Cardiff University.

Hauschild, J., Fritzsche, H., Bonn, S., & Liu, Y. (2002). Determination of the temperature dependence of the coercivity in Fe/Cr (110) multilayers. Applied Physics A: Materials Science and Processing, 74, S1541–S1543.

Hiratsuka, N., Nozawa, M., & Kakizaki, K. (1997). Magnetic properties of cobalt ferrite films with perpendicular magnetic anisotropy. Journal of Magnetism and Magnetic Materials, 176, 31–35.

Hu, G., Harris, V. G., & Suzuki, Y. (2001). Microstructure and magnetic properties of cobalt ferrite thin films. IEEE Transactions on Magnetics, 37, 2347–2349.

Hubert, A. & Schafer, R. (1998). Magnetic domains. (New York: Springer).

Jiles, D. C. (1991). Introduction to Magnetism and Magnetic Materials. (London: Chapman and Hall).

Jiles, D. C. (1993). Frequency dependence of hysteresis curves in 'non-conducting' magnetic materials. IEEE Transactions on Magnetics, 29, 3490–3492.

Jiles, D. C. (1994a). Frequency dependence of hysteresis curves in conducting magnetic materials. Journal of Applied Physics, 76, 5849–5855.

Jiles, D. C. (1994b). Modelling the effects of eddy current losses on frequency dependent hysteresis in electrically conducting media. IEEE Transactions on Magnetics, 30, 4326–4328.

Jiles, D. C. & Atherton, D. L. (1984). Theory of the magnetisation process in ferromagnets and its application to the magnetomechanical effect. Journal of Physics D: Applied Physics, 17, 1265–1281.

Jiles, D. C. & Atherton, D. L. (1986). Theory of ferromagnetic hysteresis. Journal of Magnetism and Magnetic Materials, 61, 48–60.

Jiles, D. C., Lee, S. J., Kenkel, J., & Metlov, K. L. (2000). Superparamagnetic magnetization equation in two dimensions. Applied Physics Letters, 77, 1029–1031.

Jiles, D. C., Ramesh, A., Shi, Y., & Fang, X. (1997). Application of the anisotropic extension of the theory of hysteresis to the magnetization curves of crystalline and textured magnetic materials. IEEE Transactions on Magnetics, 33, 3961–3963.

Jiles, D. C. & Thoelke, J. B. (1989). Theory of ferromagnetic hysteresis: Determination of model parameters from experimental hysteresis loops. IEEE Transactions on Magnetics, 25, 3928–3930.

Jiles, D. C., Thoelke, J. B., & Devine, M. K. (1992). Numerical determination of hysteresis parameters for the modeling of magnetic properties using the theory of ferromagnetic hysteresis. IEEE Transactions on Magnetics, 28, 27–35.

Joule, J. P. (1842). On a new class of magnetic forces. Sturgeon's Annals of Electricity, 8, 219.

Kato, Y. & Takei, T. (1933). Permanent oxide magnet and its characteristics. The Journal of the Institute of Electrical Engineers of Japan, 53, 408–412.

Kautek, W., Roas, B., & Schultz, L. (1990). Formation of YBaCu oxide thin films by pulsed laser deposition: A comparative study in the UV, visible and IR range. Thin Solid Films, 191, 317–334.

Koch, R. (1994). The intrinsic stress of polycrystalline and epitaxial thin metal films. Journal of Physics: Condensed Matter, 6, 9519–9550.

Koren, G., Gupta, A., Baseman, R. J., Lutwyche, M. I., & Laibowitz, R. B. (1989). Laser wavelength dependent properties of $YBa_2Cu_3O_{7-\delta}$ thin films deposited by laser ablation. Applied Physics Letters, 55, 2450–2452.

Krajnovich, D. J. & Vázquez, J. E. (1993). Formation of intrinsic surface defects during 248 nm photoablation of polyimide. Journal of Applied Physics, 73, 3001–3008.

Kundt, A. (1886). Ueber doppelbrechung des lichtes in metallschichten, welche durch zerstuben einer kathode hergestellt sind. Annalen der Physik, 263, 59–71.

Landau, L. D. & Lifshitz, E. M. (1935). On the theory of the dispersion of magnetic permeability in ferromagnetic bodies. Physik. Z. Sowjetunion, 8, 153–169.

Lee, J., Fuger, M., Fidler, J., Suess, D., Schrefl, T., & Shimizu, O. (2010). Modeling of the write and read back performances of hexagonal Ba-ferrite particulate media for high density tape recording. Journal of Magnetism and Magnetic Materials, 322, 3869–3875.

Liorzou, F., Phelps, B., & Atherton, D. L. (2000). Macroscopic models of magnetization. IEEE Transactions on Magnetics, 36, 418–428.

Lo, C. C. H., Ring, A. P., Snyder, J. E., & Jiles, D. C. (2005). Improvement of

magnetomechancial properties of cobalt ferrite by magnetic annealing. IEEE Transactions on Magnetics, 41, 3676–3678.

Margulies, D. T., Parker, F. T., Spada, F. E., Goldman, R. S., Li, J., Sinclair, R., & Berkowitz, A. E. (1996). Anomalous moment and anisotropy behavior in Fe_3O_4 films. Physical Review B - Condensed Matter and Materials Physics, 53, 9175–9187.

Matsunawa, A., Katayama, S., Susuki, A., & Ariyasu, T. (1986). Laser production of metallic ultra-fine particles. Transactions of JWRI (Japanese Welding Research Institute), 15, 233–244.

Metev, S. & Meteva, K. (1989). Nucleation and growth of laser-plasma deposited thin films. Applied Surface Science, 43, 402–408.

Miles, J. J. & Parker, M. R. (1996). Micromagnetic modelling of spin valve and GMR read heads. IEEE Transactions on Magnetics, 32, 4597–4602.

Miyagi, D., Miki, K., Nakano, M., & Takahashi, N. (2010). Influence of compressive stress on magnetic properties of laminated electrical steel sheets. IEEE Transactions on Magnetics, 46, 318–321.

Moses, A. J. & Davies, D. (1980). Influence of compressive stress on magnetic properties of commercial (110)[001] oriented silicon-iron. IEEE Transactions on Magnetics, 16, 454–460.

Mozharivskyj, Y., Pecharsky, A. O., Pecharsky, V. K., & Miller, G. J. (2005). On the high-temperature phase transition of $Gd_5Si_2Ge_2$. Journal of the American Chemical Society, 127, 317–324.

Muthuselvam, I. P. & Bhowmik, R. N. (2009). Structural phase stability and magnetism in Co_2FeO_4 spinel oxide. Solid State Sciences, 11, 719–725.

Neifeld, R. A., Gunapala, S., Liang, C., Shaheen, S. A., Croft, M., Price, J., Simons, D., & Hill, W. T. (1988). Systematics of thin films formed by excimer laser ablation: Results on $SmBa_2Cu_3O_7$. Applied Physics Letters, 53, 703–704.

Nishikawa, Y., Tanaka, K., & Yoshida, Y. (1991). Morphology of particles generated from thin film by excimer laser ablation. Nippon Kinzoku Gakkaishi, 55, 581–587.

Nlebedim, I. C., Ranvah, N., Williams, P. I., Melikhov, Y., Anayi, F., Snyder, J. E., Moses, A. J., & Jiles, D. C. (2009). Influence of vacuum sintering on microstructure and magnetic properties of magnetostrictive cobalt ferrite. Journal of Magnetism and Magnetic Materials, 321, 2528–2532.

Nlebedim, I. C., Snyder, J. E., Moses, A. J., & Jiles, D. C. (2010). Dependence of the magnetic and magnetoelastic properties of cobalt ferrite on processing parameters. accepted for publication in Journal of Magnetism and Magnetic Materials.

O'Handley, R. C. (2000). Modern magnetic materials: Principles and applications. (New York: John Wiley and Sons).

Okamoto, H. (1995). Comment on Gd-Si (gadolinium-silicon). Journal of Phase Equilibria, 16, 198–199.

Pecharsky, A. O., Gschneidner Jr., K. A., & Pecharsky, V. K. (2003). The giant

magnetocaloric effect of optimally prepared $Gd_5Si_2Ge_2$. Journal of Applied Physics, 93, 4722–4728.

Pecharsky, A. O., Gschneidner Jr., K. A., Pecharsky, V. K., & Schindler, C. E. (2002). The room temperature metastable/stable phase relationships in the pseudo-binary Gd_5Si_4-Gd_5Ge_4 system. Journal of Alloys and Compounds, 338, 126–135.

Pecharsky, V. K. & Gschneidner Jr., K. A. (1997a). Giant magnetocaloric effect in $Gd_5(Si_2Ge_2)$. Physical Review Letters, 78, 4494–4497.

Pecharsky, V. K. & Gschneidner Jr., K. A. (1997b). Phase relationships and crystallography in the pseudobinary system Gd_5Si_4-Gd_5Ge_4. Journal of Alloys and Compounds, 260, 98–106.

Pecharsky, V. K. & Gschneidner Jr., K. A. (1997c). Tunable magnetic regenerator alloys with a giant magnetocaloric effect for magnetic refrigeration from ~20 to ~290 k. Applied Physics Letters, 70, 3299–3301.

Pereira, A. M., Peixoto, J. R., Leitao, D., Sousa, C., Carpinteiro, F., Tavares, P. B., Martins, N., Sousa, J. B., & Araujo, J. P. (2008). Preparation of $Gd_5Si_2Ge_2$ compounds using RF-induction. Journal of Non-Crystalline Solids, 354, 5292–5294.

Perttunen, C. D., Jones, D. R., & Stuckman, B. E. (1993). Lipschitzian optimization without the lipschitz constant. Journal of Optimization Theory and Application, 79, 157–181.

Predel, B. (1991). Landolt-Bornstein, Group IV Physical Chemistry - Phase

Equilibria, Crystallographic and Thermodynamic Data of Binary Alloys, vol. 5. (Springer - Verlag).

Preisach, F. (1935). Uber die magnetische nachwirkung. Zeitschrift fur Physik, 94, 277–302.

Raghunathan, A., Snyder, J. E., & Jiles, D. C. (2009). Comparison of alternative techniques for characterizing magnetostriction and inverse magnetostriction in magnetic thin films. IEEE Transactions on Magnetics, 45, 3269–3273.

Ramesh, A., Jiles, D. C., & Bi, Y. (1997). Generalization of hysteresis modeling to anisotropic materials. Journal of Applied Physics, 81, 5585–5587.

Ramesh, A., Jiles, D. C., & Roderick, J. M. (1996). A model of anisotropic anhysteretic magnetization. IEEE Transactions on Magnetics, 32, 4234–4236.

Ranvah, N., Melikhov, Y., Jiles, D. C., Snyder, J. E., Moses, A. J., Williams, P. I., & Song, S. H. (2008). Temperature dependence of magnetic anisotropy of Ga-substituted cobalt ferrite. Journal of Applied Physics, 103.

Ranvah, N., Melikhov, Y., Nlebedim, I. C., Jiles, D. C., Snyder, J. E., Moses, A. J., & Williams, P. I. (2009a). Temperature dependence of magnetic anisotropy of germanium/cobalt cosubstituted cobalt ferrite. Journal of Applied Physics, 105.

Ranvah, N., Nlebedim, I. C., Melikhov, Y., Snyder, J. E., Williams, P. I., Moses, A. J., & Jiles, D. C. (2009b). Temperature dependence of magnetic properties of $CoAl_xFe_{2-x}O_4$. IEEE Transactions on Magnetics, 45, 4261–4264.

Rodriguez-Carvajal, J. (1993). Recent advances in magnetic structure determination by neutron powder diffraction. Physica B: Physics of Condensed Matter, 192, 55–69.

Sablik, M. J. & Jiles, D. C. (1993). Coupled magnetoelastic theory of magnetic and magnetostrictive hysteresis. IEEE Transactions on Magnetics, 29, 2113–2123.

Sambandam, S. N., Bethala, B., Sood, D. K., & Bhansali, S. (2005). Evaluation of silicon nitride as a diffusion barrier for Gd-Si-Ge films on silicon. Surface and Coatings Technology, 200, 1335–1340.

Sawatzky, G. A., Van Der Woude, F., & Morrish, A. H. (1968). Cation distributions in octahedral and tetrahedral sites of the ferrimagnetic spinel $CoFe_2O_4$. Journal of Applied Physics, 39, 1204–1205.

Scheibe, H. J., Gorbunov, A. A., Baranova, G. K., Klassen, N. V., Konov, V. I., Kulakov, M. P., Pompe, W., Prokhorov, A. M., & Weiss, H. J. (1990). Thin film deposition by excimer laser evaporation. Thin Solid Films, 189, 283–291.

Shi, Y. M., Jiles, D. C., & Ramesh, A. (1998). Generalization of hysteresis modeling to anisotropic and textured materials. Journal of Magnetism and Magnetic Materials, 187, 75–78.

Slonczewski, J. (2009). Theory of magnetic hysteresis in films and its application to computers. IEEE Transactions on Magnetics, 45, 8–14.

Slonczewski, J. C. (1958). Origin of magnetic anisotropy in cobalt-substituted magnetite. Physical Review, 110, 1341–1348.

Slonczewski, J. C. (1991a). Dynamics of domains and walls in soft magnetic films. IEEE Transactions on Magnetics, 27, 3532–3538.

Slonczewski, J. C. (1991b). Theory of domain dynamics in film heads. IEEE Transactions on Magnetics, 27, 4784–4786.

Smit, J. & Wijn, H. P. J. (1959). Ferrites. (Eindhoven: N. V. Philips).

Snoek, J. L. (1936). Magnetic and electrical properties of the binary systems MO. Fe_2O_3. Physica, 3, 463–483.

Snoek, J. L. (1948). Dispersion and absorption in magnetic ferrites at frequencies above one Mc/s. Physica, 14, 207–217.

Song, S.-H. (2007). Magnetic and magnetoelastic properties of M-substituted cobalt ferrites (M=Mn, Cr, Ga, Ge). Ph.D. thesis, Material Science and Engineering, Iowa State University.

Stoner, E. C. & Wohlfarth, E. P. (1948). A mechanism of magnetic hysteresis in heterogenous alloys. Philosphical transactions of the Royal Society of London A, pp. 599–642.

Suzuki, Y. (2001). Epitaxial spinel ferrite thin films. Annual Review of Materials Science, 31, 265–289.

Suzuki, Y., Hu, G., Van Dover, R. B., & Cava, R. J. (1999). Magnetic anisotropy of epitaxial cobalt ferrite thin films. Journal of Magnetism and Magnetic Materials, 191, 1–8.

Tam, A. C. & Schroeder, H. (1989). New high-precision optical technique to measure magnetostriction of a thin magnetic film deposited on a substrate. IEEE Transactions on Magnetics, 25, 2629–2638.

Torrejon, J., Badini-Confalonieri, G., & Vazquez, M. (2008). Fabrication and magnetic properties of hard/soft magnetostatically coupled FePt-FeNi multilayer microwires. Journal of Applied Physics, 103, 07E712.

Tsuya, N. (1958). Theory of magnetostriction and g factor in ferrites. Journal of Applied Physics, 29, 449–451.

Veeco (2004). Digital Instruments Dimension 3100 User's Manual. Veeco Instruments Inc.

Warburg, E. (1881). Magnetische untersuchungen. Annalen der Physik, 249, 141–164.

Weil, L. (1952). Magnetostriction de quelques ferrites orientes thermiquement. CR Acadie des sciences, 234, 1351.

Wilson, P. R., Ross, J. N., & Brown, A. D. (2002). Simulation of magnetic component models in electric circuits including dynamic thermal effects. IEEE Transactions on Power Electronics, 17, 55–65.

Wolf, W. P. (1957). Effect of crystalline electric fields on ferromagnetic anisotropy. Physical Review, 108, 1152–1157.

Yosida, K. & Tachiki, M. (1957). On the origin of the magnetic anisotropy energy of ferrites. Progress of Theoretical Physics, 17, 331–359.

Zheng, H., Wang, J., Lofland, S. E., Ma, Z., Mohaddes-Ardabili, L., Zhao, T., Salamanca-Riba, L., Shinde, S. R., Ogale, S. B., Bai, F., Viehland, D., Jia, Y., Schlom, D. G., Wuttig, M., Roytburd, A., & Ramesh, R. (2004). Multiferroic $BaTiO_3$-$CoFe_2O_4$ nanostructures. Science, 303, 661–663.

Zhou, J.-P., He, H.-C., & Nan, C.-W. (2007). Effects of substrate temperature and oxygen pressure on the magnetic properties and structures of $CoFe_2O_4$ thin films prepared by pulsed-laser deposition. Applied Surface Science, 253, 7456–7460.

Zhu, J. . & Bertram, H. N. (1988). Micromagnetic studies of thin metallic films. Journal of Applied Physics, 63, 3248–3253.

Zhuang, Z., Rao, M., White, R. M., Laughlin, D. E., & Kryder, M. H. (2000). Barium ferrite thin film media with perpendicular c-axis orientation and small grain size. Journal of Applied Physics, 87, 6370–6372.

Zimm, C. B., Barclay, J. A., Harkness, H. H., Green, G. F., & Patton, W. G. (1989). Magnetocaloric effect in thulium. Cryogenics, 29, 937–938.

Zimm, C. B., Ratzmann, P. M., Barclay, J. A., Green, G. F., & Chafe, J. N. (1990). Magnetocaloric effect in neodymium. Advances in Cryogenic Engineering, 36, 763–768.

Zou, P., Yu, W., & Bain, J. A. (2002). Influence of stress and texture on soft magnetic properties of thin films. IEEE Transactions on Magnetics, 38, 3501–3520.